

Development of an Ab-initio based Chemical Reaction Model for Direct Simulation Monte Carlo method

Submitted in partial fulfillment of the requirements for

the degree of

Doctor of Philosophy

by

Tapan K Mankodi

123100005

Supervisor:

Prof. U. V. Bhandarkar



Department of Mechanical Engineering

Indian Institute of Technology Bombay

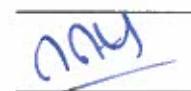
2018

*To
Mummy
&
Pappa*

Approval Sheet

This thesis titled Development of an Ab-initio based Chemical Reaction Model for Direct Simulation Monte Carlo method by Tapan K Mankodi is approved for the degree of Doctor of Philosophy.

Examiners



Supervisor



Chairperson



Date: 18/06/2018

Place: Mumbai

Declaration

I declare that this written submission represents my ideas in my own words and where others ideas or words have been included, I have adequately cited and referenced the original sources. I also declare that I have adhered to all principles of academic honesty and integrity and have not misrepresented or fabricated or falsified any idea/data/fact/source in my submission. I understand that any violation of the above will cause for disciplinary action by the Institute and can also evoke penal action from the sources which have thus not been properly cited or from whom proper permission has not been taken when needed.



Tapan K Mankodi

Roll No 123100005

Date: 18/6/2018

Abstract

Direct Simulation Monte Carlo (DSMC) is a particle method that is widely used to study high Knudsen number flows such as micro-channel flows and hypersonic flow around re-entry vehicles at rarefied ambient atmosphere. The present work focuses on investigating the flow physics around the re-entry vehicle. Simulating such flows is challenging as the high enthalpy in the post shock region leads to various interesting phenomena such as inelastic energy exchange, chemical and ionization reactions, thermal and chemical surface ablation and radiative heat transfer. Further, the flow contains high degree of non-equilibrium. An efficient parallelized 3D DSMC Code is developed and various collision models have been implemented and tested. These include the Larsen-Borgnakke (LB) model for inelastic energy exchange, Total Collision Energy (TCE) model and Quantum Kinetic (QK) model for chemical and ionization reactions.

The existing chemical reaction models in available literature (TCE and QK) employed in the DSMC method are phenomenological in nature and their use in the study of non-equilibrium flows is questionable. As a part of this work, a new chemical reaction model is formulated that has a stronger theoretical framework. Based on this framework, the reactive cross-sections employed for modelling chemical reactions are calculated using large ensembles of atomistic simulations. These simulations are carried out using the Quasi-classical Trajectory (QCT) method. The QCT method requires highly accurate Potential Energy Surfaces (PESs) that need to be based on ab-initio methods. New PESs for O_3 , O_4 , N_3 and N_4 systems based on highly accurate Multi-Configurational Self-Consistent Field (MCSCF) methods such as Complete Active Space SCF (CASSCF) method and Complete Active Space Perturbation Theory (CASPT2) method are constructed using MolCAS computational chemistry software. The reaction cross-section database for all important reactions pertaining to air chemistry are generated and published in the literature. It is found that the DSMC simulations with the new ab-initio based chemical reaction model predicts higher heat flux and heat load on the re-entry vehicle surface compared to the simulations employing the TCE and QK phenomenological model. This is a significant inference for engineers designing the Thermal Protection Systems (TPS). The limitations of the present model and future scope have also been discussed in detail.

Contents

List of Figures	xiii
List of Tables	xix
List of Symbols	xx
1 Introduction	1
1.1 Re-entry Vehicles	1
1.2 Motivation and Scope of the Present Work	3
1.3 Outline of the Thesis	7
2 Literature Survey	9
2.1 Collision Models in DSMC	10
2.2 Chemical reaction modelling in DSMC	13
2.3 An alternative Ab-initio Chemical reaction model	15
2.4 Potential Energy Surfaces in Air Chemistry	19
2.4.1 O ₃ system	19
2.4.2 N ₃ system	20
2.4.3 NO ₂ system	21
2.4.4 N ₂ O system	22
2.4.5 O ₄ system	23
2.4.6 N ₄ PES	24
2.4.7 N ₂ O ₂ system	24
2.5 Summary	25
3 Computational Methodology	27
3.1 MolCAS Ab-initio Package	27
3.2 QCT Method Code	29
3.2.1 Initializing a trajectory	29
3.2.2 Time Integrator	32
3.2.3 Outcome of a trajectory	33
3.2.4 Cross-section	34

3.3	DSMC Code	35
3.3.1	Determining computational parameters	35
3.3.2	Describing a DSMC particle	36
3.3.3	Movement module	38
3.3.4	Collision Module	38
3.3.5	Chemical Reaction Modelling	41
3.3.6	Domain and Boundary Conditions	42
3.3.7	Sampling Procedure	43
3.4	Summary	43
4	Development of New Potential Energy Surface	45
4.1	O ₃ PES	45
4.2	N ₃ PES	49
4.3	O ₄ PES	51
4.4	N ₄ PES	62
4.5	Summary	63
5	Cross-section Database	65
5.1	Cross-section fitting scheme	66
5.1.1	Selection of ro-vibrational level	66
5.1.2	Fitting scheme formulation	67
5.1.3	Validation of the scheme	69
5.2	Results and Discussion	71
5.3	Reaction Rate Coefficients	78
5.4	Summary	82
6	DSMC Simulations of Re-entry flows	83
6.1	Simulation at Equilibrium Conditions	84
6.2	Nitrogen Reactions under Non-equilibrium	85
6.3	Oxygen Reactions under Non-equilibrium	92
6.4	Stardust Re-entry Simulations	97
6.4.1	Stardust Geometry	97
6.4.2	Ambient and Computational Variables	98
6.4.3	Results and Analysis	99
6.5	Summary	111
7	Summary and Future Work	113
7.1	Summary and Key Contributions	113
7.2	Future Work	114

<i>CONTENTS</i>	xi
Bibliography	117
List of Publications	129
Acknowledgement	131

List of Figures

1.1	Flowchart of DSMC method.	3
1.2	Flowchart of alternative chemical reaction model.	6
2.1	Flowchart of Ab-initio chemical model for the DSMC method.	16
3.1	Atomic structure of an Nitrogen atom.	27
3.2	Molecular structure of a N_3 system.	28
3.3	Effective Potential Energy Curve at different rotational levels for Nitrogen molecule.	31
3.4	Graphical representation of a few of the possible outcomes for a QCT trial for the $N_2 + N_2$ reaction: a) no reaction, b) exchange reaction, c) single dissociation and d) double dissociation	34
3.5	Flowchart for chemical reaction modelling in DSMC.	42
3.6	Domain and Boundary Conditions.	43
4.1	Schematic diagram of the coordinate system	46
4.2	Detailed O_3 topography by constraining one of the three parameters (R1, R2, θ). Sub figure a) and b) show the structure at a fixed included angle of 60° and 116.8° respectively. Sub figure c) and d) show the 2D topography at fixed $R1 = 1.164196 \text{ \AA}$ and 1.4499532 \AA respectively. Reference energy for the PES $E(O_2+O)=119.2 \text{ kcal/mol}$	47
4.3	Optimized energy profile in C_{2v} symmetry for O_3 system. Different points corresponding to D_{3h} , C_{2v} , TS, local minima and maxima (M1 and M2) are demonstrated on the energy profile. Reference energy for the PES $E(O_2+O)=119.2 \text{ kcal/mol}$	48
4.4	Variation of energy (w.r.t. to dissociation threshold) along the minimum energy path (ρ) for ozone dissociation $O_3 \rightarrow O_2 + O$.Reference energy for the PES $E(O_2+O)=0 \text{ kcal/mol}$	48
4.5	2D Contour plot of N_3 PES with fixed included angle at 119° and varying R1-R2 depicting the transition state and the well structure. Reference energy for the PES $E(N_2+N)=228.7 \text{ kcal/mol}$	50

4.6	Optimized energy profile in C_{2v} symmetry for N_3 system. Different points corresponding to D_{3h} , C_{2V} , TS, local minima and maxima (M1 and M2) are demonstrated on the energy profile. Reference energy for the PES $E(N_2+N)=228.7$ kcal/mol.	51
4.7	Representation of a 4 atom system using the a) $(R1, R2, d, \theta, \phi, \psi)$ and b) $R1, R2, R3, \theta_1, \theta_2$ and ψ coordinate systems.	52
4.8	Probability density function for beta distribution for different shape parameters α and β	54
4.9	Normalized Probability density function for beta distribution and normalized gradient of the Potential Energy Curve of O_2 diatomic molecule.	55
4.10	Comparison of the O_4 PES using the present point generation scheme with Paukku et al.[79] for a) H shaped O_4 atomic configuration for a fixed $R1 = 1.098 \text{ \AA}$, $\theta = 90^\circ$, $\phi = 0^\circ$, $\psi = 90^\circ$ at different $R2$ and d , b) X shaped O_4 atomic configuration for a fixed $R1 = 1.098 \text{ \AA}$, $\theta = 90^\circ$, $\phi = 0^\circ$, $\psi = 0^\circ$ at different $R2$ and d	57
4.11	Contour plots for different geometric configurations. Sub figures a), b) and c) depict planar geometry and d) shows a non-planar geometry.	59
4.12	Variation of energy (kcal/mol) with R_c for cyclic geometry where R_c denotes the side of the square.	60
4.13	Minimum energy path for reaction $O_4 \rightarrow 2O_2$. All distances and angles have dimensions of \AA and $\text{deg}(\circ)$ respectively. Energy is with respect to O_2+O_2	61
4.14	2D contour plot in the neighbourhood of the D_{2d} stationary point as a function of a) R_{12} and θ_{123} with $\theta_{1234}=25.2^\circ$ and b) R_{12} and θ_{1234} with $\theta_{123}=87.3^\circ$. Energy is with respect to O_2+O_2	61
4.15	Comparison of the N_4 PES using random point generation scheme with Paukku et al.[83] for a) H shaped N_4 atomic configuration for a fixed $R1 = 1.098 \text{ \AA}$, $\theta = 90^\circ$, $\phi = 0^\circ$, $\psi = 90^\circ$ at different $R2$ and d b) a) X shaped N_4 atomic configuration for a fixed $R1 = 1.098 \text{ \AA}$, $\theta = 90^\circ$, $\phi = 0^\circ$, $\psi = 0^\circ$ at different $R2$ and d	62
5.1	Comparison of QCT results at $j=30$ with interpolated values using the data at $j=0$ and $j=\max(j)/2$ for $N_2+N \rightarrow 3N$ reaction. The vibrational number for all the line plots correspond to 20.	70
5.2	Comparison of QCT results (represented by scatter plot) with fitted values (line plot) using the data at $j=0$ and $j=\max(j)/2$ for the $N_2+N \rightarrow 3N$ reaction at $E_{trans} = 9.4$ eV and for different rotational and vibrational numbers.	70

5.3	Dissociation cross-section vs. Relative translational energy at different ro-vibrational levels for a)-b) $N_2 + N \rightarrow 3N$ and c)-f) $N_2 + N_2 \rightarrow N_2 + 2N$	73
5.4	Dissociation cross-section vs. Relative translational energy at different ro-vibrational levels for a)-b) $O_2 + O \rightarrow 3O$ and c)-f) $O_2 + O_2 \rightarrow O_2 + 2O$	74
5.5	Exchange cross-section vs. Relative translational energy at different ro-vibrational levels for a)-d) $O_2 + N \rightarrow NO + O$ on two surfaces. Dissociation cross-section for reactions e)-f) $O_2 + N \rightarrow 2O + N$ on the two surfaces.	75
5.6	Exchange cross-section vs. Relative translational energy at different ro-vibrational levels for a)-d) $N_2 + O \rightarrow NO + N$ on two surfaces. Dissociation cross-section for reactions e)-f) $N_2 + O \rightarrow 2N + O$ on the two surfaces.	76
5.7	Comparison of CID cross-section for the reaction $N_2 + N \rightarrow 3N$ calculated using QCT trials and fitting function for different vibrational levels at $j=0$	77
5.8	Dissociation rate coefficients calculated using data from the calculated cross-section database for the dissociation a) $O_2 + O \rightarrow 3O$ and b) $N_2 + N \rightarrow 3N$ compared with theoretical studies, shock tube experimental results and other computational works.	78
5.9	Dissociation rate coefficients calculated using data from the calculated cross-section database for the dissociation a) $O_2 + O_2 \rightarrow O_2 + 2O$ and b) $N_2 + N_2 \rightarrow N_2 + 2N$ compared with theoretical studies, shock tube experimental results and other computational works.	79
5.10	Exchange reaction rate coefficients calculated using data from the present work for the exchange a) $N + O_2 \rightarrow NO + O$ and b) $NO + O \rightarrow N + O_2$ compared with experimental results by Sayos et al.[114] and computational results [115, 116, 67]	79
5.11	Exchange reaction rate coefficients calculated using data from the present work for the exchange $O + N_2 \rightarrow NO + N$ compared with experimental results by Baulch et al.[117] and computational results [118, 119]	80
5.12	Dissociation rate coefficient calculated using the QCT data for a) N_2 dissociation, b) O_2 dissociation and c) NO dissociation compared with previous experimental[120, 107], computational[54, 34] and theoretical work[1].	81
6.1	Comparison of theoretical equilibrium degree of dissociation and DSMC simulations with ab-initio based chemical model.	85
6.2	Comparison of a) Translational temperature, b) N_2 number density, c) Pressure and d) U Velocity in simulation using the two different chemical models	86
6.3	Comparison of different modes of temperatures at the centreline for TCE and Ab-initio based chemical model.	87

6.4	Comparison of mole fraction of the two species at the centreline for TCE and Ab-initio based chemical model.	87
6.5	Cross-sections as calculated using the assumed form for TCE and those obtained from the QCT studies for two vibrational numbers ($v=20,30$) for $N_2 + N$ reaction.	88
6.6	Comparison of non-dimensional heat flux on the cylinder surface for TCE and Ab-initio based chemical model.	89
6.7	Comparison of a) number density of N_2 , b) number density of N , c) translational temperature and d) pressure for simulations employing TCE and Ab-initio based chemical models.	90
6.8	Comparison of number density of N_2 for simulations employing TCE and Ab-initio based chemical models between the contact discontinuity and shock wave.	91
6.9	Comparison of contour plots of Pressure, Total Temperature and U velocity, (x component of velocity) for DSMC simulations employing TCE and Ab-initio chemical models for low ($U_\infty = 5000$ m/s) (Sub figure a, c and e) and high ($U_\infty = 10000$ m/s) (Sub figure b, d and f) inlet velocity.	93
6.10	Comparison of CID cross-sections predicted by the TCE model and the ab-initio method for reaction $O_2 + O_2 \rightarrow O_2 + 2O$ at different vibrational numbers ($v_1 = v_2 = 0, 10$) and zeroth rotational number.	94
6.11	Comparison of population distribution (bar plot) of oxygen molecules in vibrational levels at the shock front acquired from DSMC simulations at $U_\infty = 5000$ m/s employing TCE and Ab-initio chemical models.	94
6.12	Comparison of centre-line plots of mole fraction of molecular and atomic Oxygen for DSMC simulations employing TCE and Ab-initio chemical models for a) low ($U_\infty = 5000$ m/s) and b) high ($U_\infty = 10000$ m/s) inlet velocity.	95
6.13	Comparison of centre-line plots of different modes of temperature (Translational, Rotational and Vibrational modes) for DSMC simulations employing TCE and Ab-initio chemical models for a) low ($U_\infty = 5000$ m/s) and b) high ($U_\infty = 10000$ m/s) inlet velocity.	95
6.14	Comparison of surface heat flux along the surface of the cylinder for DSMC simulations employing TCE and Ab-initio chemical models for a) low ($U_\infty = 5000$ m/s) and b) high ($U_\infty = 10000$ m/s) inlet velocity.	96
6.15	Stardust Re-entry capsule.	97
6.16	Comparison of streamline plots for DSMC simulations a) at 68 km, b) at 80 km and c) 100 km.	100
6.17	Comparison of contour plots of Pressure at a) 68 km, b) 80km and c) 100 km using DSMC simulations employing TCE and Ab-initio chemical model	102

6.18	Comparison of contour plots of U component of Velocity at a) 68 km, b) 80km and c) 100 km using DSMC simulations employing TCE and Ab-initio chemical model	103
6.19	Comparison of contour plots of V component of Velocity at a) 68 km, b) 80km and c) 100 km using DSMC simulations employing TCE and Ab-initio chemical model	104
6.20	Comparison of contour plots of Translational Temperature at a) 68 km, b) 80km and c) 100 km using DSMC simulations employing TCE and Ab-initio chemical model	106
6.21	Comparison of line plots of Densities for DSMC simulations employing TCE (Sub figures a), c) and e) for altitudes at 68 km, 80km and 100 km respectively) and Ab-initio chemical model (Sub figures b), d) and f) for altitudes at 68 km, 80km and 100 km respectively)	107
6.22	Comparison of Surface heat flux along the surface for DSMC simulations employing TCE (Sub figures a), c) and e) for altitudes at 68 km, 80km and 100 km respectively) and Ab-initio chemical model (Sub figures b), d) and f) for altitudes at 68 km, 80km and 100 km respectively)	109
6.23	Line plots of variation of fraction of collisions leading to reactions along the centreline for a) production of NO b) consumption of NO.	110

List of Tables

2.1	Arrhenius reaction rate parameters ($k = AT^{-\eta}exp-E_a/kT$) for the 5 species 11 reaction chemical model.	13
2.2	List of PESs and reactions for which cross-section database is calculated using the QCT method.	18
3.1	Active space chosen for CASSCF calculation for various systems in air chemistry	28
4.1	Comparison of parameters with existing PES for O ₃ system	46
4.2	Comparison of parameters with existing PES for N ₃ system	50
4.3	Mean unsigned error (MUE) and root mean square errors (RMSE) of the analytical fit with the CASPT2 PES for O ₄ system.	57
4.4	Mean unsigned error (MUE) and root mean square errors (RMSE) of the analytical fit with the analytical fit by Paukku et al.[83].	58
4.5	Heat of formation and barrier height (O ₄ → 2O ₂).	62
5.1	Spectroscopy constants(cm ⁻¹)	69
5.2	Comparison of reactive cross-section generated by the QCT method and using the weight based fitting scheme for random sets of ro-vibrational combination at 16000 m/s relative velocity for the reaction N ₂ +N ₂ → N ₂ +2N.	71
6.1	Ambient conditions at different altitudes	98
6.2	Computational run time per time-step(s)	99

List of Symbols

\mathcal{H}	Hamiltonian Operator
\mathcal{H}	Space variable
μ_{ref}	VHS Reference viscosity
ω	VHS parameter
σ_R	Reactive Cross-section
σ_T	Total Collision Cross-section
Θ_{diss}	Characteristic Temperature of Dissociation
Θ_{rot}	Characteristic Temperature of Rotational Excitation
Θ_{vib}	Characteristic Temperature of Vibrational Excitation
c_r	Relative velocity
$c_{r,ref}$	VHS Reference Relative velocity
$e_{v,j}$	Internal Energy
j	Rotational Level
Kn	Knudsen Number
T_{ref}	VHS Reference temperature
U_∞	Stream Velocity or Re-entry Speed
v	Vibrational Level
Z_{rot}	Rotational Relaxation number
Z_{vib}	Vibrational Relaxation number

Chapter 1

Introduction

1.1 Re-entry Vehicles

A re-entry vehicle, as the name suggests, is a critical component of an aerospace mission that enters the atmosphere of a planet or satellite before its touchdown. Space Shuttles and the Crew Return Vehicles (CRV) ferrying astronauts from the International Space Station to Earth are examples of re-entry vehicles. Primarily, the re-entry vehicles are designed keeping the Earth's atmosphere in context. However, with the passage of time, more ambitious missions for various astronomical objects will require re-entry vehicles to confront different atmospheres.

In the case of re-entry to Earth's atmosphere, vehicles face extreme conditions[1] during the hypersonic descent through various atmospheric layers. Additionally, the conditions rapidly change from molecular flow in the exosphere to rarefied low density conditions in the upper mesosphere to continuum conditions till the vehicle touches the ground. The hypersonic flow passes through the characteristic bow shock in the upstream of the blunt shaped re-entry vehicle. In the post-shock region, a sudden change in kinetic energy leads to high temperatures and density in the vicinity of the surface. A Thermal Protection Surface (TPS) is installed on the re-entry vehicle to ensure that the high energy in the flow does not incinerate the vehicle along with its passengers. It is clear that designing the TPS is paramount to the safety of the passengers as well as the mission.

Designing the TPS requires information of the heat flux and the heat load that a re-entry vehicle will face during its actual flight. A series of in-flight and on-ground experiments have been conducted to obtain important data as well as to test the TPS designs. For example, the Indian Space Research Organization's (ISRO) Crew Module Atmospheric Re-entry Experiment (CARE) mission was an in-flight experimental mission launched in December 2014. The objective of the mission was to validate the perfor-

mance of the parachute based deceleration system and to understand blunt body re-entry aerothermodynamics. It is obvious that the in-flight and on-ground experiments demand a high value of resources and are expensive. Computational simulations are an economical alternative and can provide useful information by appropriately modelling the flow around the re-entry vehicles.

Computational Fluid Dynamics algorithms have been extensively and effectively used to simulate re-entry flows since the earliest space missions. Various complex shock structures as well as shock-boundary layer and shock-turbulence interactions have been of interest in recent times. However, the CFD method can only be applicable for situations where the flow fulfills the continuum assumption, wherein the density is high enough so that the gradients used in the Navier-Stokes equations are well-defined. At altitudes higher than 65 km, the atmosphere is rarefied and the continuum assumption is not satisfied. As a result, simulating rarefied gas dynamics is complicated since the shock structures in such conditions introduce a high degree of non-equilibrium in the flow. This further reduces the utility of CFD simulations that assume equilibrium conditions as a pre-requisite for modelling the flow physics. An alternative Lagrangian method, the Direct Simulation Monte Carlo (DSMC) method [2, 3], is a much better suited method for studying hypersonic aerothermodynamics at rarefied and non-equilibrium conditions. The DSMC method is a particle method that was developed by Prof G. A. Bird in the early seventies[4, 5, 6]. However, the method is computer intensive and hence was not used substantially in the seventies and eighties. With the advent of improved computer architecture and high performance computing algorithms in the nineties[7, 8, 9], DSMC started being used widely and is presently the preferred choice for studying rarefied flows. In addition to the high energy flows described here, the DSMC method finds application in study of micro-channel flow physics[10] and will play an important role in development of micro-fluid machines. The present work studies the hypersonic flow around a re-entry vehicle at rarefied ambient conditions using this DSMC method.

In DSMC, each representative “particle” is equivalent to a large number of real molecules or atoms. The general flowchart of the DSMC method is shown in Figure 1.1. The domain is discretized into cells having dimensions less than the local mean free path and the time step chosen is a fraction of the mean collision time. Under these assumptions, the movement of the particles is fashioned in a rectilinear trajectory and the intra-cellular collisions are handled in a probabilistic manner. This process is repeated iteratively to gather a large sample of microscopic information of the particles. The macroscopic variables such as different modes of temperature, pressure, density, Mach number are calculated using kinetic theory relations. Inelastic energy exchange and chemical reactions are generally handled using various phenomenological models. In the case of re-entry to Earth’s atmo-

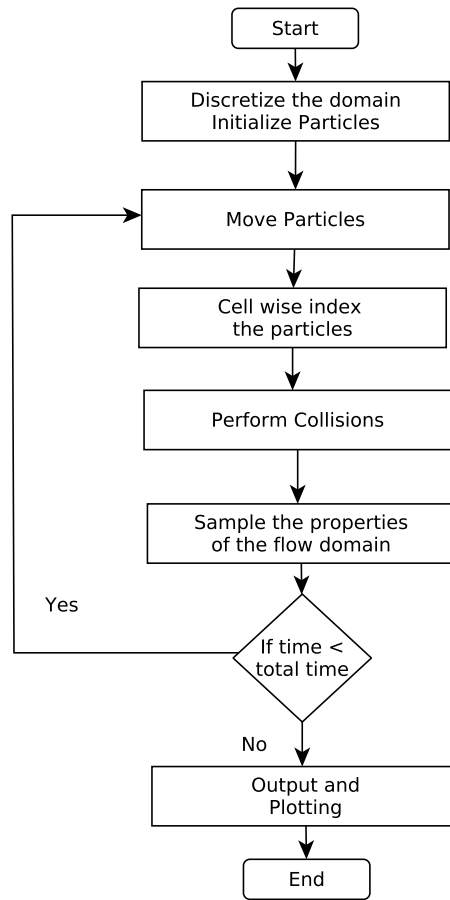


Figure 1.1: Flowchart of DSMC method.

sphere, the chemical reactions play a major role and have a direct consequence on heat flux and heat load calculations. Thus it is essential that any chemical reaction model employed in the DSMC code should be accurate and reliable.

1.2 Motivation and Scope of the Present Work

Oxygen molecules start to dissociate at temperatures higher than 2000 K and are completely dissociated at temperatures above 4000 K , whereas Nitrogen molecules dissociate at temperatures above 4000 K and are completely dissociated at temperatures above 9000 K . The energy in the post shock region is greater than the bond dissociation energy of these molecules. In addition to dissociation, recombination and exchange reactions, also known as the Zeldovich reactions, are an important part of the air chemistry. With further increase in the energy, the ionization reactions also come in to picture and add to the complexity of the problem.

From the collision theory point of view, chemical reactions are possible only when the

reactants collide and exchange enough energy to break existing bonds and form new ones. Generally, colliding molecules involving an energy interaction exceeding a certain energy barrier, known as the activation energy, are capable of reacting with each other. Further, only a fraction of such colliding molecules have an appropriate orientation during the collision that can result into a chemical reaction. This fraction is called the steric factor. The reaction rate given by the collision theory takes the following form

$$k = \left(\begin{array}{c} \text{Steric} \\ \text{Factor} \end{array} \right) \times \left(\begin{array}{c} \text{Fraction of molecules} \\ \text{having energy greater} \\ \text{than activation energy} \end{array} \right) \times \left(\begin{array}{c} \text{Collision} \\ \text{Frequency} \end{array} \right)$$

The concept of steric factor is closely related to the definition of reactive cross-section. The reactive cross-section represents the probability for occurrence of a reaction in contrast to the total collision cross-section which represents the probability for occurrence of a collision. The cross-sections are expressed in units of area. The ratio of reactive cross-section to the total collision cross-section is the steric factor.

Collision dynamics at molecular level can be simulated using the Molecular Dynamics method. The participating reactants are made to collide with each other to test if the reaction occurs or not. As the probability for a reaction to occur is a function of the orientation of the collision and since every orientation cannot be tested, a statistical approach becomes necessary. One of the methods that uses this concept is the Quasi-Classical Trajectory (QCT) method. In the QCT method, reactants are initialized at randomly chosen orientations and their trajectories are simulated; a large ensemble of such trajectories are analyzed to obtain sufficient statistical information on the reaction. The fraction of such simulations or trajectories resulting in a successful reaction to the total trajectories is the reaction probability which is similar to the steric factor. The reactive cross-section is calculated using the reaction probability data and it depends not only on the relative translation energy between the colliding particles, but also on the ro-vibrational levels of the particles. The ro-vibrational levels characterize the amount of internal energy stored in a particle. For an atom-diatom collision, the reactive cross-section is a function of the rotational and vibrational level of the molecule. In contrast, for a diatom-diatom collision, the reactive cross-section is a function of the combination of rotational and vibrational levels of both the molecules.

The key ingredient in the QCT method is the energy of interaction between the various atoms of the system. The method uses the gradient of this potential energy to calculate

the forces on each component that can be used to calculate the acceleration of the component, which in turn can be used to track the movement of the component using any integration scheme. The calculation of this potential energy is then a critical process since the success of the scheme depends on the accuracy of the potential energy. For accurate calculations, a global Potential Energy Surface (PES) is constructed for different combinations of interatomic distances between the interacting particles forming the reaction system by solving the Schrödinger equation. The gradient of the potential energy in the QCT method is calculated using an analytically fitted form of the constructed global potential energy surface. A large repository of methods is available for solving the Schrödinger equation numerically and these constitute the subject of Computational Chemistry. Several packages such as MolCAS, MolPRO, Gaussian, Gamess offer a wide range of state of the art computational chemistry algorithms. The use of such ab-initio methods to calculate the PES leads to highly accurate potential energy and force calculations. Using these PESs along with the QCT method should result in accurate reactive cross sections that depend only on the translational, rotational and vibrational energies of the colliding species, without the necessity of an equilibrium temperature.

In contrast to the description above, the chemical models presently employed in DSMC are inherently phenomenological in nature. In one of the mostly widely employed chemical reaction model, the Total Collision Energy (TCE) model, the different modes of energies (translational, rotational and vibrational) of the reactants are added to obtain the total collision energy. An analytical relation of the reactive cross-section as a function of the total collision energy is assumed. The fitting parameters for the analytical relation are calculated using available equilibrium reaction rate data by back substitution. The limitation of the TCE model is that it takes no account of the varying influence of different modes of energy on the reactive cross-section. In addition to this, the dependence on the equilibrium based Arrhenius theory in calculating the appropriate parameters may not model a chemical reaction properly in non-equilibrium flows. Other chemical reaction models also have been used in DSMC, such as the Vibrationally Favourable Dissociation (VFD) model and Quantum Kinetic (QK) model. However, these too are phenomenological in some manner or other and hence suffer from the same shortcomings as the TCE model. Instead of using these phenomenological reaction models, the reactive cross-sections calculated using the QCT method can be directly utilized in DSMC, and this in turn should significantly improve our understanding of the reactions in rarefied flows especially those containing high degree of non-equilibrium. At equilibrium conditions, the reaction rate coefficients calculated using these reactive cross-section databases should match with the available experimental data. The overall difference between the phenomenological models and this alternative chemical reaction model is summarized in Figure 1.2. It is desirable that such a chemical reaction model is based on ab-initio theory and has a stronger the-

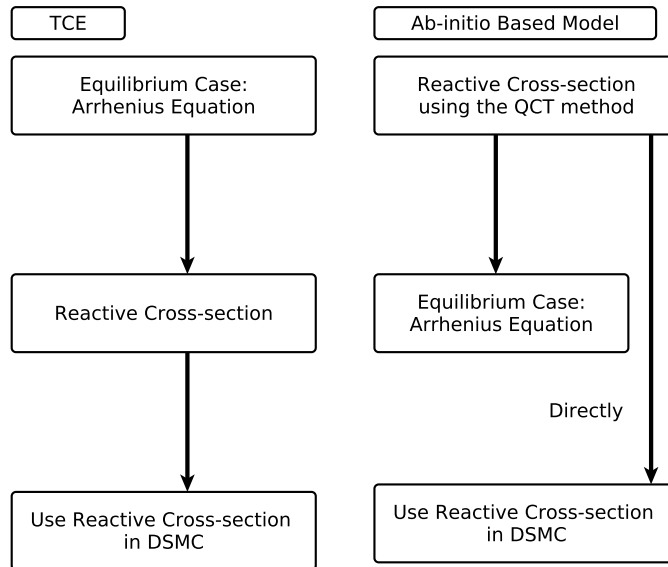


Figure 1.2: Flowchart of alternative chemical reaction model.

oretical framework. The aim of the present thesis is to develop, present and test this alternative chemical reaction model.

Based on the above discussion, the objectives of the present work can be stated as follows:

- To develop an efficient three-dimensional parallelized DSMC code for simulating non-equilibrium conditions in a re-entry flow that employs an ab-initio based chemical reaction model in order to investigate the flow properties in the domain as well as the surface properties on a vehicle re-entering at hypersonic speeds.
- To generate a reactive cross-section database of all major reactions of air chemistry for use in the model described in the objective above by employing the QCT method on highly accurate PESs. The objective will entail writing a QCT code and generating the cross-section database for all possible combinations of energy distributions in the reacting species.
- To construct PESs using highly accurate ab-initio methods for reaction systems that are currently unavailable as well as to collate all available accurate PESs so that they can be employed in the QCT method stated in the objective above.

1.3 Outline of the Thesis

A literature survey of the DSMC method and the presently used phenomenological models for simulating inelastic collisions and chemical reactions is presented in Chapter 2. The limitations of the existing chemical reaction models are also presented in detail in this chapter, apart from providing a better description of the alternative chemical reaction model that is being proposed. A literature survey on the presently available Potential Energy Surfaces required for developing the new ab-initio chemical reaction model is also discussed.

Chapter 3 presents details of all the codes used for the present work. This includes a presentation of the DSMC code and the QCT code that have been written as a part of this work. The chapter then presents the MolCAS computational chemistry software that was used to generate the PESs.

The methodology of the construction of various PESs and the investigation of critical features on the topography of the PESs are explained in Chapter 4.

The generation of the new cross-section database using the QCT method by employing the new PESs as well as the existing PESs is described in Chapter 5. The analysis and validation of the database thus generated is also presented. The validation is carried out by calculating the reaction rate coefficients at equilibrium conditions and comparing with the existing ones in the literature.

In Chapter 6, a comparative study of previously reported chemical reaction models and the new ab-initio chemical reaction model is undertaken for equilibrium and non-equilibrium flows. Hypersonic air flow around the re-entry vehicle at ambient rarefied conditions using the different chemical models is studied in detail. The effect of the ab-initio chemical reaction model on the flow properties in the post shock region and heat flux on the vehicle surface is investigated.

The important conclusions from the present work are detailed in Chapter 7. The present work has thrown up a lot of questions that need to be addressed. Possible future work arising from these questions is also discussed in this chapter.

Chapter 2

Literature Survey

Fluid flow is simulated broadly through two approaches: atomistic and continuum modelling. Atomistic modelling studies the physics at a molecular level using simulation techniques such as Molecular Dynamics and Quantum mechanical calculations. On the opposite side of the scale, the fluid which inherently consists of atoms and molecules is treated as continuous and the flow is modelled by the Navier-Stokes equations. Numerous examples in fluid dynamics exist where the continuum assumption is not strictly valid and concurrently the number of atoms or molecules is substantial rendering Molecular Dynamics computationally impracticable. If the simulation approaches are to be demonstrated on a scale, then such complex situations known as transition flows would lie in the middle. Such a scale is quantified using a dimensionless parameter known as the Knudsen number. Knudsen number is the ratio of mean free path (λ) to the characteristic length (L).

$$Kn = \frac{\lambda}{L} \quad (2.1)$$

The flow regimes are not clearly demarcated on the Knudsen number line. However, it has been observed that the continuum assumption breaks down around $Kn \sim 0.1$. At standard conditions ($p = 1$ atm, $T = 273.15$ K), the number density is equal to the Loschmidt number ($2.68678 \times 10^{25} \text{m}^{-3}$). The mean free path is equal to $4.8 \times 10^{-8} \text{m}$. For a box with length equal to 1 m, the Knudsen number is approximately of the order of 10^{-8} . The flow at these conditions belongs to continuum regime and can be studied using the continuum based CFD techniques. Flows having Knudsen number greater than 0.1 belong to transition flow regime and those flows with Kn greater than 10 are known as free molecular flows. The flow around a re-entry vehicle at altitudes above ~ 70 km is an example of transition flow. The low ambient density ($\sim 10^{20} \text{m}^{-3}$) leads to higher mean free path (> 0.01 m) and consequently high Knudsen number. In the case of flow through micro-channels, low characteristic lengths lead to rarefaction. In the present work, the

former situation is of interest and is studied using the Direct Simulation Monte Carlo (DSMC) method.

A DSMC framework capable of modelling complex physical phenomena such as shock formation, elastic and inelastic collisions, chemical reactions and gas-surface interactions is developed as a part of the present thesis work. Several phenomenological models such as No-Time Counter model, Variable Hard Sphere and Variable Soft Sphere models for simulating collisions, Larsen-Borgnakke model for inelastic energy exchange, Total Collision Energy chemical reaction model, Quantum Kinetic chemical reaction model, Specular, Diffuse and Cercignani-Lords-Lampis gas-surface interaction models have been implemented. An analysis of the existing chemical reaction modelling raises skepticism about using phenomenological models for simulation of critical applications. An alternative chemical model is developed with the view to improve the present DSMC models. A short literature review on the existing phenomenological models, followed by review of available resources in the development of the ab-initio based chemical reaction model is covered here.

2.1 Collision Models in DSMC

The collision step is the most important step in the DSMC algorithm. The intra-cellular collisions are simulated using a probabilistic approach. The collision model aims to ensure an accurate local collision frequency (ν). Several phenomenological models have been developed to model collisions. Bird [7] first proposed the Time Counter (TC) model. Two particles are randomly sampled from the list of particles in a cell. The probability of the collision is $((\sigma_T c_r)/(\sigma_T c_r)_{max})$ where σ_T is the total collision cross-section, c_r is the relative velocity between the pair of colliding particles and $(\sigma_T c_r)_{max}$ is the maximum value of the product of cross-section and relative velocity recorded over the progress of the simulation. An acceptance-rejection scheme is used to decide if the pair of particles chosen collide or not that compares the probability of the collision to a random number that is generated. For each selection of pair of particles, an increment in time (Δt_c) is computed using the formula:

$$\Delta t_c = \frac{2\Delta V}{\bar{N} N F_{NUM} \sigma_T c_r} \quad (2.2)$$

where ΔV is the volume of the cell, N is the number of particles in the cell at the given time step and \bar{N} is the average number of particles in the cell. The selection of the pair of particles for possible collision is carried on till the sum of the time increments (Δt_c) exceeds the simulation time step (Δt). This method does not reproduce the correct collision frequency under extreme non-equilibrium conditions.

Subsequently, Bird [7] proposed the No Time Counter (NTC) method which is an efficient $O(N)$ complexity algorithm. The total number of possible collision pairs are first computed using the formula:

$$N_T = \frac{1}{2} \frac{N(N-1)F_{NUM}(\sigma_{TCr})_{max}\Delta t}{\Delta V} \quad (2.3)$$

The probability of collision is the same as that in the TC model. Collisions performed using the NTC model showed exceptionally accurate match with the theoretical collision frequency results even in cases with high degree of non-equilibrium.

In addition to these, other widely used collision models include the Collision Frequency (CF) Scheme introduced by Koura[11], Majorant Collision Frequency (MCF) model by Ivanov[12, 13] and Null Collision (NC) scheme[14].

The total collision cross-section (σ_T) employed in the above method has dimensions of area and can be related to the probability of a collision event to occur. The formula to calculate the total collision cross-section is:

$$\sigma_T = \pi d^2 \quad (2.4)$$

where d is the particle diameter. The simplest model to calculate the diameter is the Hard Sphere model. The diameter is calculated using viscosity coefficients with the help of the following formula:

$$d^2 = \frac{(5/16)(mkT_{ref}/\pi)^{\frac{1}{2}}}{\mu_{ref}} \quad (2.5)$$

where k is the Boltzmann constant, m is the mass of the gas particle, μ_{ref} is the reference viscosity at the reference temperature, T_{ref} . It was found that this model does not reproduce the correct viscosity-temperature variation.

The Variable Hard Sphere (VHS) model proposes that the effective diameter is a function of the relative kinetic energy between the colliding particles. According to the VHS model, the effective diameter is

$$d_{VHS} = d_{ref} \frac{c_{r,ref}^\xi}{c_r} \quad (2.6)$$

where d_{ref} is the effective diameter at a reference relative speed ($c_{r,ref}$) and ξ is VHS parameter adjusted to obtain the correct viscosity-temperature relation.

In addition to these cross-section models, several others such as Variable Soft Sphere (VSS)[15], Generalized Hard Sphere (GHS) [16], Generalized Soft Sphere (GSS)[17] models have been proposed to calculate the total collision cross-section. In the present work, all DSMC simulations are carried out using the No Time Counter (NTC) model to calculate the collision rate and the Variable Hard Sphere (VHS) model to calculate the cross-section.

A large amount of the kinetic energy of the molecules in the pre-shock region of the re-entry vehicle problem is transformed into the thermal (translational, rotational and vibrational) energy in the post-shock region. Thus, the molecules that are normally at the ground vibrational energy move to higher levels. Similarly, rotational levels increase apart from the molecules reaching higher speeds. Inelastic energy exchange leads to the transformation of the translational energy into ro-vibrational energy and vice versa.

Larsen and Borgnakke (LB)[18] have proposed a phenomenological model to simulate such inelastic energy exchange. According to this model, the inelastic energy exchange is carried out for only a fraction of all collisions. The inverse of this fraction, known as the relaxation number (Z), is chosen in such a manner that the simulated relaxation time matches well with the theoretical and experimental data. The post collision inelastic energy is randomly sampled from a continuous Maxwellian distribution in the case of rotational energy. In contrast, the vibrational energy is quantized into discrete levels. A quantum LB model for vibrational energy is proposed that includes this feature. Haas et al.[19] proposed a serial implementation of the inelastic energy exchange model where the rotational and vibrational energy exchange for any colliding pair is modelled to occur serially, i.e., one after the other.

Constant rotational and vibrational relaxation numbers are generally employed for DSMC simulations at conditions close to standard conditions. However, at extreme conditions, the rotational and vibrational relaxation numbers show a prominent dependence on the temperature and pressure. Parker[20] employed the following equation to model the temperature dependence of the rotational relaxation number

$$Z_{rot} = \frac{Z_{rot}^{\infty}}{1 + \pi^{1/2}/2(T^{\infty}/T_{tr})^{1/2} + (\pi + \pi^2/4)(T^{\infty}/T_{tr})} \quad (2.7)$$

where the values of the parameters Z^{∞} and T^{∞} are chosen such that the temperature dependence matches with experimental findings. Lordi and Mates[21] advocated a different set of parameters for diatomic gas using the same equation.

Similar to rotational relaxation number, Bird[2] has formulated a relation that models

Table 2.1: Arrhenius reaction rate parameters ($k = AT^{-\eta}exp-E_a/kT$) for the 5 species 11 reaction chemical model.

Reaction	A	η	$E_a(\times 10^{-19} \text{ J})$
$O_2 + M \rightarrow 2O + M(=N,O)$	5.593×10^{-12}	1.0	8.197
$O_2 + M \rightarrow 2O + M(=N_2,O_2,NO)$	5.593×10^{-12}	1.0	8.197
$N_2 + M \rightarrow 2N + M(=O,O_2,NO)$	3.187×10^{-13}	0.5	15.61
$N_2 + M \rightarrow 2N + M(=N_2)$	7.968×10^{-13}	0.5	15.61
$N_2 + M \rightarrow 2N + M(=N)$	6.90×10^{-8}	1.5	15.61
$NO_2 + M \rightarrow N + O + M(=N,O)$	6.590×10^{-10}	1.5	10.43
$NO_2 + M \rightarrow N + O + M(=N_2,O_2,NO)$	1.318×10^{-8}	1.5	10.43
$NO + O \rightarrow N + O_2$	5.279×10^{-21}	-1	2.719
$N_2 + O \rightarrow NO + N$	1.120×10^{-16}	0	5.175
$O_2 + N \rightarrow NO + O$	1.598×10^{-18}	-0.5	0.4968
$NO + N \rightarrow O + N_2$	2.490×10^{-17}	0	0.0

the temperature dependence of the vibrational relaxation number :

$$Z_{vib} = C_1/T^\omega exp(C_2T^{-1/3}) \quad (2.8)$$

where C_1 and C_2 are parameters and ω is the VHS coefficient.

2.2 Chemical reaction modelling in DSMC

In addition to elastic and inelastic collisions, chemical reactions play a major role in determining accurate flow properties in the domain and surface properties on the re-entry vehicle TPS. The list of reactions pertaining to the five species air chemistry model along with the corresponding Arrhenius rate coefficient parameters as suggested by Park et al.[1] is tabulated in Table 2.1.

Similar to the inelastic energy exchange models, the common approach is to simulate chemical reactions using phenomenological models that calculate the reactive cross-section for a reaction. The reactive cross-section is the measure of probability for a reaction to occur. Bird [6] first proposed the Total Collision Energy (TCE) model. According to this model, the total collision energy, (the sum of relative translational, rotational and vibrational modes of energies) is employed to calculate the reactive cross-section which assumes the following form:

$$\sigma_R = 0 \quad E_c < E_a \quad (2.9)$$

$$\sigma_R = \sigma_T C_1 (E_c - E_a)^{C_2} (1 - E_a/E_c)^{\bar{\tau} + 3/2 - \omega} \quad E_c > E_a \quad (2.10)$$

where C_1 and C_2 are constants, τ is the average value of the number of degrees of freedom of internal energy, ω is the VHS viscosity parameter, E_c is the collision energy, E_a is the activation energy, σ_T is the collision cross-section and σ_R is the reactive cross-section. Only a fraction of collisions having energy greater than the activation energy can result in a reaction. The coefficient of reaction rate calculated by integrating the above assumed form of the reactive cross-section at equilibrium conditions should match the Arrhenius reaction rates found experimentally. The values of the constants C_1 and C_2 are computed from back substitution and have the following form:

$$C_1 = \frac{\pi^{1/2} A \Gamma(\bar{\tau} + 5/2 - \omega)}{2\sigma_{ref} \Gamma(\bar{\tau} + \eta + 3/2)} \left(\frac{m_r}{2kT_{ref}} \right)^{1/2} \frac{T_{ref}^{1-\omega}}{k^{\eta-1+\omega}} \quad (2.11)$$

$$C_2 = \eta - 1 + \omega \quad (2.12)$$

where σ_{ref} and T_{ref} are reference VHS parameters, while A and η are the pre-exponential factor and temperature coefficient respectively in the Arrhenius equation.

Boyd and Haas[22] proposed an extension to the TCE model, the Vibrationally-Favoured-Dissociation (VFD) model which accounts for the influence of the vibrational relaxation rate on the rate of dissociation. The reaction cross-section has an extra dependence on the vibrational energy of the particle. This is executed by employing an extra parameter ϕ . The σ_R takes the form:

$$\sigma_R = \sigma_{R,TCE} \left(\frac{E_v}{E_c} \right)^\phi \quad (2.13)$$

where E_v is the vibrational energy of the dissociating particle. A parametric study recommended that the value of ϕ should be 2.0 for N_2 and 0.5 for O_2 . A higher value of the parameter ϕ indicates higher coupling of the two processes.

Bird[9] reported the Quantum-Kinetic (QK) model that employs only the total energy involved in the collision. The quantum model for vibrational energy exchange using the Larsen-Borgnakke model is extended to include the dissociation reactions. The collision energy includes the relative translational energy and the vibrational energy of the particle. If the post collision vibrational energy level calculated using the LB model exceeds the dissociation limit, the particle is considered to proceed for dissociation. The condition for dissociation is given by:

$$i_{max} > \Theta_D / \Theta_V \quad (2.14)$$

where i_{max} is the maximum vibrational level, Θ_D is the characteristic temperature of dis-

sociation and Θ_v is the characteristic temperature of vibrational excitation.

2.3 An alternative Ab-initio Chemical reaction model

It is evident that the existing phenomenological models have serious limitations and an alternative chemical reaction model is needed that is free of macroscopic parameters and that gives justice to the varying influence of different modes of energies on the reactive cross-sections. The general algorithm of the Ab-initio based chemical model is shown in Figure 2.1. The first step involves the construction of a global Potential Energy Surface (PES) using computational chemistry methods. The surface constructed on discrete points is fitted with a suitable analytical expression. A cross-section database is then generated using a large number of trajectories. Cross-sections are integrated at equilibrium conditions to validate the reaction rate coefficients with available experimental data. An appropriate function is used to fit the cross-section and this is used in the DSMC ab-initio model.

The Quasi Classical Trajectory[23, 24] method tracks the time evolution of the participating reactants by solving the Hamilton's equations. The Hamiltonian (\mathcal{H}) of the system is defined as the sum of its kinetic energy and potential energy (\mathcal{V}):

$$\mathcal{H} = \sum_i \sum_{j=x,y,z} \frac{1}{2m_i} p_{i,j}^2 + \mathcal{V} \quad (2.15)$$

where the first letter of the subscripts $\{i, j\}$ denotes the atom and second denotes the coordinate ($j = x$ or y or z). The Hamilton's equations are given by:

$$\dot{p}_{i,j} = \frac{dp_{i,j}}{dt} = -\frac{\partial \mathcal{H}}{\partial q_{i,j}} = -\frac{\partial \mathcal{V}}{\partial q_{i,j}} \quad (2.16)$$

$$\dot{q}_{i,j} = \frac{dq_{i,j}}{dt} = \frac{\partial \mathcal{H}}{\partial p_{i,j}} = \frac{p_{i,j}}{m_i} \quad (2.17)$$

Here, \mathcal{V} is calculated using computational chemistry methods by solving Schrödinger equation. Detailed quantum mechanical calculation at each and every time-step by solving the Schrödinger equation using numerical methods is not practical. Energies are calculated for a few discrete points representing different geometries of the system leading to generation of a Potential Energy Surface (PES). The progress of the reaction can be visualized as a travel on this PES from regions characterizing reactants to those of products. A PES is generally constructed by solving the Hartree Fock (HF) transformation of the Schrödinger equation while invoking Born-Oppenheimer approximations. However,

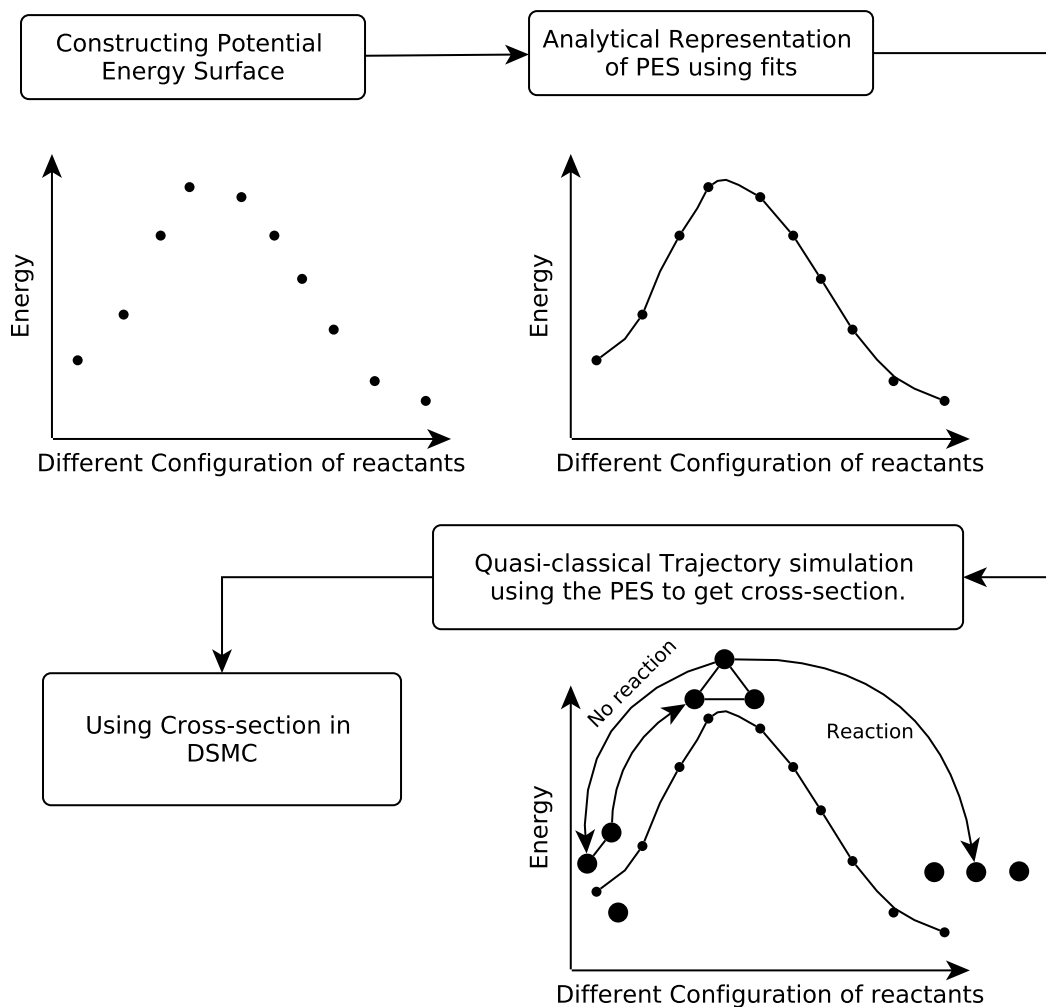


Figure 2.1: Flowchart of Ab-initio chemical model for the DSMC method.

as chemical reactions involve bond breaking and bond formation processes, higher end computational chemistry methods are necessary[25] for construction of a PES. It is suggested that post Hartree Fock methods such as Configuration Interaction (CI), Coupled Cluster (CC) algorithms, Moller-Plesset perturbation theory (MP_n) are not sufficient. Complex algorithms such as Multi-configurational self-consistent field (MCSCF) which includes Complete Active Space Self-Consistent Field method (CASSCF) and Complete Active Space Perturbation Theory (CASPT2) are presently recognized state of the art methods used for construction of PESs intended for studying reactions. Such accurate surfaces are unavailable for many systems required for studying reactions pertaining to air chemistry and these are presently calculated from scratch.

Presently, there are few published works that have used cross-section data calculated using ab-initio methods for use in DSMC simulations. Ozawa et al.[26, 27] obtained the cross-section for the reaction $O + HCl \rightarrow OH + Cl$ using the Ramachandran Peterson

(RP) PES[28]. Their DSMC model assumes that the rotational and vibrational energies are continuous variables, and calculates the reaction probability as a function of internal energy (E_{int}).

$$\sigma_r = \sigma_r(E_{int}, E_{trans}) \quad (2.18)$$

Wysong et al.[29] compared the reactive cross-section obtained from QCT, TCE and QK models for the dissociation $N_2 + N \rightarrow 3N$ and exchange reaction $N_2 + O \rightarrow NO + N$. They studied the effect of cross-sections obtained through QCT method and the phenomenological chemical models for DSMC simulation of hypersonic flow over a sphere, and found a mismatch between the reactive cross-section values as assumed in the TCE model and generated using the QCT method. Several papers [30, 31, 32, 33] have been published investigating ro-vibrational excitation and dissociation cross-section results corresponding to different thermal distributions of energy in various modes. The database in the above mentioned references are more suitable for CFD simulation rather than DSMC simulations. Besides these databases are not available for open access.

Ideally, a cross-section database suitable for DSMC should be generated as a function of rotational and vibrational levels of the colliding particles instead of macroscopic values of rotational and vibrational temperatures. This will ensure that there is no need to define a temperature and any non-equilibrium situation can be handled. A major obstacle in developing a suitable cross-section database is the extensive computational cost associated with the QCT sampling. The dissociation of nitrogen molecule upon collision with another nitrogen molecule is the most important reaction in Air Chemistry. A Nitrogen molecule has 9019 ro-vibrational levels. Thus, ensembles for QCT method have to be run for a total of ${}^{9019}C_2$ combinations of ro-vibrational levels for any specified value of relative translational energy. It is obvious that the computational cost associated with generating such a large database is not practical. A way around this would be to arrive at methods to decrease the computational cost using some interpolation scheme. Such a method has been discussed in the present work. The proposed new method calculates the reactive cross-section for the entire spectrum of ro-vibrational levels using a weighted fitting scheme using reactive cross-section data at only a few selected ro-vibrational levels. The weights are calculated using spectroscopic data.

As a part of this work, the reactive cross-section for all important reactions in the 5 species air chemistry model are generated and published. The reactions in air chemistry can be classified into the following groups:

- dissociation of N_2 or O_2 or NO colliding with another molecule,

- dissociation of N_2 or O_2 or NO colliding with an atom (N or O),
- recombination of two atoms to form a molecule,
- exchange (Zeldovich) reactions: $N_2 + O \rightleftharpoons NO + N$, $O_2 + N \rightleftharpoons NO + O$.

Although important and challenging, the recombination processes are skipped in the present analysis of the reaction modelling. This is because the probability of recombination is minimal in the high enthalpy vicinity of the re-entry vehicle at rarefied conditions. Further the formation of NO in the simulation is insufficient and the mole fraction of NO is less than 0.01. Hence, a cross-section database for the dissociation of NO with other molecules and atoms is not included. In DSMC simulations, these reactions will be modelled using the existing TCE model to ensure completeness.

Table 2.2: List of PESs and reactions for which cross-section database is calculated using the QCT method.

	N_2	O_2	NO
N_2	N_4 $N_2+N_2 \rightarrow N_2+2N$ $N_2+N_2 \rightarrow 4N$		
O_2	N_2O_2 $O_2+N_2 \rightarrow O_2+2N$ $O_2+N_2 \rightarrow N_2+2O$	O_4^* $O_2+O_2 \rightarrow O_2+2O$ $O_2+O_2 \rightarrow 4O$	
N	N_3^* $N_2+N \rightarrow 3N$	NO_2 $N+O_2 \rightarrow N+2O$ $N+O_2 \rightarrow NO+O$	N_2O $N+NO \rightarrow O+2N$ $N+NO \rightarrow N_2+O$
O	N_2O $O+N_2 \rightarrow O+2N$ $O+N_2 \rightarrow O+NO$	O_3^* $O+O_2 \rightarrow 3O$	NO_2 $O+NO \rightarrow N+2O$ $O+NO \rightarrow O_2+N$

* *New PES constructed*
Exchange reaction

Different reactions require different PESs. A summary of reactions studied and their corresponding PESs is tabulated in Table 2.2. The PESs marked with (*) are the newly constructed PESs using accurate computational chemistry methods. In the case of studying flow around the re-entry vehicles, the constituent atoms and molecules are often

transported to higher electronic states. Although the population of particles in higher electronic states is negligible, these particles may have a significant effect on the radiative component of the heat flux. Inclusion of the higher electronic states in the modelling of chemistry adds an appreciable computational effort and cost. Presently, the chemical reaction model involves the reactants and products in their respective ground states. In addition to this complexity, the ground state of the reactants and the products are often connected through multiple PESs. In the case of O_3 , O_4 , N_2O , and NO_2 systems, the multiple PESs have a low energy barrier and have multiple conical intersections. A reaction starting on a PES may end up on another surface during its progression. This is known as surface hopping. In the present study, the trajectories are run on different surfaces of a system to get accurate cross-sections. However, these trajectories are assumed to be adiabatic in nature and hence surface hopping is ignored. In contrast to the systems with oxygen atoms, the N_3 and N_4 PESs have large energy barriers and trajectories are simulated on ground state PES only.

2.4 Potential Energy Surfaces in Air Chemistry

2.4.1 O_3 system

Studies for the dissociation of O_2 molecule requires inclusion of non-adiabatic effects[34]. This is due to the closely spaced multiple electronic states for the O_3 system. In total, 27 electronic states need to be considered in absence of the spin-orbit interaction. Also the conical intersection between the two lowest PESs increases complications. The complexities of the O_3 system are discussed at length by Tashiro and Schinke[35], Andrienko and Boyd[34]. The inclusion of such complexities are presently beyond the scope of this work. At present, the trajectories are performed on a single ground state with adiabatic assumption. Previous studies[36] suggest multiplication with a degeneracy factor 16/3 to account for the multiple surface problem in calculating the dissociation rates coefficients.

An analytically derived PES by Varandas[37] in Double Many Body Expansion (DMBE) form has been used extensively[34, 38, 39, 40, 41] to study the O_3 system. This PES has a simple analytical form, formulated using experimental data on scattering and dissociation rate coefficients.

Several authors have presented a global PES or a part of it using ab-initio methods[42, 43, 44, 45]. Müller et al.[44] conducted a comparative study of characterization of open and ring minima using singles and doubles coupled-cluster (CCSD) method and a variety of basis sets. They concluded that the results calculated using CCSD(T) and MR-AQCC (Multi-reference interaction with Averaged Quadratic Coupled Cluster) with quadruple-

zeta correlation consistent basis set were within 3% of the experimental findings[46]. However, using methods such as single and double excitation perturbation method for studying systems with strong electron correlation such as bond breaking and bond formation cannot be justified with full confidence[25]. A superior procedure of generating a PES for few atom systems is by implementing a multi-configurational method to account for static electron correlation followed by a dynamic correlation step.

Recently developed PESs[47, 48, 49, 50, 51, 52] have incorporated the CASSCF method followed by multi-reference methods. The PES created is further used to study the kinetics of ozone formation $O_2 + O \rightarrow O_3$ and determining isotope exchange rates. Deviation from the isotope exchange rates with experimental findings, especially at low temperatures, and limited understanding of the anomalous mass independent fractionation effect has been widely perceived as a direct consequence of unavailability of a satisfactory global PES. Seibert et.al[47] reported a global PES (Siebert Schinke Bittererova or SSB PES) using multireference configuration interaction (MRCI) calculation and cc-PVQZ (correlation consistent polar valence only Quadruple-zeta) basis set. The SSB PES accurately described the open minima(C_{2v}), ring minima (D_{3h}) and dissociation threshold. Ozone dissociates to $O_2 + O$ when an end atom in the C_{2v} structure is removed. The SSB PES has a small barrier (45 cm^{-1}) above the dissociation limit and a van der Waals minimum in the exit channel of the minimum energy path. Babikov et.al.[48] have concluded that this barrier is an artifact.

Dawes et.al.[51, 52] have reported a PES constructed with MRCI-F12 method and VQZ-F12 basis set. A spin-orbit correction was added and it was observed that their PES showed accurate parameters of equilibrium structures (C_{2v} , D_{3h}) and transition region without the reef structure. In addition to this, the vibrational levels calculated using their PES showed satisfactory match with experiments. Moreover, substantial work[43, 53] has been carried out focusing on higher electronic states of Ozone.

2.4.2 N_3 system

Several studies have reported classical trajectory analysis of N_2-N collisions [54, 55, 56, 57] using N_3 PES. Laganà et al.[58] proposed the London-Eyring-Polanyi-Sato (LEPS) PES with a linear transition structure and a barrier height of 36 kcal/mol. Computational results[59] have suggested that the transition structure has a double barrier contrary to the LEPS structure.

Wang et al.[60] reported a global PES using open-shell Coupled-Cluster Singles and Doubles with perturbation-correction of Triples (CCSD (T)) technique and augmented

correlation consistent basis set (aug-cc-pVQZ) using 3326 points. They reported a double barrier at a height of 47.2 kcal/mol above the reactant energy separated by a shallow well at a depth of 3.5 kcal/mol relative to the barrier. The transition state as calculated due to Wang et al. was a non linear bent shaped structure. At the double barrier, the bond lengths between the adjacent N atoms were 1.18 Å and 1.48 Å with an included angle of 119°. At the shallow well, having the C_{2v} symmetry, the bond lengths were both 1.27 Å with 120° included angle. The PES was used to study the $N_2 + N$ exchange reaction using quantum dynamics wave packet calculations. The reported PES showed significant differences with the Laganà LEPS.

A series of PESs (L0-L4) were reported by Garcia et.al.[57] based on CCSD(T)/aug-cc-pVTZ system. PESs were based on ab-initio calculations on a smaller data set of geometric configurations or points. The points were clustered around the transition state region and minimum energy path. The calculated values of bond lengths and included angle for transition states and the well geometry agreed well with Wang et al.[60].

2.4.3 NO₂ system

The ground and several higher electronic states of the NO₂ system have been subjected to numerous studies in the past. Ground state reactants and products are connected through $^2A'$ and $^4A'$ surfaces. Global or small sections of the PES for the NO₂ systems have been reported by several authors [61, 62, 63, 64]. However, many of these may not be suitable for studying the mechanism and calculating the cross-section database of the exchange reactions.

Walch et al.[65] reported a Complete Active Space SCF/ Contracted CI PES for NO₂ and N₂O surfaces using large Gaussian basis sets. In the case of the NO₂ system, a global PES for the $^2A'$ surface and calculation along the minimum energy path (MEP) for $^4A'$ are documented. The forward exchange reaction was found to be exoergic in nature. In the entry channel of the MEP, an early barrier of 10.2 kcal/mol on the $^2A'$ surface and a barrier of 18.0 kcal/mol on the $^4A'$ surface was established. It can be concluded that the forward exchange reaction primarily takes place on the $^2A'$ surface due to the difference in the barrier heights, especially at lower translational energy.

Gilibert et al.[66] reported an analytical Sorbie-Murrell function on the lowest $^2A'$ surface using the then available ab-initio data and spectroscopic data. The authors have used this surface for Quasi-Classical Trajectory studies and have reported reproduction of experimental reaction rate coefficients.

Sayos et al.[67] generated new $^2A'$ and $^4A'$ surfaces using CASSCF method followed by second order perturbation method (CASPT2). An active space of 17 active electron and 12 active orbitals with Dunning style G2/aug-cc-pVTZ basis set were used for the calculations. In addition to these, experimental data for the exoergicity and dissociation enthalpy of O_2 molecule were used to appropriately modify the ab-initio $^2A'$ PES. The topography of the system at C_s and near C_{2v} symmetries were detailed. Many previously unreported transition points were reported and tabulated for both the surfaces. The authors observed that the barrier height along the MEP of the forward exchange reaction on the $^4A'$ surface was lower than the corresponding value calculated by Walch and Jaffe[65]. This results in higher contribution of the trajectories on $^4A'$ surface towards the reaction rate coefficient.

Varandas et al.[68] reported a multi-sheeted Double Many Body Expansion (DMBE) PES for the $^2A'$ state. The authors have calibrated 8×8 DMBE PES to match the important topological features of the NO_2 system. The DMBE surface has been used widely for QCT studies of the exchange reaction.

Kurkal et al.[69] reported a global PES for the ground (1A_1) and the first excited state (2B_2) of NO_2 using multireference configuration interaction calculation and Dunning style aug-cc-pVQZ. The surface was intended to study the dissociation of $NO_2 \rightarrow N + O_2$ and accurately predicted the dissociation energy. The frequencies of different vibrational modes calculated using the generated PES matched well with the experimental values.

At higher energies, the reactants often transport to higher electronic states and the reaction takes place on higher electronic states. Braunstein and Duff[70] calculated PESs for the reaction $N(^2D) + O_2(X^3\Sigma_g^-) \rightarrow NO + O$. The products formed are at their respective ground states. Gonzalez et al.[71] also reported CASSCF/CASPT2 PES for the same reaction and further performed variational transition state theory (VTST) and quasiclassical trajectory (QCT) methods calculations to study the kinetics and dynamics of the reaction.

2.4.4 N_2O system

The PES required to study the N_2 -O collisions is the N_2O PES. The ground state reactants and products are connected through $^3A'$ and $^3A''$ surfaces. Similar to the NO_2 system, many authors have reported PESs[72, 73] for the N_2O system. Walch and Jaffe[65] reported CASSCF/CCI calculations for the two lowest N_2O surfaces. The PESs have been widely used to study the dynamics and kinetics of the reaction. A barrier height of 0.5

kcal/mol and 14.4 kcal/mol relative to $\text{NO} + \text{N}$ were found at the exit channel on the ${}^3A'$ and ${}^3A''$ respectively. It was observed that the reverse reaction $\text{NO} + \text{N} \rightarrow \text{N}_2 + \text{O}$ predominantly takes place on ${}^3A''$ surface.

Recently, Lin et al.[74] reported a state of the art PES for the lowest ${}^3A'$ and ${}^3A''$ using MRCI/state averaged SA-CASSCF. Only 2p electrons are considered in the active space. The ten active electrons and nine active orbitals make up the active space. Dunning style maug-cc-pVTZ basis set was used for the calculations. Calculations are performed at 2280 and 2298 points on the ${}^3A'$ and ${}^3A''$ respectively. A permutationally invariant polynomial using mixed exponential Gaussian variables was used to fit the data. The analytical expression of the two surfaces is available on Potlib[75]. Various topographical features such as the transition points, local minima, and minimum energy paths for the exchange reaction on the two surfaces are further explained in detail.

2.4.5 O_4 system

O_4 PES topography has been a topic of interest and many authors have reported either a global PES or a part of it. Lauvergnat et al.[76] constructed a global triplet O_4 PES using internally contracted Multireference configuration interaction (icMRCI) using 6-311G (2d,f) basis set. The computations were carried out using an active space of 6 electrons and 6 orbitals (CAS(6,6)). It was argued that the basis set chosen and the choice of the active space were inadequate. As a result, equilibrium bond lengths for the $\text{O}_2 + \text{O}_2$ stationary point were unequal. In addition to this, the optimized lengths for the $\text{O}_3 + \text{O}$ C_{2v} state were also unequal.

Hernandez-Lamonedada et al.[77] reported ab-initio results for ground state and low lying electronic states for the reverse reaction (Reaction $\text{O}_2(v > 25) + \text{O}_2 \rightarrow \text{O}_3 + \text{O}$) along the minimum energy path (MEP) using icMRCI and atomic natural orbitals (ANO) and a more intensive active space (CAS(16,12)). PES crossings between the singlet and triplet states were observed. It was observed that non-adiabatic effects play an important role in ozone deficit effect. Although the choice of the active space was superior, the calculations were only along the MEP and hence cannot be used to study the oxygen dissociation (Reaction $\text{O}_2 + \text{O}_2 \rightarrow \text{O}_2 + \text{O} + \text{O}$) reaction that requires a global PES.

Varandas et al.[78] reported a Double Many Body Expansion (DMBE) PES constructed using MRCI ab-initio calculations, data from previous surfaces and a recommended estimate of the barrier height in the MEP. The work experimented with different active spaces (CAS(6,6), CAS(8,8), CAS(16,12)) and concluded that CAS(8,8) was the smallest active space sufficient to describe all reaction channels. Also, this was the small-

est active space with equal bond lengths for stationary points O_2+O_2 and O_3+O unlike the CAS(6,6) active space used in the PES by Lauvergnat et al.[76] that did not lead to the correct bond lengths.

Recently, Paukku et al.[79] have published a state of the art MS-CASPT2/maug-cc-pVTZ global O_4 PES for singlet and quintet spin states. Permutationally invariant global fits using mixed exponential Gaussian functions for the surfaces are available at POTLIB[75]. The PES is suitable for studying ro-vibrational energy exchange and dissociations for high energy O_2-O_2 collisions.

In addition to these global PESs, many studies on reduced four dimensional PESs on the O_4 system with rigid O_2-O_2 dimer configurations have been carried out[80, 81, 82]. Bartolomei et al.[81, 82] have reported spherical harmonic expansion of singlet, triplet and quintet spin multiplicities of O_2-O_2 dimer using restricted coupled-cluster theory with singles, doubles, and perturbation triple excitations (RCCSD(T)). The interatomic distance between the atoms forming O_2 are fixed at equilibrium distance. Though many interesting phenomena in the fields of laser technology and condensed matter physics can be studied using their PESs, the 4D PESs are unsuitable for studying bond breaking and bond formation.

2.4.6 N_4 PES

The N_4 PES is a six-dimensional surface and is a more complicated system when compared to the three atom system. Paukku et al.[83] have used Complete Active Space Self Consistent Field (CASSCF) and Complete Active Space Second Order Perturbation Theory (CASPT2) to develop a state of the art global N_4 PES to study the dissociation more accurately. A Fortran code for the permutationally invariant global least square fit of the PES is available on POTLIB[75].

Selecting appropriate active space and active orbitals for CASSCF-CASPT2 method is critical for accuracy and computational cost. Paukku et al.[83] have placed only 2p orbitals in the active space. An active space of 12 electrons and 12 orbitals (12e/12o) was selected for the system. Minimally augmented Dunning style basis set (maug-cc-pVTZ) was used for all calculations carried out on MOLPRO computational chemistry package.

2.4.7 N_2O_2 system

A combination of Complete Active Space SCF (CASSCF) and second order perturbation theory (CASPT2) has been used by Varga et al.[84] in construction of a state of the art

global triplet spin state N_2O_2 PES. The active space used consists of 14 active electrons comprising of 2p electrons of the two nitrogen and the two oxygen atoms, and 12 active orbitals. Dunning style minimally augmented correlation-consistent polarized valence triple-zeta (maug-cc-pVTZ) basis set is used in construction of the six dimensional surface using a total of 54889 geometries. A permutationally invariant fitting function of the N_2O_2 surface is available on PotLIB[75].

2.5 Summary

It can be concluded that the widely used phenomenological methods for modelling chemical reactions in DSMC are not reliable in situations with high degree of non-equilibrium. There is a need and scope for improvement in the area of non-equilibrium chemical reaction modelling. A new ab-initio based chemical reaction model is proposed which employs computational chemistry algorithms to generate PESs which are used to calculate reactive cross-section using the QCT method. Accurate N_4 , N_2O_2 , NO_2 and N_2O PESs are available on the PES library: PotLIB. In addition to these systems, new PESs for O_4 , N_3 , and O_3 are constructed using the MolCAS computational chemistry package. Details of the ab-initio calculations and validation with experimental data is presented in Chapter 4. The reactive cross-sections for dissociation and exchange, listed in Table 2.2, are generated using the accurate PESs.

Chapter 3

Computational Methodology

3.1 MolCAS Ab-initio Package

University edition MolCAS 8.0 computational chemistry package includes Multi-configurational Self-Consistent Field (MC-SCF) methods such as Complete Active Space SCF method (CASSCF) and second order Complete Active Space Perturbation Theory (CASPT2). Coordinates of the atoms comprising the system, spin of the system, details regarding basis set and parameters for the CASSCF and CASPT2 methods are input to a MolCAS code. MolCAS ab-initio Package solves the electronic Schrödinger equation given the position of the nuclei and the number of electrons.

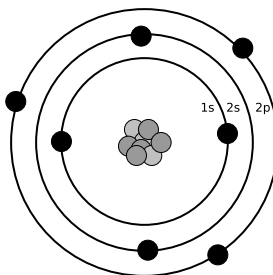
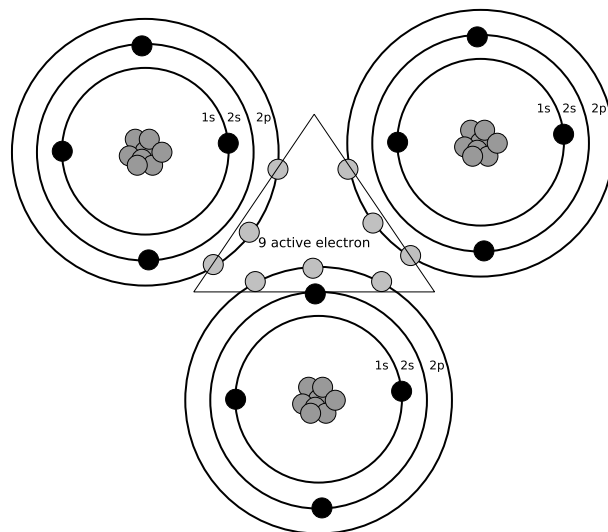


Figure 3.1: Atomic structure of an Nitrogen atom.

The spin state (**Spin**) of the system, number of active electrons (**Nactel**), number of inactive pairs of electrons (**Inactive**) and active orbitals (**RAS2**) are required for CASSCF calculations. As an illustration, consider CASSCF calculation for an N_3 configuration. The N atom has 7 electrons residing in $1s$, $2s$ and $2p$ electron shells in its ground state as shown in Figure 3.1. $1s$ and $2s$ are fully occupied and the electrons residing in these orbitals can be assumed to be inactive. In total, 6 pairs of electrons in the N_3 system are inactive. The remaining 9 electrons reside in $2p$ orbitals as shown in Figure 3.2. The spin of the system ($S = 2\Sigma s + 1$) is the sum of spins ($s = 1/2$ or $-1/2$) of the active electrons. In the ground state, the spin state of the N_3 system is equal to 2 ($2 \times 1/2 + 1$). The choice of active orbitals depends on the system in question. In the present work for

Figure 3.2: Molecular structure of a N_3 system.

constructing PESs pertaining to air chemistry, the numbers of active orbitals chosen for various systems are obtained from literature.

Table 3.1: Active space chosen for CASSCF calculation for various systems in air chemistry

System	Inactive electron pairs	Active electrons	Active Orbitals	Reference
N_3	6	9	9	Mankodi et al.[85]
O_3	6	12	9	Mankodi et al.[85] Varga et al.[86]
N_2O	6	10	9	Lin et al.[74]
NO_2	6	11	9	Sayos et al.[67]
N_4	8	12	12	Mankodi et al.[87] Paukku et al.[83]
O_4	8	16	12	Mankodi et al.[87] Paukku et al.[79] Paukku et al.[88]
N_2O_2	8	14	12	Varga et al.[84]

The O_3 system has exactly the same number of inactive pair of electrons as the N_3 system. However, the Oxygen atom has four active electrons in its last $2p$ shell. Thus, there are 12 active electrons for the O_3 system and it is reported that 9 active orbitals are sufficient for CASSCF calculations. The other three atom systems, namely N_2O and

NO_2 , also have the same number of pairs of inactive electrons. N_2O and NO_2 have 10 and 11 active electrons respectively. The four atom systems, N_4 , O_4 and N_2O_2 each have 8 pairs of inactive electrons. The number of active electrons for N_4 , O_4 and N_2O_2 are 12, 16 and 14 respectively. In essence, only 2p electrons are part of the active space for CASSCF calculations. The details of the active space and references of the source of the PES are tabulated in Table 3.1. CASPT2 follows the CASSCF calculation.

3.2 QCT Method Code

The reactive cross-section database is generated by simulating a large ensemble of runs using the Quasi-classical Trajectory (QCT) method. The overall algorithm of the QCT method is detailed in Chapter 2. In the present chapter, the procedure for initialization and analysis of a trajectory are described.

3.2.1 Initializing a trajectory

The major reactions in the Air chemistry listed in Table 2.2 can be classified on the basis of number of atoms involved in the interaction. The reactions occur either through atom-molecule or molecule-molecule collisions. Further, the molecules involved are diatomic molecules only. The atom-molecule collisions traversing on a three dimensional PES can lead to dissociation of the molecule or exchange of the atom with one of the constituent atoms forming the molecule. In contrast, the molecule-molecule collisions traversing on a four-atom six-dimensional PES lead to dissociation of one or both the molecules. There also could be an exchange of atoms.

Initializing the space (q) and momenta (p) variables is essential in starting a trajectory. In the case of atom-molecule collision, the space variables of the atoms in the molecule are set about the origin of the coordinate system. The third atom is placed at a distance far from the origin where it does not experience any effect of the molecule at the origin. The relative translational energy of the trajectory is added as the momentum of this atom directed towards the origin. The internal energy comprising of rotational and vibrational energies is added through the molecule at the origin. The diatomic molecule rotates and vibrates about the centre. At either extremum of the periodic motion, the momentum of the atoms about the centre of vibration is zero. At this point, the momentum of the atoms is purely due to rotational component of the internal energy. These points are known as turning radii (r_{\pm}). Different ro-vibrational levels have different sets of turning radii. The value of the turning radii is calculated by solving the vibrational Schrödinger

equation for diatomic molecules:

$$\left[-\frac{\hbar^2}{2\mu} \frac{d^2}{dr^2} + V_{eff}(r, j) - e_{v,j} \right] \psi(r) = 0 \quad (3.1)$$

where \hbar is the Planck's constant divided by 2π , μ is the reduced mass of the diatomic molecule, ψ is the wavefunction, $e_{v,j}$ is the internal energy at j rotational level and v vibrational level.

$V_{eff}(r, j)$ is the effective potential energy which is the sum of potential energy and rotational energy, and is given by:

$$V_{eff}(r, j) = V(r) + \frac{j(j+1)\hbar^2}{2\mu r^2} \quad (3.2)$$

where $V(r)$ is generally in the Morse potential form. In contrast to the attractive-repulsive behaviour of the potential ($V(r)$), the contribution of rotational energy to the effective potential is repulsive in nature. Beyond a certain rotational level (j_{max}), the effective potential will be of purely repulsive nature. For all rotational levels greater than j_{max} the molecular identity is lost and it is said to be in a dissociated state. In the case of Nitrogen and Oxygen molecules, the total number of possible rotational levels, j_{max} , are 279 and 212 respectively. For all values of j less than j_{max} , the graph of the effective potential energy will have a global minima and a local maxima as shown in Figure 3.3 for nitrogen molecule. The gradient of the effective potential energy changes its direction at the global minima and a local maxima at a distance greater than the radius at the global minimum internal energy. Calculating the roots of the equation of the gradient using the bisection method yields the radii corresponding to the global minimum and local maximum energy. A simple substitution of the radii in the initial equation will return the minimum and maximum energy possible.

The Schrödinger equation, in this case, does not have a simple analytical solution because the form of $V_{eff}(r, j)$ is complex. However using the semi-classical Wentzel-Brillouin-Kramers (WKB)[89, 90] method, an approximation can be made to generate a simpler integral relation of the form:

$$v = -\frac{1}{2} + \frac{(2\mu)^2}{\pi\hbar} \int_{r_-}^{r_+} (e_{v,j} - V_{eff}(r, j))^{1/2} dr \quad (3.3)$$

Initially, the maximum internal energy for a rotational level j , as calculated using

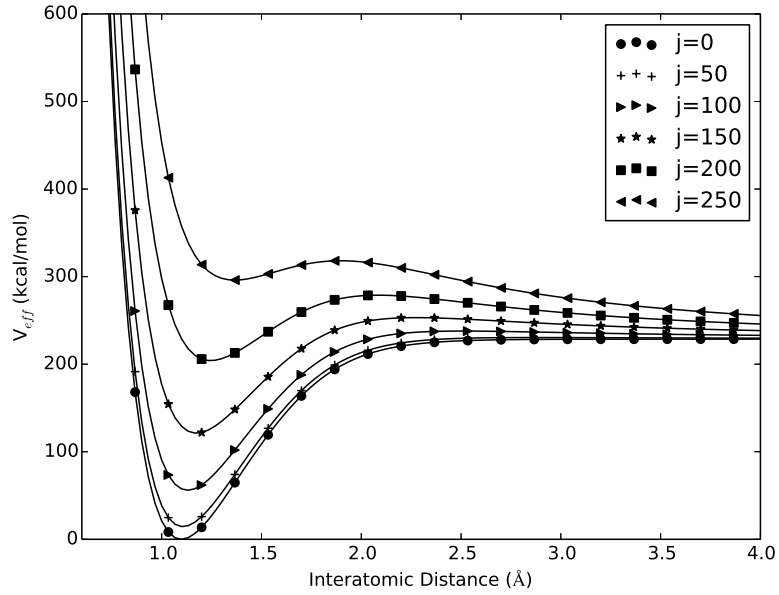


Figure 3.3: Effective Potential Energy Curve at different rotational levels for Nitrogen molecule.

the procedure outlined in the paragraph above, is used to calculate turning points r_+ and r_- . The turning points and maximum internal energy are substituted in the above equation which is further numerically integrated using the Trapezoidal method. The floor value of the right hand side of the equation calculates the maximum possible vibrational level ($v_{max}(j)$) for the given rotational level (j). The values of internal energy ($e_{v,j}$) are iteratively adjusted so as to get the final result of the right hand side converge to an integer value corresponding to the vibrational levels ($\in (0, v_{max}(j))$). The values of turning points and internal energy for the entire range of ro-vibrational levels are enumerated.

Rovibrational states that have an internal energy ($e_{v,j}$) greater than the dissociation enthalpy are classified as unbound states, while the remaining states are classified as bound states. For nitrogen, the maximum vibrational level for $j = 0$ rotational level is 55, the number of bound states are 6990 while the unbound states are 2000 adding up to a total of 8990 states. In contrast, for oxygen, the maximum vibrational level for $j = 0$ rotational level is 37, while the number of bound and unbound states are 4221 and 1125 respectively. Further, only odd number rotational levels are acceptable for oxygen molecule. The maximum vibrational level for Oxygen is in a good match with the experimental findings ($v_{max} = 36$) and is an improvement over previous simulation results [34, 91]. For the nitrogen system, there is a small difference with existing values [90, 56] for the number of bound and unbound states. However, it has been argued previously that this change can be attributed to numerical methods employed and the interpolation techniques of the potential energy curve. In addition to this, as the internal energy increases, the states are closely spaced and often regarded as a band instead of distinct lines in spectroscopy. It is

safe to assume that the effect of this difference in closely spaced higher ro-vibrational levels would not be menacing on the reactive cross section obtained using the QCT algorithm.

The space coordinates of the atoms forming the molecule are placed at half the turning radii centred about the origin with a random polar and azimuthal angle. The momentum of the atoms forming the molecule is set to the rotational energy corresponding to the rotational level of the molecule. In the molecule-molecule collision, the internal energy of the incoming molecule that is placed at a distance far from the origin is set in the same manner. However, it must be mentioned that the momenta and space coordinate of this second molecule are set according to its ro-vibrational level.

The paths of the centre of gravity of the colliding particles may not intersect leading to the concept of impact parameter. The impact parameter is defined as the perpendicular distance between the path of the incoming particle and the center of a potential field created by the molecule at the origin. The impact parameter (b) for a trajectory is randomly sampled using the relation $b = \xi^{1/2}b_{max}$ where b_{max} is the maximum impact parameter and ξ is a random number between 0 and 1. The maximum impact parameter is set to 8\AA for all trajectories involving atom-molecule collisions and 14\AA for molecule-molecule collisions. In the simulation, the space coordinate of the incoming particle is adjusted accordingly.

3.2.2 Time Integrator

With the above initial conditions, Hamilton's equations are numerically integrated to get the time evolution of the system. The choice of the time integrator is important for any partial differential equation. The time evolution of a Hamiltonian system is symplectomorphic and it is justified to use a symplectic integrator for the set of equations. Generally higher order Runge Kutta (RK) methods are used as time integrator. The standard RK-4 method is not a symplectic integrator. Hence, higher order symplectic integrators were also tested. These integrators were both computationally accurate and costly compared to a second order Verlet algorithm[92]. However, the latter was chosen as the time integrator since the outcome of the trajectory run was not affected by the order of the algorithm as long as the integrator was symplectic. The Verlet algorithm comprises of three steps:

$$p_{i,j}^{N+1/2} = p_{i,j}^N + \frac{1}{2} \frac{\partial \mathcal{V}}{\partial q_{i,j}^N} \Delta t \quad (3.4)$$

$$q_{i,j}^{N+1} = q_{i,j}^N + \frac{p_{i,j}^{N+1/2}}{m_i} \Delta t \quad (3.5)$$

$$p_{i,j}^{N+1} = p_{i,j}^{N+1/2} + \frac{1}{2} \frac{\partial \mathcal{V}}{\partial q_{i,j}^{N+1}} \Delta t \quad (3.6)$$

where the first letter of the subscripts $\{i, j\}$ denotes the atom and second denotes the coordinate ($j = x$ or y or z), and the superscripts $N, N + 1/2$ and $N + 1$ denote the time at the previous, intermediate and the new iteration respectively. It is noteworthy that evaluation of derivative of the potential is carried out twice for a single Verlet step.

3.2.3 Outcome of a trajectory

As time progresses, the colliding particles move toward each other. The sum of the distances between the pairs of atoms reduces. After the interaction is complete, the particles keep moving away from each other and the sum of the distances between the pairs of atoms increases. The trajectory is said to reach completion when the sum of the new distances is greater than the sum of the distances at the initial moment ($t=0$). The distances between the pair of atoms at the end of a run is used to check if the collision has resulted in a reaction or not.

The possible outcomes for an atom-molecule trajectory are:

- no reactions and no change in ro-vibrational level of the molecule
- no reaction but change in ro-vibrational level of the molecule
- the atom exchanges its place with one of the atoms of the molecule
- the molecule dissociates to give three separate atoms.

In contrast, a molecule-molecule interaction can result into many more outcomes.

- no reactions and no change in ro-vibrational level of any molecule
- no reaction but change in ro-vibrational level of one of the molecules
- no reaction but change in ro-vibrational level of both the molecules
- exchange reaction
- one of the molecules dissociates and no change in ro-vibrational level of the other molecule
- one of the molecule dissociates and change in ro-vibrational level of the other molecule

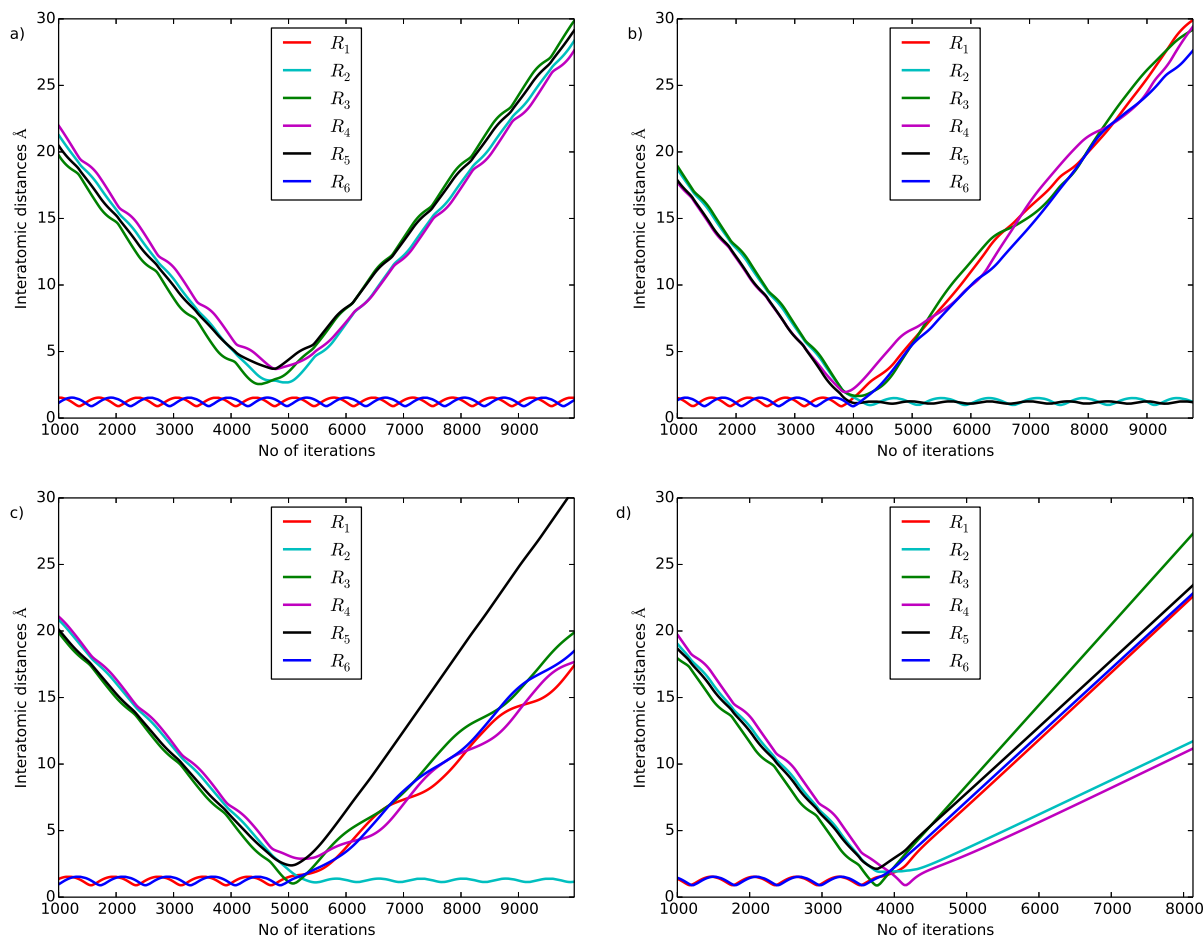


Figure 3.4: Graphical representation of a few of the possible outcomes for a QCT trial for the $N_2 + N_2$ reaction: a) no reaction, b) exchange reaction, c) single dissociation and d) double dissociation

- two dissociated atoms and formation of one molecule comprising of atoms from different molecules.
- both molecules dissociate

Figure 3.4 presents a pictorial view of four of the different possible outcomes for the N_2-N_2 interaction. Each sub-figure displays the time evolution (on x axis) for different interatomic distances (R_1-R_6). For all the cases represented in Figure 3.4, the molecules are initialized at $v=20$ and $j=0$. The distances represented by R_1 and R_6 are the interatomic distance between the pair of atoms forming a molecule.

3.2.4 Cross-section

A large ensemble is simulated for a particular ro-vibrational level for an atom-molecule collision or a combination of ro-vibrational levels for a molecule-molecule collision at some

value of the relative translational energy. This ensemble is used to calculate the reaction probability and reactive cross-section data. The reaction probability is the fraction of the trajectories that result in a reaction to the total number of trajectories in an ensemble. The reactive cross-section is an effective area used to indicate the measure of the probability for a collision to result in a successful chemical reaction. The reactive cross-section for an ensemble of trajectories in the case of atom-molecule reactions is:

$$\sigma_R(v, j, V_R) = (\pi b_{max})^2 \frac{N_R(j, v, V_R)}{N(j, v, V_R)} \quad (3.7)$$

where v is the vibrational level, j is the rotational level, V_R is the relative speed, N is the total number of trajectories progressed and N_R is the number of trajectories that result in a successful dissociation.

In the molecule-molecule reactions, the reactive cross-section (σ_R) is a function of the rotational and vibrational levels of both molecules, and the relative velocity. It is calculated as:

$$\sigma_R(v_1, j_1, v_2, j_2, V_R) = \pi b_{max}^2 \frac{N_R(v_1, j_1, v_2, j_2, V_R)}{N_T(v_1, j_1, v_2, j_2, V_R)} \quad (3.8)$$

As the QCT method is statistical, it is also important to evaluate scatter in the data to check if the reactive cross-section data is reliable or not. The scatter ($\Delta\sigma_R$) in the reactive cross-section (σ_R) is calculated using the expression:

$$\Delta\sigma_R = \sigma_R \times \left(\frac{N - N_R}{NN_R} \right) \quad (3.9)$$

As can be observed from the equation, the scatter reduces with increase in the size of the ensemble.

3.3 DSMC Code

3.3.1 Determining computational parameters

DSMC simulations are performed for studying hypersonic flow over a re-entry vehicle at a specified altitude. Assuming Eulerian approach, the inlet gas with a composition corresponding to the given altitude flows toward the vehicle with stream velocity equal to the re-entry speed. Properties such as pressure (P) or number density (n), temperature (T) of the ambient atmosphere at the altitude, and the re-entry speed (U_∞) and angle of attack (θ_{AOA}) of the inlet flow are the necessary input conditions. Generally, at altitudes around 70 km, the ambient pressure has a value around 1 or 10 Pa, while the temperature is around 200 K.

The first step in a DSMC simulation is to calculate various computational parameters such as the number of cells in the domain, time-step and number of particles per cell using the input variables. A principle assumption of the DSMC algorithm is that the cells should have lengths less than the mean free path and the time-step should be less than the mean collision time in order to justify decoupling of the movement and collision processes. The mean free path (λ) and mean collision time (t_c) are calculated using:

$$\lambda = \frac{1}{\sqrt{2}\pi d_{ref}^2 n} \quad (3.10)$$

$$t_c = \frac{1}{4\pi d_{ref}^2 n \sqrt{\left(\frac{\pi k_b T_{ref}}{m}\right) \left(\frac{T}{T_{ref}}\right)^{1-\omega}}} \quad (3.11)$$

where d_{ref} , T_{ref} and ω are the Variable Hard Sphere (VHS) model parameters: reference diameter, reference temperature and viscosity parameter respectively. These parameters are available for the common gases and tabulated in Appendix IV, [2].

The cell size and time-step for the DSMC simulation for a given set of ambient conditions is calculated using the formulae:

$$\Delta x = p \times \lambda \quad (3.12)$$

$$\Delta t = p \times t_c \quad (3.13)$$

where p is a fraction generally less than 1/3. The number of cells in each dimension (N_x, N_y, N_z) is determined from the cell width values.

3.3.2 Describing a DSMC particle

In DSMC, each simulated particle represents a large number of real molecules. The number density and the cell size information is available. Traditionally, it was accepted that there should be around 20 DSMC particles per cell. However, recently developed sophisticated DSMC procedures suggest that this number should be around 8. It is evident that the product of the volume of the cell ($\Delta x \Delta y \Delta z$) and the number density is equal to the number of real particles in the cell. Therefore continuing with these DSMC procedures, the total number of real particles that a DSMC particle represents is calculated as:

$$Z = \frac{n \Delta x \Delta y \Delta z}{8} \quad (3.14)$$

A list of particles is maintained during the simulation. A particle is a zero dimensional point entity. The following information is stored and updated for each particle as the

simulation progresses:

- Position ($\mathbf{X} = \{x, y, z\}$)
- Velocity ($\mathbf{U} = \{u, v, w\}$)
- Rotational Energy (E_R)
- Vibrational Energy Level (v') and Vibrational Energy (E_V)
- Species or species number

Eight particles are placed randomly in each cell of the domain. If a particle lies inside the re-entry vehicle geometry, it is ignored from the list of particles. After every time step, N_{in} particles are placed randomly on the inlet surface.

The velocity of a particle is composed of two constituents: thermal velocity (U_t) and stream (U_∞) velocity. The components of the thermal velocity follow the Maxwell-Boltzmann (M-B) distribution with ambient temperature as the parameter. The components of the thermal velocity ($U_{t,i}$) are sampled from the M-B distribution using Box-Mueller transformation which has the following form:

$$U_{t,i} = \sqrt{-\ln(r_1)} \sin(2\pi r_2) U_{VMP} \quad (3.15)$$

where r_1 and r_2 are randomly generated numbers between 0 and 1, U_{VMP} is the most probable speed of the gas at ambient temperature. U_∞ is added to the thermal velocity to get the particle velocity. New particles entering the domain are initially placed on the inlet surface. These particles are moved according to their velocities for a random fraction of the time-step. Particles that manage to enter the domain are added to the particle list.

In addition to the kinetic energy, polyatomic particles will also possess rotational and vibrational energies. In contrast to rotational levels that form a continuous band, the vibrational energy levels are widely spaced and a quantum model for vibrational energy is necessary. The rotational energy (E_R) and vibrational level (v') are initialized as:

$$E_r = -\ln(r_3) k_b T \quad (3.16)$$

$$v' = -\ln(r_4) T / T_v \quad (3.17)$$

where r_3, r_4 are random numbers. Initially all particles are at ground vibrational level.

3.3.3 Movement module

The position of the particles is updated in each time step using Euler integration. The velocities of the particles remain unchanged during their motion. If a particle exits the domain, it is deleted from the particle list. For particles colliding with the re-entry geometry, coordinate geometry formulations are used to calculate the point of collision on the re-entry surface. The velocity of particles colliding with the geometry change according to the boundary conditions set at the surface. The two most widely used boundary conditions for surface collisions are:

- **Specular Boundary Condition:** The direction of the normal component of the velocity of the colliding particle is reversed and the tangential component is kept unchanged. The rotational and vibrational energy of the particles are also kept unchanged. The energy of the particle before and after colliding with the surface is same and hence there is no exchange of energy with the surface. This boundary condition is not appropriate due to its hypothetical character. The high energy gas molecules in the post-shock region ablate the surface material and this is not captured through this boundary condition.
- **Diffuse Boundary Condition:** The charring process raises the temperature of the surface material to its ablation temperature. The material slowly erodes at this temperature and it is assumed that the surface temperature stays (T_{surf}) at this constant value. The velocity and internal energies of the particle colliding with the surface are reinitialized using the Maxwell-Boltzmann distribution corresponding to the surface temperature as the parameter and take the following form:

$$U_{t,i} = \sqrt{-\ln(r_5)} \sin(2\pi r_2) U_{VMP, T_{surf}} \quad (3.18)$$

$$E_r = -\ln(r_6) k_b T_{surf} \quad (3.19)$$

$$v' = -\ln(r_7) T_{surf} / T_v \quad (3.20)$$

where $U_{VMP, T_{surf}}$ is the most probable speed for a gas at the surface temperature. The difference in the kinetic and internal energy of the particle before and after its collision with the surface is the net energy exchanged with the surface. Adding the energy exchanges of all particles over a unit surface surrounding a location during unit time gives the heat flux at the given location.

3.3.4 Collision Module

Simulating collisions in the flow is the most critical part of the entire DSMC algorithm. For the transport properties to be calculated accurately, a particle in a given cell can

collide only with another particle from the same cell. The collision module for all cells consists of three parts:

- The number of pairs of particles (N_T) in a cell that need to be checked for possible collision is calculated using the No Time Counter (NTC) method (Equation 2.2, Chapter 2).
- Two different particles are randomly chosen from the list of particles belonging to one cell. Once chosen, the same pair of particles is not considered again in the same time-step. The value of total collision cross-section (σ_T) is calculated using the Variable Hard Sphere (VHS) method.

$$\sigma_T = \pi d_{ref}^2 \left(\frac{2k_b T_{ref}}{\mu c_r} \right)^{\frac{\omega}{\Gamma(2-\omega)}} \quad (3.21)$$

where μ is the reduced mass. A random number (R) is compared with the ratio of the product of the total collision cross-section and relative speed ($(\sigma_T c_r)$) and the maximum value of the product of the total collision cross-section and relative speed ($(\sigma_T c_r)_{max}$). If

$$R < \frac{(\sigma_T c_r)}{(\sigma_T c_r)_{max}} \quad (3.22)$$

then the pair of particles is said to undergo collision. Initially $(\sigma_T c_r)_{max}$ is set to a reference value equal to the product of hard sphere (HS) total collision cross-section (πd^2) and most probable speed. As the iterations progress, the value of $(\sigma_T c_r)_{max}$ is updated whenever

$$(\sigma_T c_r) > (\sigma_T c_r)_{max} \quad (3.23)$$

- The post collision velocity of the two particles (say 1 and 2) are calculated using the VHS formula. Velocity of the particle is divided into two components: centre of mass velocity (U_{cm}) and relative velocity (U_{re}).

$$U_{cm,i} = \frac{\mu U_{1,i}}{m_2} + \frac{\mu U_{2,i}}{m_1} \quad (3.24)$$

$$U_{re,i} = U_{2,i} - U_{1,i} \quad (3.25)$$

where $U_{1,i}$, $U_{2,i}$ denote the i^{th} component of velocity of particle 1 and 2 respectively. The centre of mass velocity remains unchanged during a collision. In VHS model, the direction of the relative velocity is revised by randomly sampling a new solid angle. The post-collision relative velocity takes the following form:

$$U_{re,u} = (2r_8 - 1) c_r \quad (3.26)$$

$$U_{re,v} = \sqrt{1 - (2r_8 - 1)^2} \cos(r_9) c_r \quad (3.27)$$

$$U_{re,w} = \sqrt{1 - (2r_8 - 1)^2} \sin(r_9) c_r \quad (3.28)$$

where r_8 and r_9 are random numbers between 0 and 1, and c_r is the magnitude of the relative velocity or relative speed. The final velocities of the two particles is:

$$U_{1,i} = U_{cm,i} + \mu U_{re,i}/m_1 \quad (3.29)$$

$$U_{2,i} = U_{cm,i} - \mu U_{re,i}/m_2 \quad (3.30)$$

Polyatomic particles exchange inelastic energies and this is implemented in DSMC using the Larsen-Borgnakke (LB) model. According to this model, only a fraction of collisions further undergo internal energy exchange. The serial implementation of LB model is the standard way of handling the inelastic energy exchange where the rotational and the vibrational energy of the two particles are updated one after the other. Temperature dependent rotational relaxation number is computed using Equation 2.6, Chapter 2. If a random number (r_{10} between 0 and 1)

$$r_{10} < Z_{rot} \quad (3.31)$$

then the rotational energy of the first particle is updated in the following manner. The relative translational energy (E_T) and the rotational energy (E_R) of the first particle are added to get the total energy (E_{tot}). The new E_T and E_R after the inelastic energy exchange take the following form:

$$E_T = \left(1 - a^{\frac{1}{2-\omega}}\right) E_{tot} \quad (3.32)$$

$$E_R = \left(a^{\frac{1}{2-\omega}}\right) E_{tot} \quad (3.33)$$

This is followed by calculating vibrational relaxation number (Z_V) using Equation 2.7, Chapter 2. A random number is compared with Z_V to check the condition in the same way as the condition involving Z_R . If the collision undergoes vibrational energy exchange, relative translational energy (E_T) and vibrational energy (E_V) of the first particle are added to get the total energy (E_{tot}). Maximum possible vibrational level (v_{max}) corresponding to energy less than the E_{tot} value is calculated as:

$$v_{max} = \left\lfloor \frac{E_{tot}}{k_b T_V} \right\rfloor \quad (3.34)$$

Post collision vibrational level (v') is randomly chosen ($v' \leq v'_{max}$). A random number (r_{11}) is compared with the following fraction (v'_{prob}):

$$v'_{prob} = \left(1 - \frac{v'k_bT_v}{E_{tot}}\right)^{1-\omega} \quad (3.35)$$

Until the following condition

$$r_{11} < v'_{prob} \quad (3.36)$$

is not satisfied, a new post collision vibrational level is chosen. The final vibrational and translational energy after the condition is satisfied is equal to:

$$E_V = v'k_bT_v \quad (3.37)$$

$$E_T = E_{tot} - E_V \quad (3.38)$$

This procedure is repeated for the second particle if it is polyatomic.

3.3.5 Chemical Reaction Modelling

A collision may result into a reaction when the total collision energy is greater than the activation energy required for the reaction. The algorithm of the reaction modelling is outlined in Figure 3.5. The manner in which reactive cross-section is calculated is the basis of various chemical reaction models in DSMC. One of most widely used chemical reaction model, the Total Collision Energy (TCE) model, employs an analytical form of cross-section with pre-calculated parameters specific for a reaction. The formulation and limitations are detailed in Chapter 2. In contrast, the reactive cross-section in the ab-initio based chemical reaction model is obtained from a database generated using the QCT method. The TCE cross-section is a single variable function that employs the sum of the translational, rotational and vibrational energies or total collision energy as the input, whereas the ab-initio based reaction cross-section is a multi-variable function and requires three inputs namely translational energy, rotational level, and the vibrational level. The TCE cross-section is calculated using Equation 2.10 (Chapter 2) whereas the ab-initio based cross-section will use an interpolating function fitting the cross-sections generated by the QCT method. The ratio of the reactive cross-section to the total collision cross-section is defined as reaction probability. A random number is sampled between 0 and 1. If this random number is less than the reaction probability, the collision results in a reaction.

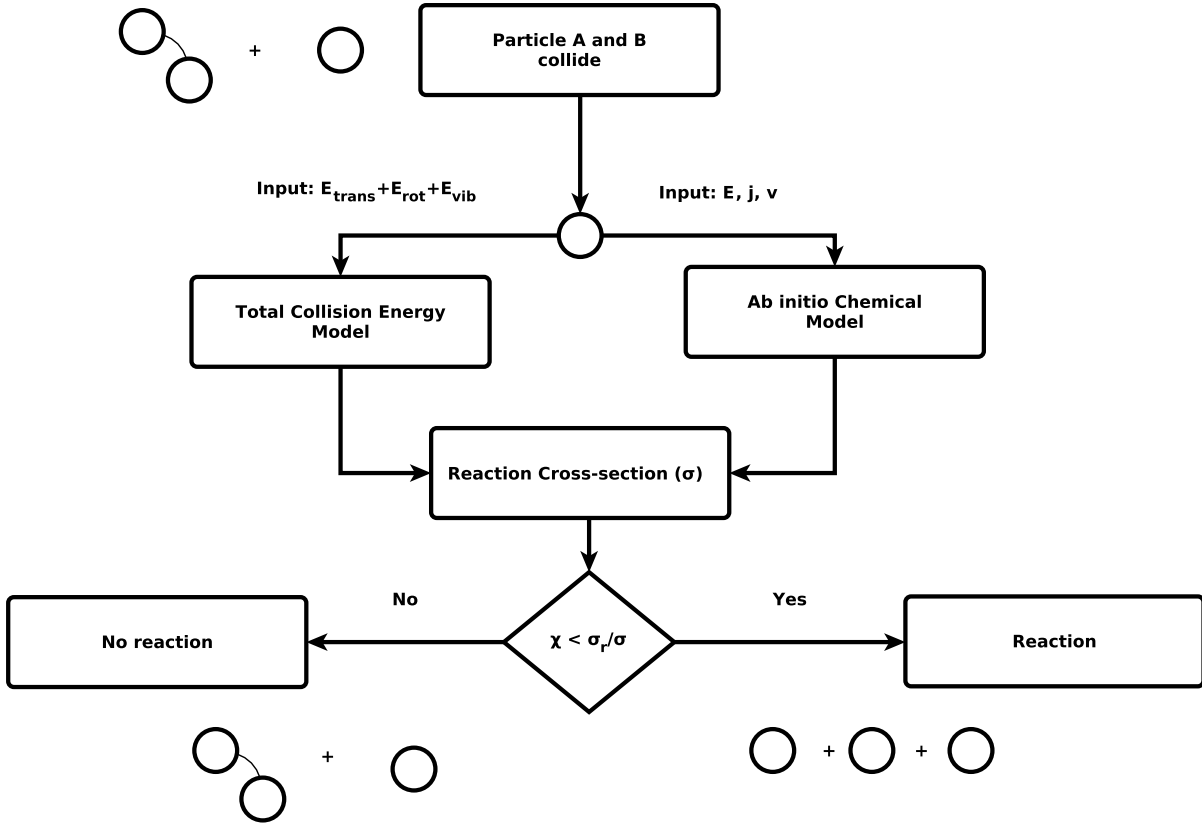


Figure 3.5: Flowchart for chemical reaction modelling in DSMC.

3.3.6 Domain and Boundary Conditions

The geometry of the re-entry vehicle is normally placed at the centre of an appropriately sized domain. The side facing the nose of the re-entry vehicle is the inlet side. After every time-step, new particles are initialized at this inlet side and moved with the re-entry speed towards the object. The number of DSMC particles introduced at the inlet side is equal to:

$$N_{in} = \frac{nAU_{\infty}\Delta t}{Z} \quad (3.39)$$

where A is the area of the inlet side (in 2D simulation, A =length of the side). The integer part of this quantity is the number of particles entering the inlet side. The remainder quantity is carried forward to the next time step and added to the new N_{in} . In case of multi species simulation, N_{in} is a vector instead of a scalar quantity and is calculated using the species number density (n_s).

Vacuum boundary conditions are employed at the remaining surfaces. Generally, the ambient pressure is so low that only a few particles manage to enter the domain from the remaining surfaces. Further, these particles have negligible or negative component of thermal velocity normal to these surfaces. The particles entering through the inlet side dominate the flow in the domain and sweep these few number of particles that manage to

enter through the remaining surfaces out of the domain. The particles entering through the remaining surfaces have no effect on the surface properties of the re-entry vehicle and hence can be ignored from the simulations altogether. The computational domain and the various boundary conditions are shown in Figure 3.6

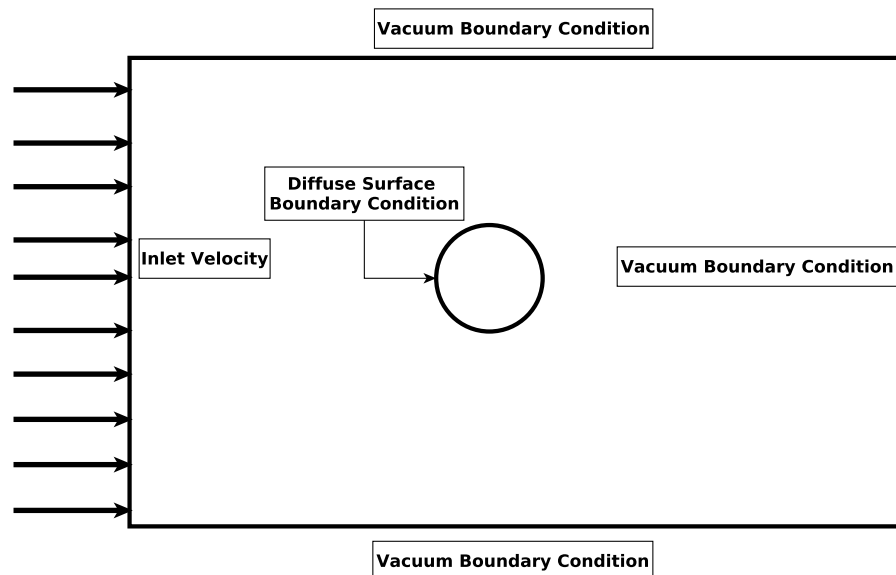


Figure 3.6: Domain and Boundary Conditions.

3.3.7 Sampling Procedure

DSMC algorithm utilizes microscopic quantities of the particles. However, it is the macroscopic quantities in the flow domain and on the surface that help in understanding physics better and in designing aspects. It is obvious that the calculation of macroscopic quantities based on information of a few particles in a single iteration will lead to high scatter and unreliable results. Hence, for better statistics and to reduce scatter, the particle information in any cell is accumulated over a large number of time steps. Standard kinetic theory formulations are used to calculate various quantities such as pressure, density, different modes of temperature, Mach number and Velocity.

3.4 Summary

New PESs are generated using the MolCAS Ab-initio Package. The details regarding its construction, computational effort and results are presented in the next Chapter. The in-house parallelized QCT method code employing these PESs is run to obtain a cross-section database for the various reactions in air chemistry. The data-fitting technique, cross-section results and comparison with equilibrium reaction rate coefficients are explained in Chapter 5. Finally, the cross-section database is employed in the in-house 3D parallel

DSMC code to study non-equilibrium hypersonic flows around re-entry vehicles. The details of the simulations and a comparative study between the chemical reaction models is carried out and the results and conclusions are described in Chapter 6.

Chapter 4

Development of New Potential Energy Surface

New PESs for O_3 , O_4 , N_3 and N_4 systems are constructed using Complete Active Space Self-Consistent Field (CASSCF) and Complete Active Space Perturbation Theory at second order (CASPT2) methods. CASSCF and CASPT2 involve calculation on a subset of all orbitals known as the active space. All calculations are performed using university edition MolCAS 8.0[93, 94, 95] computational chemistry package.

4.1 O_3 PES

A new PES[85] is constructed that employs the CASSCF method to account for the static correlation followed by the CASPT2[96] method to calculate the dynamic correlation. The advantage of CASPT2 is its ability to handle complex systems with practicable computational cost. However, CASPT2 cannot be used as a black box method and needs careful consideration while choosing the appropriate active electrons and active space[25]. Different combinations of active electron (e) and active orbitals (o) (12e/9o, 12e/7o, 12e/12o, 18e/15o, 18e/12o) for a small portion of the PES near the transition region were tested, and it was found that the PES with 12 active electrons consisting of only 2p orbitals of all O atoms and nine active orbitals was reasonably accurate and computationally inexpensive. It has been noted that the proposition of placing only 2p orbitals for such systems as active orbitals is acceptable. Previous PESs also use the same active space. A augmented correlation-consistent polarized valence triple zeta (aug-cc-PVTZ) basis set is employed.

Different points on the O_3 PES are expressed in a coordinate system (shown in Figure 4.1) comprising of the distance between the pair of atoms forming the molecule (R1), distance between the third atom and one of the atoms of the molecule (R2) and the included angle (θ). Let R3 be the length of the third side of the triangle. The distances R1 and R2

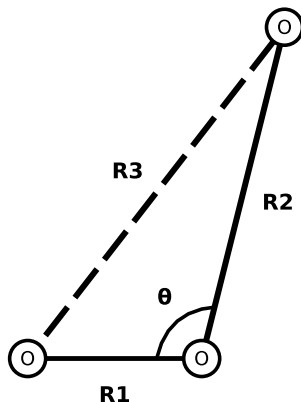


Figure 4.1: Schematic diagram of the coordinate system

are varied from 0.7 Å to 9.0 Å with more points clustered around the equilibrium bond distance of O₂ (1.208Å). θ is distributed evenly between 0 and π in incremental steps of 12°. The various combinations of R1-R2- θ add up to a total of 15376 points. All calculations were performed parallel on Intel Xeon Phi processor and the total computation cost was 1152 CPU hours.

Table 4.1: Comparison of parameters with existing PES for O₃ system

Geometry			
Minima type	C_{2v}		D_{3h}
	R(Å)	θ	R(Å)
Müller[44]	1.27	117.2	1.438
Experiment[46]	1.272	116.8	
Dawes [52]	1.271	116.8	1.436
Present	1.282	114.8	1.449
Energy Differences (kcal/mol)			
Energy Differences	$E(C_{2v})-E(D_{3h})$		$E(C_{2v})-E(O_2)$
			$-E(O)$
Müller[44]	-29.5		-24.5
Experiment[46]			-26.1
Dawes [52]	-30.75		-26.7
Present	-34.4		-23.4

Ab-initio calculations have shown that the O₃ system has a characteristic open minima (C_{2v}) and ring minima (D_{3h}). The existence of the ring minima is yet to be substantiated using experiments. The value of energy separation between the two minima and the dissociation barrier of ozone (C_{2v}) form to O₂ + O and the atomic configuration of the open and ring minima are presented and compared with other computational and available ex-

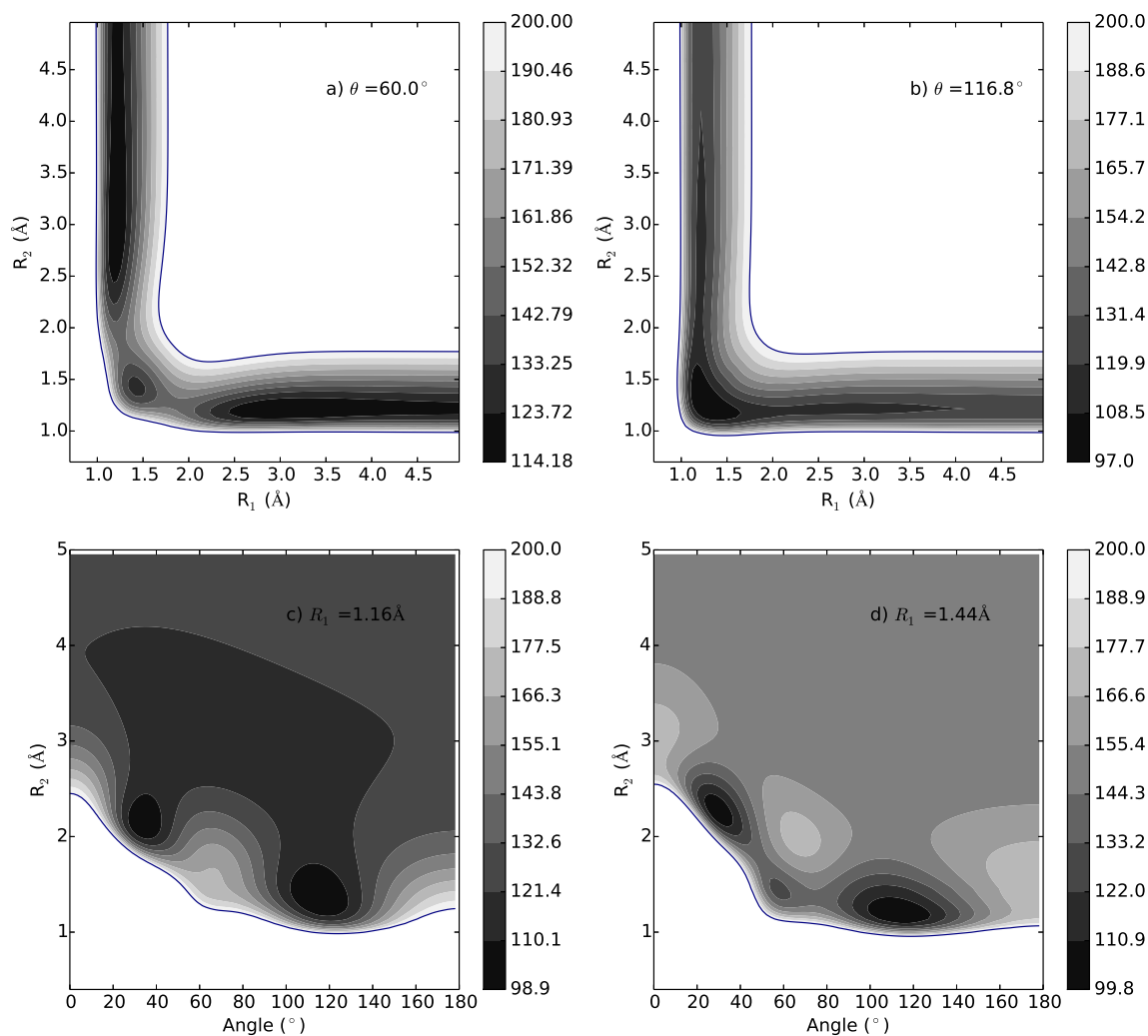


Figure 4.2: Detailed O_3 topography by constraining one of the three parameters (R_1 , R_2 , θ). Sub figure a) and b) show the structure at a fixed included angle of 60° and 116.8° respectively. Sub figure c) and d) show the 2D topography at fixed $R_1 = 1.164196 \text{ \AA}$ and 1.4499532 \AA respectively. Reference energy for the PES $E(O_2+O)=119.2 \text{ kcal/mol}$.

perimental references in Table 4.1. The generated O_3 PES is within reasonable limits of the experimental values and existing computed values. Different two-dimensional contour plots by fixing one of the three variables give us a visual insight in the topography of the PES, as depicted in Figure 4.2. Figure 4.2 a) and b) shows the contour plots with bond lengths (R_1 and R_2) as axes and fixing the included angle at 60° and 116.8° respectively. The adjacent contour lines have a difference of 5 kcal/mol. Figure 4.2 a) and b) shows the ring minima and open minima respectively. Contour plots in Figure 4.2 c) and d) show the structure of PES with fixed R_1 distance and varying included angle. The stationary points at 37° and 117° correspond to two of the three open minima and the point at 60° in Figure 4.2 d) corresponds to the ring minima. The transition state between the C_{2v} and D_{3h} lies at around 75° .

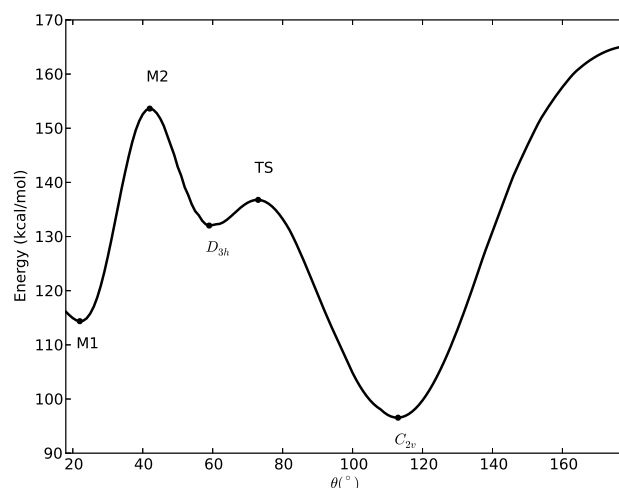


Figure 4.3: Optimized energy profile in C_{2v} symmetry for O_3 system. Different points corresponding to D_{3h} , C_{2v} , TS, local minima and maxima (M1 and M2) are demonstrated on the energy profile. Reference energy for the PES $E(O_2+O)=119.2$ kcal/mol.

The variation of energy with included angle (θ) for C_{2v} configurations with relaxed bond length is shown in Figure 4.3. In addition to the characteristic minima C_{2v} and D_{3h} points, the transition point ($R_1=R_2=1.4$ Å, $\theta = 75^\circ$), local minima M1 ($R_1=R_2=3.2$ Å, $\theta = 24^\circ$) and local maxima ($R_1=R_2=1.8$ Å, $\theta = 44^\circ$) are demonstrated in the energy profile.

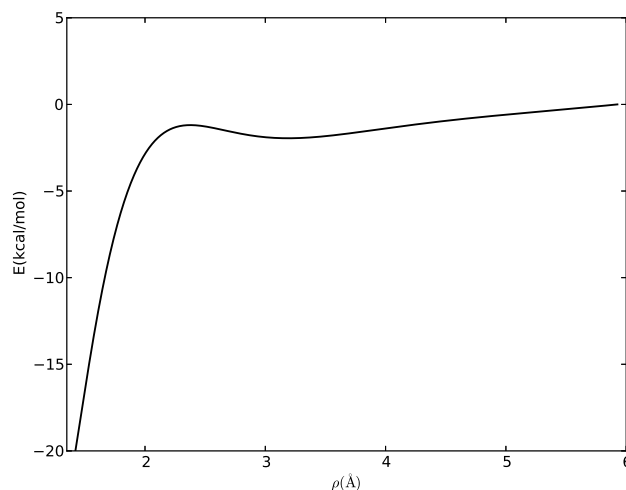


Figure 4.4: Variation of energy (w.r.t. to dissociation threshold) along the minimum energy path (ρ) for ozone dissociation $O_3 \rightarrow O_2 + O$. Reference energy for the PES $E(O_2+O)=0$ kcal/mol

The present PES is constructed with the purpose of studying oxygen dissociation. However, the surface involved in analyzing ozone dissociation is a subspace of the present global PES. Hence, all appropriate features involved in the MEP of ozone dissociation should have a reasonable match with previous works. Many authors have found that the minimum energy path for dissociation of ozone has an unusual reef structure as a result

of an avoided intersection with a higher electronic state. As seen in Figure 4.4, the submerged reef and van der Waal minima are observed along the minimum energy path. The submerged reef is located at $R_1=1.26$ Å, $R_2=2.32$ Å and at a depth of 1.194 kcal/mol below the dissociation threshold. The van der Waals minimum is located at $R_1=1.248$ Å, $R_2=3.19$ Å and at a depth of 1.954 kcal/mol below the dissociation threshold. Tyuterev et.al.[49] and Dawes et.al. [51, 52] have reported PESs with and without the reef structures in their MEP. The PESs without reef structure employ spin orbit correction which has not been included in the present work.

In addition to these features, the present PES estimates accurately the dissociation energy for oxygen molecule at 119.2 kcal/mol (experimental value 119.14 kcal/mol) . The lowest vibrational frequencies for the symmetric, bending and antisymmetric stretch modes are 1109.36 cm^{-1} , 699.99 cm^{-1} and 1048.68 cm^{-1} respectively. The corresponding experimental results[49] for the modes are 1103.14 cm^{-1} , 700.93 cm^{-1} and 1043.9 cm^{-1} respectively and as can be observed the values are a good match.

4.2 N_3 PES

Paukku et al.[83] have constructed a highly accurate global PES for the N_4 system, wherein they calculated energies for a total of 16380 configurations points for various molecular arrangements of N_4 . They have chosen 12e/12o (12 electron, 12 orbital) active space for the CASSCF method and Dunning style augmented correlation-consistent polarized (maug-cc-pVTZ) as the basis set. Different molecular arrangements for N_4 systems were considered in constructing the PES. The PES for the current N_3 system is drawn as a subset of this N_4 global PES.

Paukku et al.[83] have provided a six dimensional global least square fit for the N_4 system. Using a six dimensional surface fit for the N_3 system is unnecessary and computationally expensive. Instead, various points have been obtained for different N_3 configurations from the N_4 global fit and a three dimensional least square fit has been constructed. Quasi-classical Trajectories using the six-dimensional N_4 analytical fit need six times more computational time than that required for trajectories using the three dimensional N_3 analytical fit (initialized at same conditions). The computational gain of using the three dimensional analytical fit over the six dimensional fit is obvious.

An N_3 data point can be visualized as an N_4 configuration with one of the four atoms at a far away distance from the other three atoms so that it has no influence on the potential of the N_3 system. The energy for each configuration is calculated using the global

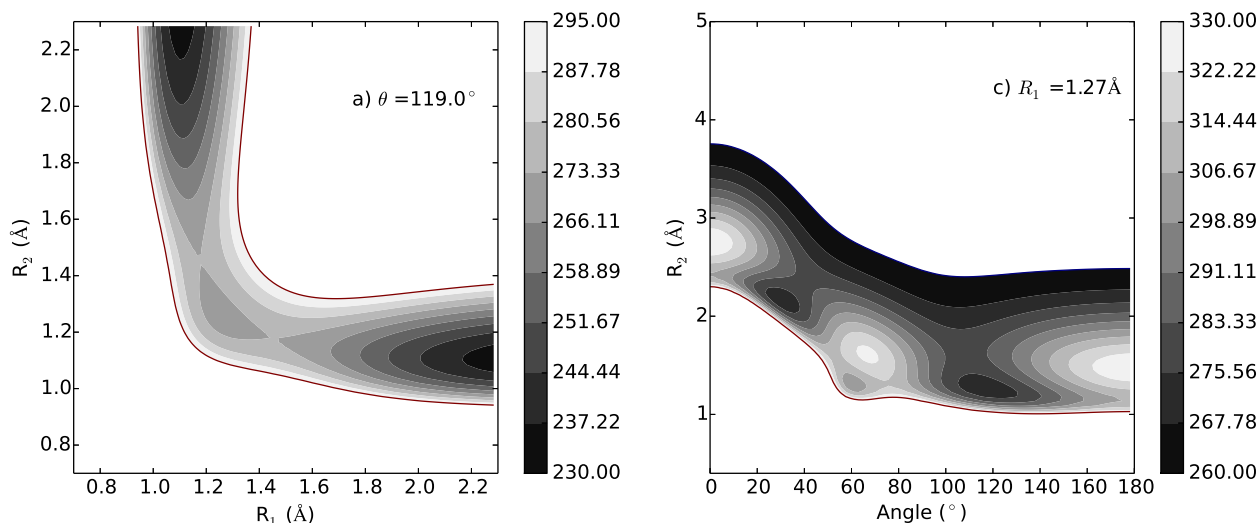


Figure 4.5: 2D Contour plot of N_3 PES with fixed included angle at 119° and varying R_1 - R_2 depicting the transition state and the well structure. Reference energy for the PES $E(N_2+N)=228.7$ kcal/mol.

least square fit[83]. Various configurations of the N_3 system are chosen in the same manner as the ones for the O_3 system (discussed in the previous section). The only point of difference between the two sets of configurations is that points for N_3 are more clustered near the equilibrium distance of the N_2 bond length ($=1.098\text{\AA}$).

Table 4.2: Comparison of parameters with existing PES for N_3 system

	$r_A(\text{\AA})$	$r_B(\text{\AA})$	$\theta(^{\circ})$	$\Delta E(\text{kcal/mol})$ wrt $N_2 + N$
Transition State				
Present	1.18	1.48	119	47.12
Wang[60]	1.184	1.491	117	47.2
Garcia[57]	1.174	1.505	116	47.0
Galvão[97]	1.18	1.46	119	45.9
Well				
Present	1.262	1.262	120	44.66
Wang[60]	1.27	1.27	117	43.7
Garcia[57]	1.268	1.268	119	44.5
Galvão[97]	1.25	1.25	119	42.6

The N_3 PES constructed is a $^4A''$ state. The value of the dissociation energy is 228.7 kcal/mol and is in good match with the experiments (228.47 kcal/mol). Table 4.2 shows the comparison of the position and the energy (relative to the well) of the double barrier transition state between the present and previous PESs. Figure 4.5 shows the two dimensional contour plot with a fixed included angle ($\theta = 120^\circ$) and variable R_1 and R_2 . The

symmetrical transition points and the shallow well are all visible in the contour plot. The shallow well is located at $R_1=R_2=1.262$ Å and $\theta = 120^\circ$. The double barrier transition state geometry is symmetrical about the $R_1=R_2$ line and located at $R_1 = 1.18$ Å, $R_2 = 1.48$ Å and ($\theta = 119^\circ$) at a height of 47.12 kcal/mol. The difference between the shallow well and the transition states is 2.45 kcal/mol. The accuracy of the characteristic points of the N_3 PES is within reasonable limits[60, 57, 97] and this goes to show the robustness of the global N_4 PES.

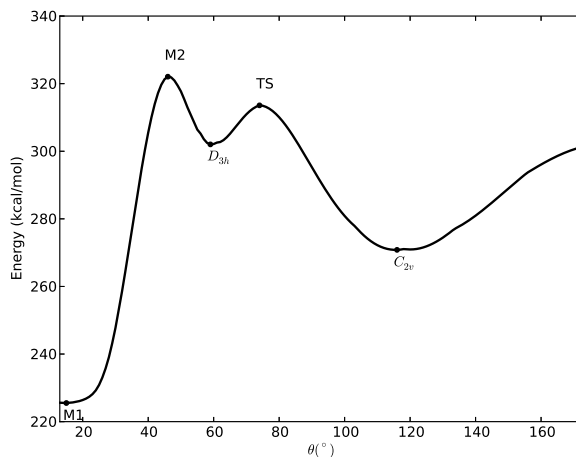


Figure 4.6: Optimized energy profile in C_{2v} symmetry for N_3 system. Different points corresponding to D_{3h} , C_{2v} , TS, local minima and maxima (M1 and M2) are demonstrated on the energy profile. Reference energy for the PES $E(N_2+N)=228.7$ kcal/mol.

Similar to the O_3 system analysis, the variation of energy with included angle (θ) for C_{2v} configurations with relaxed bond length for N_3 system is shown in Figure 4.6. In addition to the characteristic minima C_{2v} and D_{3h} points, the transition point ($R_1=R_2=1.4$ Å, $\theta = 75^\circ$), local minima M1 ($R_1=R_2=3.2$ Å, $\theta = 24^\circ$) and local maxima ($R_1=R_2=1.8$ Å, $\theta = 44^\circ$) are demonstrated in the energy profile.

4.3 O_4 PES

A total of ${}^N C_2$ variables are required to define a constrained N particle system. A geometric configuration, or simply configuration, is an arrangement of N atoms in three dimensional space. This configuration is a point on a ${}^N C_2$ dimensional PES. The problem of determining points on the surface is similar to grid generation in the ${}^N C_2$ space. A common way of generating a grid is by discretization of the domain in the N_i^{th} dimension into n_i cells. The total number of points or configurations using this discretization is:

$$M = \prod_{i=1}^{N C_2} n_i \quad (4.1)$$

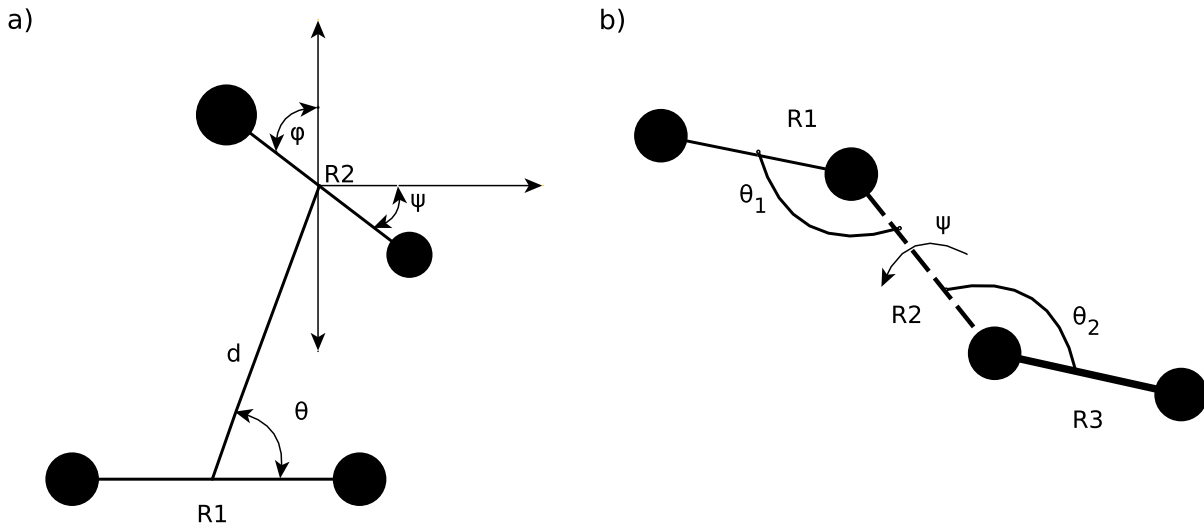


Figure 4.7: Representation of a 4 atom system using the a) $(R1, R2, d, \theta, \phi, \psi)$ and b) $R1, R2, R3, \theta_1, \theta_2$ and ψ coordinate systems.

With increase in the number of dimensions, the number of configurations or points required to cover the space and the computational cost associated with calculating the energy at each point increases sharply. A four atom system is six-dimensional in nature and just ten grid points for each dimension adds up to a total of one million geometries. It is not practical and also not necessary to construct such a dense surface. Instead, an alternative scheme to select points on the PES that are distributed randomly according to simple probability distributions is suggested in this section. The aim of such a scheme is to get the correct topography of the system using fewer points.

Four sides and two diagonals of the quadrilateral constructed by the four points forms a simple six dimensional coordinate system (R1-R6 coordinate system). The formulation for the distances (R1-R6) is as follows:

$$R1 = |\vec{p}_1 - \vec{p}_2| \quad (4.2)$$

$$R2 = |\vec{p}_1 - \vec{p}_3| \quad (4.3)$$

$$R3 = |\vec{p}_1 - \vec{p}_4| \quad (4.4)$$

$$R4 = |\vec{p}_2 - \vec{p}_3| \quad (4.5)$$

$$R5 = |\vec{p}_2 - \vec{p}_4| \quad (4.6)$$

$$R6 = |\vec{p}_3 - \vec{p}_4| \quad (4.7)$$

where $\vec{p}_1, \vec{p}_2, \vec{p}_3$ and \vec{p}_4 represent the Cartesian coordinates for the four Oxygen atoms in three dimensional space. It is easier to work with a coordinate system formed using two opposite sides (R1 and R2), distance between the centres of the opposite sides (d),

the angle subtended by the side of length d with the side of length $R1$ (θ) and pair of azimuthal and polar angles (ϕ and ψ) subtended by the side represented by distance $R2$. A pictorial representation of this coordinate system is shown in Figure 4.7 a. $R1$ and $R2$ are the interatomic distances between the pair of atoms that form the undissociated diatomic molecules when their values correspond to bound states of the diatomic molecules. Points generated for O_4 PESs in the present work are determined using this coordinate system. Another coordinate system for the four atom system (A_4) used in previous works[76, 78] comprises of bond lengths $R1$, $R2$ and $R3$ between atoms A_1 - A_2 , A_2 - A_3 and A_3 - A_4 respectively, valence angles $\angle A_1A_2A_3$ and $\angle A_2A_3A_4$, θ_1 and θ_2 , and dihedral angle ϕ . Pictorial representation of this coordinate system is shown in Figure 4.7 b.

Following the choice given in Figure 4.7 a, the values of $R1$, $R2$, d , θ , ϕ , ψ are chosen using random numbers sampled from an appropriate probability distribution. The choice of the probability distribution function and its parameters is heuristic and information gathered from previously reported surfaces for similar systems assist in making these choices. Observations about the PESs for the corresponding two body (O_2) and three body (O_3) surfaces are used in this process.

The part of the topography of the surface where all its atoms are separated by large distances from each other is generally uninteresting. Similarly, configurations with two pairs of atoms forming molecules that are separated by a large distance also fall in the same category. It is apparent that performing computations at many such points is redundant. It is desirable that fewer configurations of such type are included in constructing a PES. Similarly, the potential energy curve of a diatomic molecule generally has a finite well and asymptotes to a constant value at large interatomic distances. It is obvious that for such systems, the grid constructed should be clustered around the well and minimal beyond the dissociation limit. This principle is valid for the coordinates for the distances ($R1$, $R2$, d) of the four body system.

The distribution should preferably be bounded in nature as the potential energy curve asymptotes as the distances increase. An unbounded distribution with a cap can also be considered. In the present work, the values of the distances $R1$, $R2$ and length d are sampled using the beta distribution. The beta distribution is a continuous two parameter distribution supported on a bounded interval. The probability density function (pdf) for the beta distribution has the following form:

$$f(x : \alpha, \beta) = \frac{\Gamma(\alpha + \beta)}{\Gamma(\alpha)\Gamma(\beta)} x^{\alpha-1} (1-x)^{\beta-1} \quad (4.8)$$

where α , β are parameters also known as shape parameters such that $\alpha, \beta > 0$ and $\Gamma(x)$

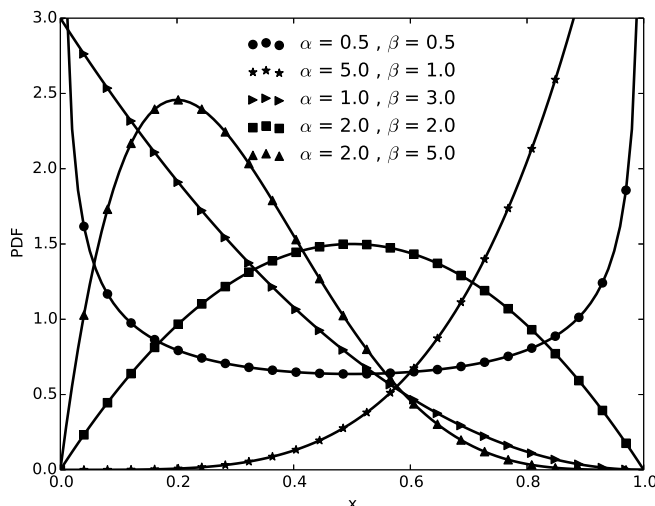


Figure 4.8: Probability density function for beta distribution for different shape parameters α and β .

is the gamma function. Figure 4.8 shows the probability density function for the beta distribution for different shape parameters. As can be observed from Figure 4.8, the advantage of using the beta distribution is that a wide range of shapes of the distribution can be covered with two simple parameters. A suitable choice of the parameters allows extensive flexibility. This is the prime reason for choosing the beta distribution as an appropriate probability distribution function.

The parameters of the beta distribution used in generation of the O_4 PES are determined using the knowledge of the O_2 potential energy curve. The parameters are set such that the peak of the beta distribution coincides with the peak of the gradient of the potential energy curve of the O_2 molecule. A comparison of the gradient of the O_2 potential curve and the beta distribution with parameters ($\alpha = 1.3$, $\beta = 14.8$) is shown in Figure 4.9. The values have different units and scales, and hence these are normalized with respect to the maximum value in the interval of (0.6,15.0). It is possible to choose the parameters such that the two curves coincide in the full domain. However, it is observed that the stationary points on the O_3 surface are located with interatomic distances higher than equilibrium interatomic distance. The D_{3h} has an equilateral triangular shape with the sides equal to 1.45 Å[85]. The parameters are chosen for a broader distribution with a factor of safety of 2 i.e., the beta distribution curve asymptotes at roughly twice the distance at which the gradient asymptotes to zero. The following paragraphs have a comprehensive comparison of the topography of the new PES with previous surfaces and it will be concluded that even with such a high factor of safety, the present surface reproduces the important features of the O_4 topography.

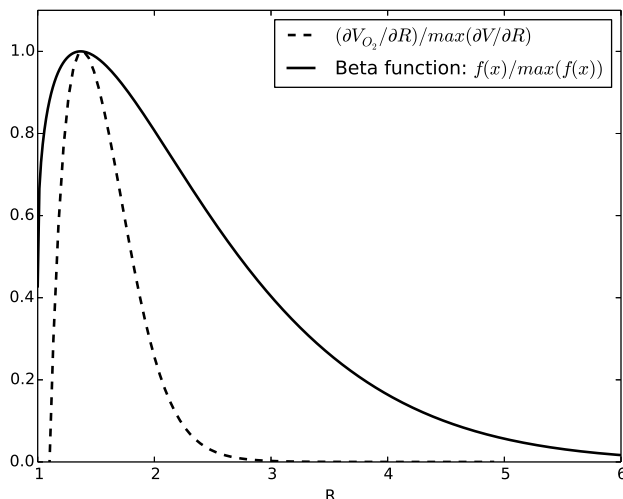


Figure 4.9: Normalized Probability density function for beta distribution and normalized gradient of the Potential Energy Curve of O_2 diatomic molecule.

A large database of random numbers is sampled from the beta distribution function in the interval for $0.6 < x < 15.0$ with parameters $\alpha = 1.3$ and $\beta = 14.8$. In the present work, the same set of parameters are used for R1, R2 and d variables. The domain is divided into five intervals with cell length equal to 0.5 \AA , 0.4 \AA , 0.5 \AA , 3.0 \AA and 10.0 \AA respectively. A total of 125 cells are constructed in three dimensions formed by R1, R2 and d. Thirty sets of R1, R2 and d are sampled randomly for each of the 125 cells from the generated beta distribution database. For each such set of points, the values of the angular coordinates θ , ϕ and ψ are sampled randomly from a uniform distribution with limits $0 < \theta < \pi/2$, $0 < \phi < 2\pi$ and $0 < \psi < \pi$.

In addition to the total 4250 points, two more sets of points are also considered. The first set is constituted of 500 additional points with the value of length R1 fixed at the equilibrium value 1.208 \AA . The second set consists of 250 points with both the values of lengths R1 and R2 fixed at their respective equilibrium values. These sets are added to improve the quality of the fit near the equilibrium bond length. An extra 250 points for the $O_3 + O$ configuration are also added to these using data calculated in the previously constructed O_3 PES[85]. A total of 5250 points are generated for the O_4 system.

As mentioned above, in the present work, the same set of parameters are used for sampling R1, R2 and d coordinates. For hetero-molecular systems, the parameters could be different for different coordinates. In the case of H_2O_2 , R1 is the interatomic distance between the two hydrogen molecules, and R2 represents the O_2 interatomic distance. A recommended set of values for beta parameters for R1 is $\alpha = 1.5$ and $\beta = 4.7$ so that the peak of the normalized beta distribution coincides with the peak of the gradient of the potential energy curve for H_2 molecule. In case of R2, the same parameters as used

in the present paper can be employed. In the case of CO-CO interaction on C₂O₂ PES, the beta parameters for R1 and R2 (interatomic distance between Carbon and Oxygen) should be roughly equal to $\alpha = 1.4$ and $\beta = 8.9$ in the interval (0.7, 10.0).

In addition to the O₄ PES, the point generation scheme is used to construct a global ground state N₄ PES. The parameters used for N₄ PES are $\alpha = 1.4$ and $\beta = 13.0$. The comparison of this PES with the state of the art N₄ PES by Paukku et al.[83] serves as a good validation for the reported point generation scheme.

Multireference second order perturbation theory, CASPT2 is used to account for dynamical corrections following the Complete Active Space Multiconfiguration SCF (CASSCF) method. Paukku et al.[79] have performed calculations using dynamically weighted[98] state averaged CASSCF and Multi State CASPT2. The present PES is generated using single state CASSCF-CASPT2. The choice of active space is critical[25] for CASSCF. An active space of 16 electrons comprising of only 2p orbitals of the four nitrogen atoms and 12 orbitals is used and a level shift equal to 0.4 is used to avoid a problem known as the intruder state problem. In case of systems with closely spaced higher electronic states, it is possible that the solution converges to a value on another electronic state instead of the ground state. This is known as the intruder state problem. Augmented correlation-consistent polarized valence triple zeta basis set (aug-cc-PVTZ) is chosen for calculations. All calculations are performed using university edition MolCAS 8.0[93, 94, 95] computational chemistry package. The total computational time for the 5000 points running in parallel on Intel Xeon workstation was 23000 CPU hours.

Permutationally invariant global least square fit using monomial symmetrization approach [99] is used to fit the data. The coordinates are changed from the (R1, R2, d, θ , ϕ , ψ) coordinate system to R1-R6 coordinate system. The variables ($r_i \in [R1, R2, \dots, R6]$) are converted into Mixed Exponential Gaussian (X_i) and take the following form:

$$X_i = e^{\frac{r_e - r_i}{a_e} + \frac{(r_e - r_i)^2}{b_e}} \quad (4.9)$$

where r_e is the equilibrium bond length ($r_e = 1.208$ Å) and a_e and b_e are non linear parameters ($a_e = 0.9$ Å and $b_e = 4$ Å²). The symbolic expression for the fit is given by:

$$V = \sum_{m=0}^M S[X_1^a X_2^b X_3^c X_4^d X_5^e X_6^f] \quad (4.10)$$

where S is the symmetrization operator and a, b, c, d, e, f are indices such that $a + b + c + d + e + f = m$ and M is the order of polynomial. In the present work, the highest order

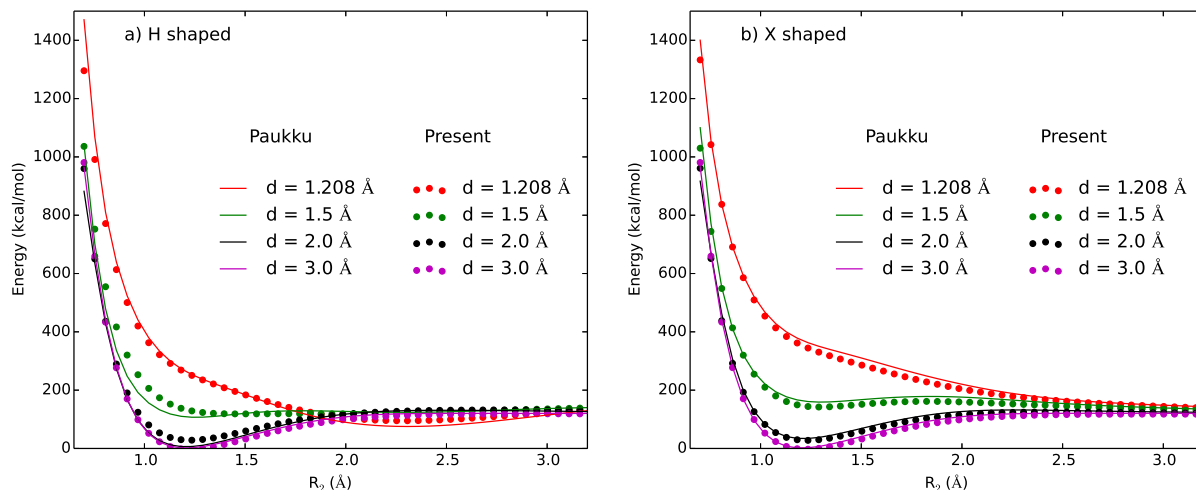


Figure 4.10: Comparison of the O_4 PES using the present point generation scheme with Paukku et al.[79] for a) H shaped O_4 atomic configuration for a fixed $R_1 = 1.098 \text{ \AA}$, $\theta = 90^\circ$, $\phi = 0^\circ$, $\psi = 90^\circ$ at different R_2 and d , b) X shaped O_4 atomic configuration for a fixed $R_1 = 1.098 \text{ \AA}$, $\theta = 90^\circ$, $\phi = 0^\circ$, $\psi = 0^\circ$ at different R_2 and d .

(M) is set to 9. The total number of coefficients for the O_4 global fit using the monomial symmetrization approach is 306. The quality of the fit is shown in Table 4.3. The mean unsigned error (MUE) and the root mean square errors (RMSE) for different intervals of the energies depict that the fit matches well with the CASPT2 calculations.

The comparison of the permutationally invariant global least square fit for the O_4 system reported in the present work with the global ground state PES reported by Paukku et al.[79] for H and X shaped molecular arrangements is shown in Figure 4.10. In the H shaped arrangement, the two pairs of atoms are placed parallel to each other in the same plane resembling the letter H. R_1 is fixed to equilibrium distance ($R_1 = 1.208 \text{ \AA}$). The values of the angular coordinates are fixed at $\theta = 90^\circ$, $\phi = 0^\circ$, $\psi = 90^\circ$. In contrast to the H shaped arrangement, the X shaped arrangement is such that two pairs of the atoms are perpendicular to each other and do not share any common plane. The values of the

Table 4.3: Mean unsigned error (MUE) and root mean square errors (RMSE) of the analytical fit with the CASPT2 PES for O_4 system.

(kcal/mol)	RMSE	MUE
$E < 240$	0.97	0.92
$240 < E < 500$	5.10	2.89
$500 < E < 1000$	10.56	7.98
$1000 < E < 2000$	12.87	9.91
$E > 2000$	14.72	10.27

angular coordinates are fixed at $\theta = 90^\circ$, $\phi = 0^\circ$, $\psi = 0^\circ$. It is evident from Figure 4.10 that there exists a reasonably good match between the two PESs.

In addition to the above arrangements, energies at the 5000 configurations constructed using the point generation scheme are calculated using the global fit reported by Paukku et al.[79] and compared with the corresponding energies calculated in the present work. The mean unsigned errors and the root mean square errors for different intervals are shown in Table 4.4. The statistical analysis carried out here is similar to the analysis for comparing the fit and PES discrete values (Table 4.3). The only point of difference is that in table 4.4, the energies for the new O_4 PES are compared with the global fit of the PES by Paukku et al. The values of the errors in Table 4.4 suggests that the new PES matches well with the PES reported by Paukku et al. at lower energies. However, at larger energies, there is a noticeable deviation. The global fit by Paukku et al. does not include points having energy greater than 2500 kcal/mol. The present PES has many configurations (~ 200) where the energies are greater than the value of this threshold. It is obvious that the energies at such points calculated using the global fit by Paukku et al. may not lead to correct answers. In addition to this, the comparison is not between the ab-initio energies calculated by the two works. Rather, the comparison is between the presently reported ab-initio energies with a global fit of ab-initio energies by Paukku et al. The inherent errors in fitting the data by Paukku et al. also adds to this discrepancy. In conclusion, it can be claimed that the overall match between the PESs is satisfactory for most of the topography. This vindicates the validity of the described point generation scheme.

Two dimensional contour plots for a six dimensional function requires limiting four coordinates. Polar contour plots in dimensions d and θ for O_2 - O_2 dimer configurations are shown in Figure 4.11. The interatomic distances R1 and R2 are fixed at equilibrium bond distance (1.208 Å). One of the two dimers is symmetrically placed on the x axis

Table 4.4: Mean unsigned error (MUE) and root mean square errors (RMSE) of the analytical fit with the analytical fit by Paukku et al.[83].

(kcal/mol)	RMSE	MUE
$E < 240$	3.13	1.87
$240 < E < 500$	4.17	2.91
$500 < E < 1000$	10.87	8.38
$1000 < E < 2000$	17.94	13.53
$E > 2000$	32.72	27.83

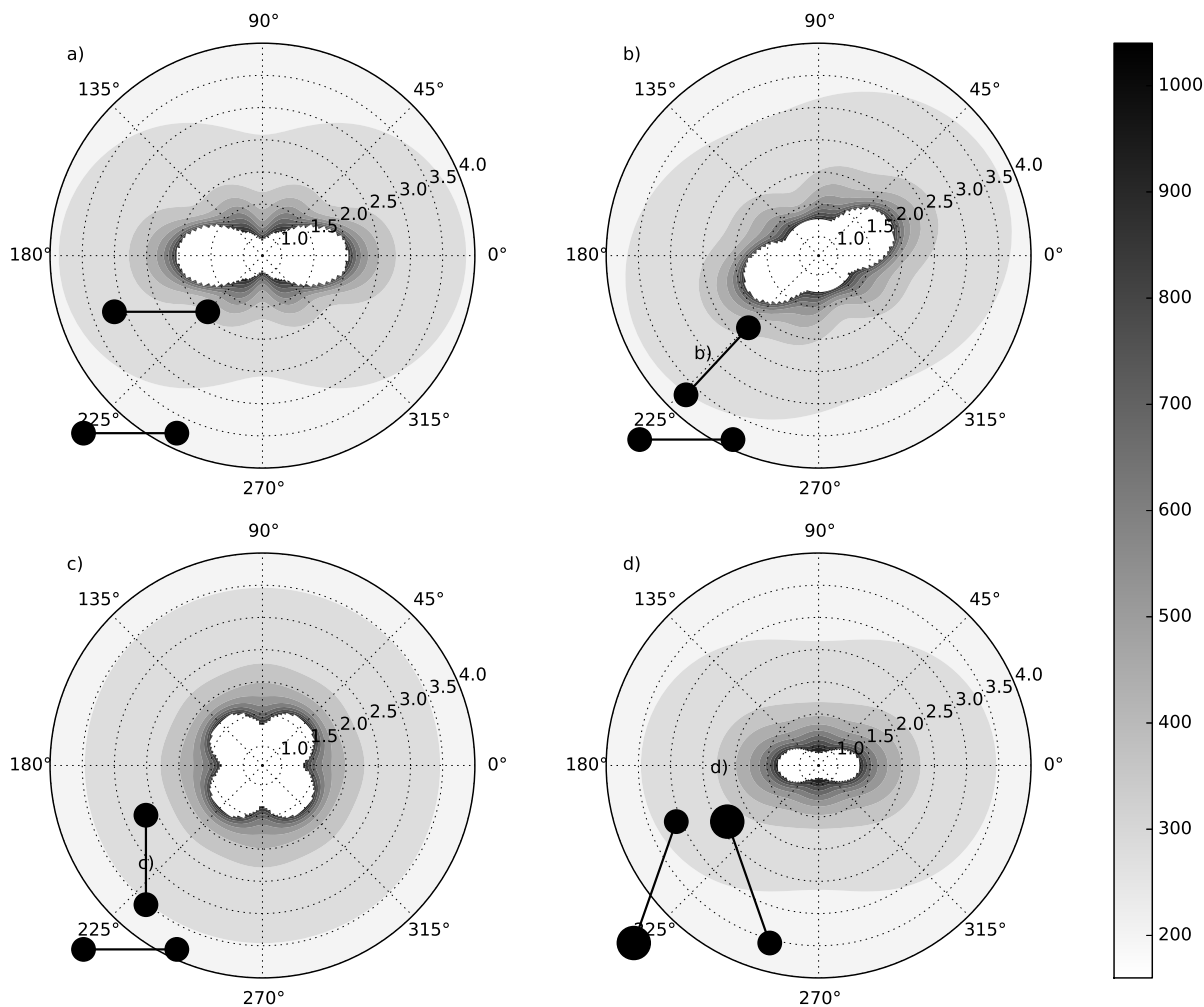


Figure 4.11: Contour plots for different geometric configurations. Sub figures a), b) and c) depict planar geometry and d) shows a non-planar geometry.

about the origin. The remaining two angular coordinates ϕ , ψ take the values $(\phi = 0^\circ, \psi = \pi/2)$, $(\phi = \pi/4, \psi = \pi/2)$, $(\phi = \pi/2, \psi = \pi/2)$ and $(\phi = 0^\circ, \psi = 0^\circ)$ for Figure 4.11 a, b, c and d respectively. Figures 4.11 a, b and c depict planar geometries and Figure 4.11 d characterizes a non-planar geometry.

The stationary points on the O_4 surface consist of the O_2 - O_2 dimer configuration, O_2+O+O configuration, C_{2v} points for the singlet ozone in O_3+O configuration and transition points for O_4 geometry. The equilibrium bond length for the oxygen molecule at O_2 - O_2 stationary point as calculated using the global PES is 1.2091 Å. The experimental data for the equilibrium bond length is 1.208 Å. It is apparent that adding extra points to the pool of configurations for the ab-initio calculations with both or either of bond length fixed at 1.208 Å results in the close match between the calculated value and the experimental data. In addition to the bond length, the predicted value (120.1 kcal/mol) of the bond dissociation of oxygen matches well with the corresponding experimental value (119.2 kcal/mol).

The characteristic points for the singlet O_3 system, the open minima, are also observed in O_3+O configuration. For the open minima or C_{2v} geometry, the values of the interatomic distance between O_1-O_2 , O_2-O_3 , and included angle $O_1-O_2-O_3$ are 1.22 Å, 1.28 Å and 117° respectively. [85].

The O_4 system is known to exist in two main isomers: cyclic and star-like isomer. The transition point in the cyclic isomer form is a planar square geometry with its side (R_c) equal to 1.484 Å. Also the isomer is at energy (ΔE) equal to 110.7 kcal/mol above the $O_2 + O_2$ configuration. These values are in excellent agreement with the corresponding values ($R_c = 1.482$ Å and $\Delta E = 112.2$ kcal/mol) reported by Paukku et al.[79]. The star like isomer can be described as a configuration with one Oxygen atom at the centroid of an O_3 complex forming an equilateral triangle. At the transition point, the length joining the centroid atom and any of the atoms of the triangle (R_s) is found to be 1.34 Å. Again this value also matches reasonably with the reported value ($R_s = 1.29$ Å). The variation of energy with the values of R_c of the cyclic geometry is shown in Figure 4.12.

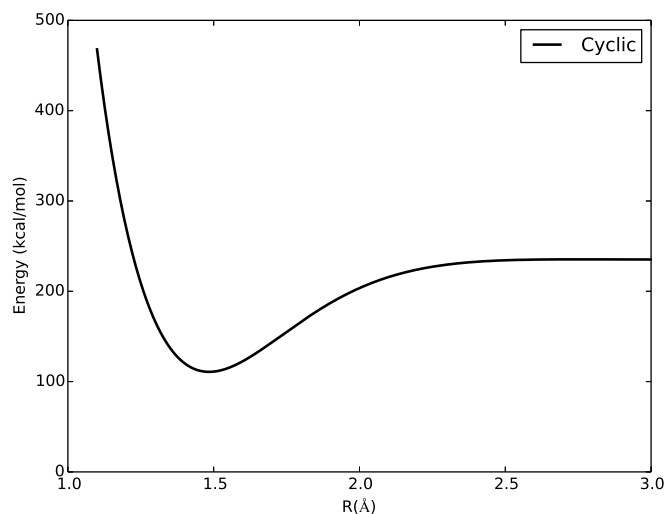


Figure 4.12: Variation of energy (kcal/mol) with R_c for cyclic geometry where R_c denotes the side of the square.

The non-planar cyclic O_4 molecule dissociates to two O_2 molecules through a C_2 transition point. The minimum energy path has been a focus of many studies[100, 101, 102, 103]. The dissociation energy or the heat of formation as well as the barrier height have been reported using different computational chemistry algorithms such as Coupled cluster methods (CISD, CCSD, CCSD(T)), and Multireference Fixed Node diffusion Quantum Monte Carlo (MR-FM-DMC) method. The geometry of the D_{2d} and C_2 stationary point and respective energy along the minimum energy path for the reaction $O_4 \rightarrow 2O_2$ is depicted

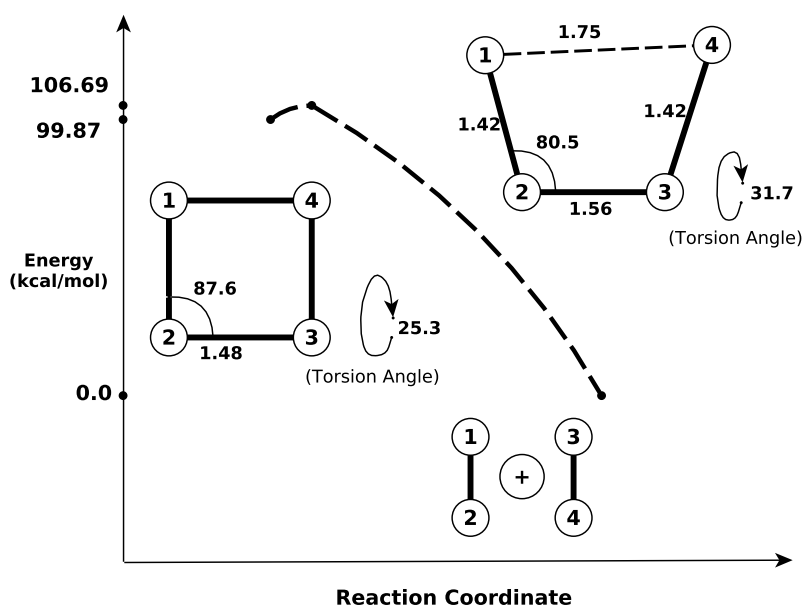


Figure 4.13: Minimum energy path for reaction $O_4 \rightarrow 2O_2$. All distances and angles have dimensions of \AA and deg° respectively. Energy is with respect to O_2+O_2 .

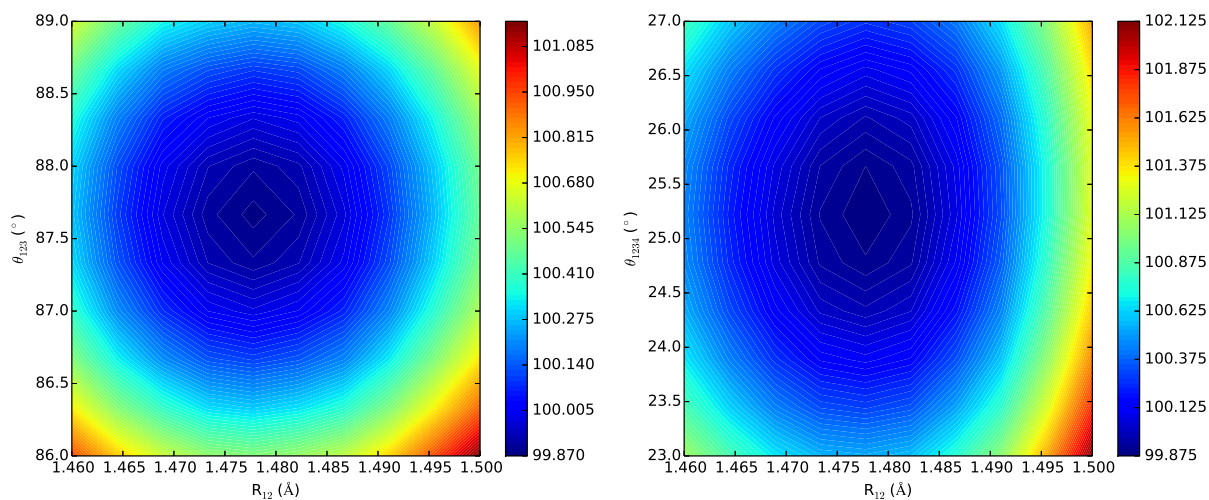


Figure 4.14: 2D contour plot in the neighbourhood of the D_{2d} stationary point as a function of a) R_{12} and θ_{123} with $\theta_{1234}=25.2^\circ$ and b) R_{12} and θ_{1234} with $\theta_{123}=87.3^\circ$. Energy is with respect to O_2+O_2 .

in Figure 4.13. The geometry of the D_{2d} stationary point is described using interatomic distance between adjacent atoms R_{12} ($=R_{23}=R_{34}=R_{14}$), included angle θ_{123} and dihedral angle θ_{1234} . The neighbourhood of the D_{2d} point is shown as two dimensional contour plots in Figure 4.14 by fixing one of the three coordinates. The geometry of the transition point and the stable tetraoxygen are close to the values reported in the literature[104, 101]. Further, comparison of the values of heat of formation and barrier height, tabulated in Table 4.5, shows that the present surface is within the acceptable limits of accuracy.

Table 4.5: Heat of formation and barrier height ($O_4 \rightarrow 2O_2$).

	Heat of formation $E(O_4)-E(2O_2)$ (kcal/mol)	Barrier Height $E(TS)-E(O_4)$ (kcal/mol)
Present	99.87	6.82
CCSD(T)[101]	93.2	7.9
MR-FN-DMC[102]	98.5 ± 1.9	11.4 ± 1.6

4.4 N_4 PES

In addition to the O_4 singlet spin state PES, the point generation scheme was used to construct a PES for the N_4 system. The comparison of the new PES with the existing PES by Paukku et al.[83] serves as an additional proof for the point generation scheme. For the N_4 system, again Multireference second order perturbation theory (CASPT2) is used to account for dynamical corrections following the Complete Active Space Multiconfiguration SCF (CASSCF) method. The choice of active space is critical[25] for CASSCF. An active space of 12 electrons comprising of only 2p orbitals of the four nitrogen atoms and 12 orbitals is used. Paukku et al.[83] have also used the same active space for the global N_4 system. Augmented correlation-consistent polarized valence triple zeta basis set (aug-cc-PVTZ) is chosen for calculations. The total computational time for the 5000 points running in parallel on Intel Xeon workstation was 12960 CPU hours.

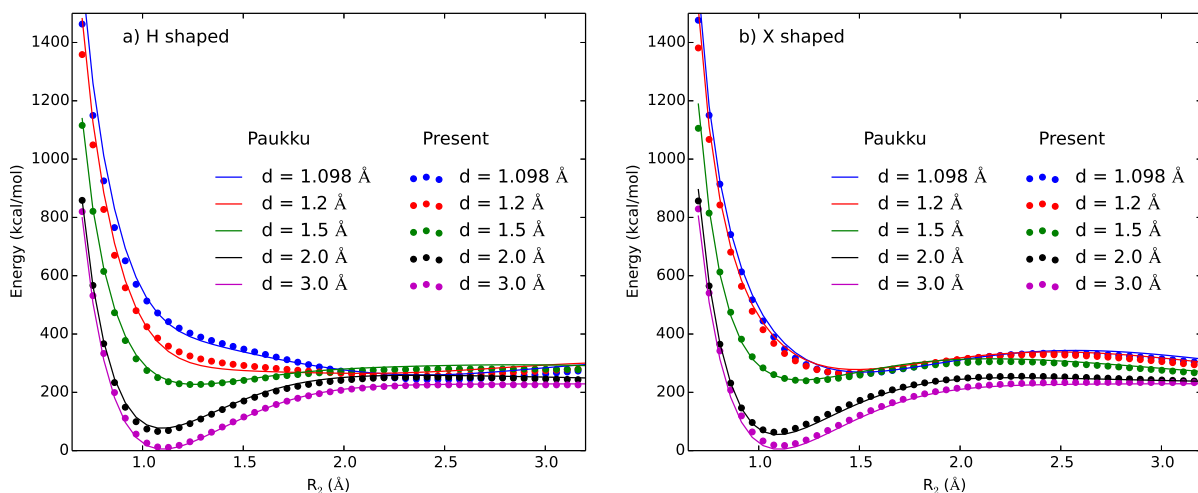


Figure 4.15: Comparison of the N_4 PES using random point generation scheme with Paukku et al.[83] for a) H shaped N_4 atomic configuration for a fixed $R_1 = 1.098$ Å, $\theta = 90^\circ$, $\phi = 0^\circ$, $\psi = 90^\circ$ at different R_2 and d b) a) X shaped N_4 atomic configuration for a fixed $R_1 = 1.098$ Å, $\theta = 90^\circ$, $\phi = 0^\circ$, $\psi = 0^\circ$ at different R_2 and d .

The comparison of the permutationally invariant global least square fit for the N_4 system reported in the present work with the global ground state PES reported by Paukku et al.[83] for H and X shaped molecular arrangements is shown in Figure 4.15. In H shaped arrangement, the two pairs of atoms are placed parallel to each other in the same plane resembling the letter H. R1 is fixed to equilibrium distance ($R1 = 1.098 \text{ \AA}$). The values of the angular coordinates are fixed at $\theta = 90^\circ$, $\phi = 0^\circ$, $\psi = 90^\circ$. In contrast to H shaped arrangement, the pair of the atoms are perpendicular to each other and do not share any common plane in the X shaped arrangement. The values of the angular coordinates are fixed at $\theta = 90^\circ$, $\phi = 0^\circ$, $\psi = 0^\circ$. It is evident from Figure 4.15 that there exists a reasonably good match between the two PESs. In conclusion, the new N_4 PES along with the O_4 PES serves a good validation for the new point generation scheme.

4.5 Summary

The new PESs generated for O_4 , O_3 , N_3 and N_4 systems are the major contributions from this effort and along with existing PESs for N_4 , N_2O_2 , N_2O , NO_2 represent the best available PESs at present. These PESs are employed in the QCT code to calculate the reactive cross-section databases.

Chapter 5

Cross-section Database

This chapter presents the cross-section databases that are generated using the Quasi-classical Trajectory (QCT) method employing the best available PESs. N_3 [85] and N_4 [83] PESs are used to calculate dissociation cross-sections [85, 105] of a Nitrogen molecule colliding with a Nitrogen atom and another Nitrogen molecule respectively. O_3 [85] and O_4 [87, 79, 88] PESs are employed to generate the cross-section database for Oxygen dissociation. NO_2 [67] and N_2O [74] surfaces are employed to calculate the exchange cross-section for Zeldovich reactions. N_2O_2 [84] PES is used to generate the cross-section database for high energy N_2 - O_2 collisions.

In contrast to Nitrogen systems, the differences in the energies between the low lying electronic states and the ground state for Oxygen systems are small. Further, these surfaces may intersect with each other at several places. In such cases, the collision may progress on either of the surfaces. For instance, the singlet[87, 79], triplet [88] and quintet[79] spin state O_4 PESs are close to each other. Statistically, 5/9 collisions occur on the quintet surface, 1/9 on the singlet, and 1/3 on the triplet surface. In the present work, the CID cross sections for O_2 - O_2 collisions are calculated on the singlet surface using the PES developed by us, while the cross sections on the triplet and quintet spin state are calculated using the PES by Paukku et al[79, 88]. It is assumed that a collision starting on one surface remains on the same surface during the entire time of interaction. This assumption is also known as the adiabatic assumption. The cross-sections are calculated for all three surfaces separately and an effective dissociation cross-section is calculated. Similarly, cross-section calculations for the exchange reactions involving NO_2 and N_2O systems are carried on two surfaces each: $^2A'$ and $^4A'$ for N_2O , and $^3A'$ and $^3A''$ for NO_2 respectively.

In the next section, a detailed explanation of a new cross-section fitting scheme is presented along with its significance and validation. This is followed with a discussion on

the results of the QCT simulations and analysis of the cross-section databases. Finally, the accuracy of the work is validated by comparing the reaction rate coefficients calculated by integrating the reactive cross-section databases with Maxwell-Boltzmann distribution against the available experimental reaction rate coefficients at equilibrium conditions. In addition to the equilibrium conditions, the cross-section databases are expected to work well in non-equilibrium cases too.

5.1 Cross-section fitting scheme

5.1.1 Selection of ro-vibrational level

Reactive cross-section is a function of ro-vibrational levels and relative translational energy. The major problem in generating the cross-section database is its data intensiveness. As calculated using the WKB method, it is established that the numbers of ro-vibrational levels of Nitrogen and Oxygen molecule are 9019 and 6094 respectively. In the reaction involving $\text{N}_2\text{-N}_2$ and $\text{O}_2\text{-O}_2$ collisions, ensembles at $^{9019}C_2$ and $^{6094}C_2$ different ro-vibrational combinations respectively have to be generated for a complete database. It is obvious that running ensembles at each ro-vibrational combinations is not practicable. Alternatively, cross-sections are calculated using ensembles built at equispaced ro-vibrational combinations and at remaining levels, interpolation or data fitting is employed.

To reduce the numerical load, the following fitting scheme has been devised in the present work. At the core of the technique is the conjecture that at a given vibrational level, the variation of the reactive cross-section (σ_r) with the relative translational energy (E_{tr}) at different rotational levels have a similar form. As the rotational number increases, it is observed that the difference between the reactive cross-section ($\sigma_r(j+1) - \sigma_r(j)$) for a fixed relative translational energy increases. The difference in the energy between two successive rotational levels also varies in a similar pattern. The proposed technique utilizes this observation and uses spectroscopic data for data fitting.

The first step is the selection of appropriate ro-vibrational levels for which the ensembles are generated. In the case of atom-molecule reactions, ensembles are run at zeroth and half the maximum rotational level for each vibrational level. For instance, ensembles are generated for the atom-molecule reactions involving the Nitrogen molecule at $v = \{0, 1, \dots, 55\}$ and $j = 0$. In addition to the results at the zeroth rotational number, another batch of ensembles is run at half the maximum possible rotational number ($j = j(v)_{max}/2$). The procedure remains the same with an added complexity due to non-zero rotational quantum number. A similar process is carried out for the atom-molecule reactions involving O_2 and NO molecules. The only difference is the number of vibrational

levels and the value of $j(v)_{max}/2$.

In contrast to the atom-molecule reactions, molecule-molecule reactions employ a higher number of ensembles. For cases involving the collision of the same molecular species (N_2 - N_2 and O_2 - O_2), the ensembles are generated for different values of relative translational energies for the following combinations of ro-vibrational levels:

- $v_1 = v_2 = 0, 1, \dots, v_{max}, j_1 = j_2 = 0$,
- $v_1 = v_2 = 0, 1, \dots, v_{max}, j_1 = j_{max}(v_1)/2, j_2 = 0$, and
- $v_1 = v_2 = 0, 1, \dots, v_{max}, j_1 = j_2 = j_{max}(v_2)/2$

For molecule-molecule collision involving molecules of different species (N_2 - O_2), v_{max} and $j_{max}(v)$ are different for the two molecules. An additional set of ro-vibrational combinations is required for this asymmetry (point 3 in the following list). The set of combinations for such a heterogeneous system consists of:

- $v_{N_2} = v_{O_2} = 0, 1, \dots, v_{N_2,max}, j_{N_2} = j_{O_2} = 0$,
- $v_{N_2} = v_{O_2} = 0, 1, \dots, v_{N_2,max}, j_{N_2} = j_{max}(v_{N_2})/2, j_{O_2} = 0$, and
- $v_{N_2} = v_{O_2} = 0, 1, \dots, v_{N_2,max}, j_{N_2} = 0, j_{O_2} = j_{max}(v_{O_2})/2$, and
- $v_{N_2} = v_{O_2} = 0, 1, \dots, v_{N_2,max}, j_{N_2} = j_{max}(v_{N_2})/2, j_{O_2} = j_{max}(v_{O_2})/2$

For all combinations with $v_{N_2} > v_{O_2,max}$, $v_{O_2} = v_{O_2,max}$.

5.1.2 Fitting scheme formulation

The reactive cross-section for all cases at the selected ro-vibrational numbers are calculated using Equation 3.7 and 3.8 for atom-molecule and molecule-molecule reaction respectively. The second step of the scheme is to fit the reactive cross-section for all remaining ro-vibrational levels or combinations of the same. The general formula of the fit for the atom-molecule reaction is assumed to be:

$$\sigma_R(v, j, V_R) = ((w_1\sigma_R(v, 0, V_R)^{0.5} + w_2\sigma_R(v, j(v)_{max}/2)^{0.5}, V_R)/(w_1 + w_2))^2 \quad (5.1)$$

where w_1 and w_2 are the weights

$$w_1 = \tilde{\nu}(v, j(v)_{max}/2) - \tilde{\nu}(v, j) \quad (5.2)$$

$$w_2 = \tilde{\nu}(v, j) - \tilde{\nu}(v, 0) \quad (5.3)$$

and $\tilde{\nu}(v, j)$ is the internal energy:

$$\tilde{\nu}(v, j) = \omega_e(v+0.5) - \omega_e x_e(v+0.5)^2 + \omega_e y_e(v+0.5)^3 + (B_e - \alpha_e(v+0.5))j(j+1) - D_e j^2(j+1)^2 \quad (5.4)$$

where $\omega_e, \omega_e x_e, \omega_e y_e$ are vibrational constants and B_e, α_e and D_e are rotational constants.

As an extension to the previous formula, a weighted 2D bilinear interpolation is used for molecule-molecule reaction (N_2-N_2 and O_2-O_2). The first step involves interpolating data for all combinations of rotational numbers for a given vibrational number with the form:

$$\begin{aligned} \sigma(v_1, v_2, j_1, j_2, V_R) = & ((w_{00}\sigma(v_1, v_2, 0, 0, V_R))^{0.5} + \\ & (w_{01}\sigma(v_1, v_2, j_{max}/2, 0, V_R))^{0.5} + \\ & (w_{11}\sigma(v_1, v_2, j_{max}/2, j_{max}/2, V_R))^{0.5} \\ & / (w_{00} + w_{01} + w_{11})^2 \end{aligned} \quad (5.5)$$

The weights w_{00}, w_{01} and w_{11} are defined as:

$$w_{00} = (e_J(j_{max}/2) - e_J(j_1))(e_J(j_{max}/2) - e_J(j_2)) \quad (5.6)$$

$$\begin{aligned} w_{01} = & (e_J(j_{max}/2) - e_J(j_1))(e_J(j_2) - e_J(0)) + \\ & (e_J(j_{max}/2) - e_J(j_2))(e_J(j_1) - e_J(0)) \end{aligned} \quad (5.7)$$

$$w_{11} = (e_J(j_1) - e_J(0))(e_J(j_2) - e_J(0)) \quad (5.8)$$

where $j_{max}/2$ is half the maximum rotational number for a vibrational number and e_J is the rotational energy calculated using spectroscopic data.

In the case N_2-O_2 collision, a slight modification is made to account for asymmetry of the ro-vibrational levels.

$$\begin{aligned} \sigma(v_{N_2}, v_{O_2}, j_{N_2}, j_{O_2}) = & ((w_{00}\sigma(v_{N_2}, v_{O_2}, 0, 0))^{0.5} + \\ & (w_{01}\sigma(v_{N_2}, v_{O_2}, j_{max, N_2}/2, 0))^{0.5} + \\ & (w_{10}\sigma(v_{N_2}, v_{O_2}, 0, j_{max, O_2}/2))^{0.5} + \\ & (w_{11}\sigma(v_{N_2}, v_{O_2}, j_{max, N_2}/2, j_{max, O_2}/2))^{0.5} \\ & / (w_{00} + w_{01} + w_{10} + w_{11})^2 \end{aligned} \quad (5.9)$$

The weights w_{00} , w_{01} , w_{10} and w_{11} are defined as:

$$w_{00} = (e_J(j_{max}/2) - e_J(j_{N_2}))(e_J(j_{max}/2) - e_J(j_{O_2})) \quad (5.10)$$

$$w_{01} = (e_J(j_{max}/2) - e_J(j_{N_2}))(e_J(j_{O_2}) - e_J(0)) \quad (5.11)$$

$$w_{10} = (e_J(j_{max}/2) - e_J(j_{O_2}))(e_J(j_{N_2}) - e_J(0)) \quad (5.12)$$

$$w_{11} = (e_J(j_{N_2}) - e_J(0))(e_J(j_{O_2}) - e_J(0)) \quad (5.13)$$

The second step is to fit the data for the remaining combinations of vibrational numbers. CID cross-sections for a combination of vibrational numbers (v_1, v_2) are assumed to be a weighted average of the data calculated at combinations (v_1, v_1) and (v_2, v_2) .

The vibrational and rotational constants are obtained from data fitting energy levels calculated using the WKB method and Numerov's method. The values along with the corresponding experimental values[106] are tabulated and compared in Table 5.1. Again the comparison shows reasonable match[106].

Table 5.1: Spectroscopy constants(cm^{-1})

	N ₂ [106]	N ₂ (WKB)	N ₂ (Numerov)	O ₂ [106]	O ₂ (WKB)	O ₂ (Numerov)
ω	2358.57	2382.23	2315.24	1580.39	1620.93	1606.69
$\omega_e x_e$	14.324	14.57	14.01	12.112	12.74	11.79
$\omega_e y_e$	-0.00226	-0.00228	-0.00262	0.0754	0.02812	0.091
B_e	1.99824	2.006	1.999	1.4451	1.4147	1.3291
α_e	0.017318	0.01775	0.01781	0.01523	0.01504	0.01612
D_e	5.76e-6	6.459e-6	5.971e-6	4.839e-6	3.734e-6	4.07e-6

5.1.3 Validation of the scheme

The validation of the new weighted scheme is established in the following paragraphs. Consider the atom-molecule reaction $\text{N}_2 + \text{N} \rightarrow 3\text{N}$. Reactive cross-sections at $j = 0$ and $j = j(v)_{max}/2$ are calculated using the QCT method. The remaining ro-vibrational levels are calculated using the weighted fitting scheme. An extra set of ensembles are run at a different rotational energy level between 0 and maximum rotational number for a N_2 -N reaction at a vibrational level of the nitrogen molecule at 20. The comparison of the generated data with the interpolated data for rotational number $j=30$ is shown in

Figure 5.1. The close agreement is the validation of the method. The average relative differences between interpolated values and values obtained using the QCT method for different rotational numbers and different relative translational energies were less compared to the average relative difference for simple interpolation without any weights (i.e. $w_1 = w_2 = 1$). This highlights that the reactive cross-section for different rotational levels at a given vibrational level does not follow a linear fitting scheme and a weighted scheme is more reasonable.

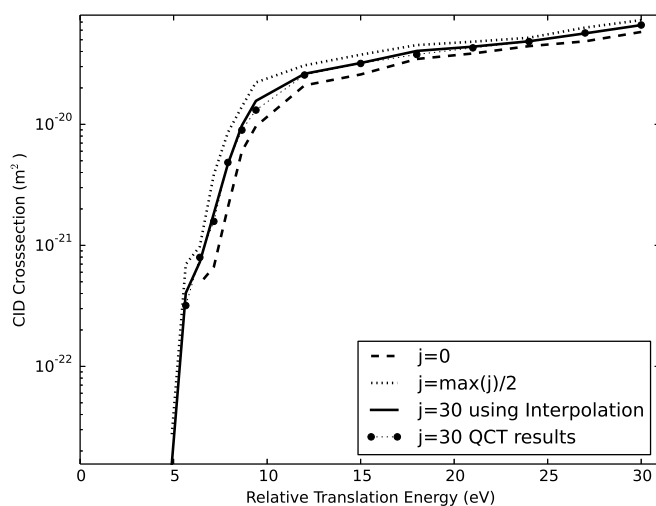


Figure 5.1: Comparison of QCT results at $j=30$ with interpolated values using the data at $j=0$ and $j=\max(j)/2$ for $N_2+N \rightarrow 3N$ reaction. The vibrational number for all the line plots correspond to 20.

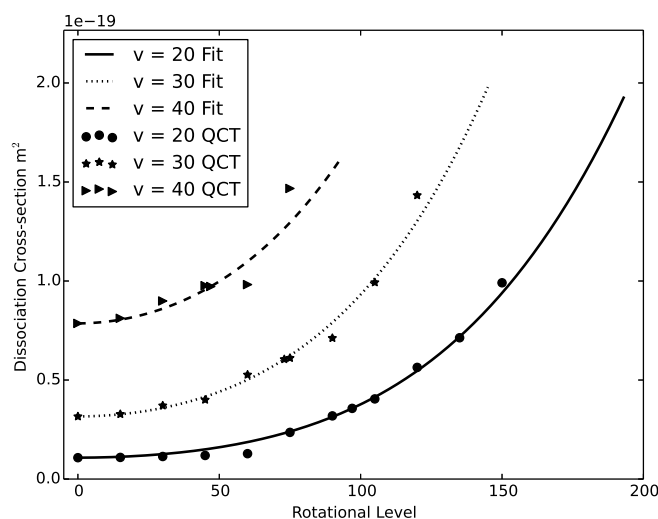


Figure 5.2: Comparison of QCT results (represented by scatter plot) with fitted values (line plot) using the data at $j=0$ and $j=\max(j)/2$ for the $N_2+N \rightarrow 3N$ reaction at $E_{trans} = 9.4$ eV and for different rotational and vibrational numbers.

Further, for the same reaction, Figure 5.2 shows the comparison between the reac-

tive cross-section generated using trajectories at different rotational levels at a constant relative translational energy ($E_{trans} = 9.4$ eV) and the reactive cross-section generated using the fit described by Equations 5.1-5.4 for all rotational levels for different vibrational numbers ($v=20,30,40$). It is evident that the reactive cross-section calculated using the fit is in good agreement with the reactive cross-section calculated using trajectories.

Consider the $N_2+N_2 \rightarrow N_2+2N$ reaction. Extra sets of ensembles are run at random combination of ro-vibrational energy levels. Reactive cross-section generated (tabulated in Table 5.2) using the QCT method for random combinations of rotational and vibrational numbers of the two molecules match well with the reactive cross-section as calculated using the fitting scheme.

Table 5.2: Comparison of reactive cross-section generated by the QCT method and using the weight based fitting scheme for random sets of ro-vibrational combination at 16000 m/s relative velocity for the reaction $N_2 + N_2 \rightarrow N_2 + 2N$.

v_1	v_2	j_1	j_2	σ_{QCT} (m ²)	σ_{fit} (m ²)
18	20	195	149	3.31156739229e-19	3.42988514801e-19
9	18	107	98	3.69115863634e-21	3.9646279757e-21
18	25	51	65	8.03822235687e-20	9.19512995319e-20
16	32	130	94	3.87426381778e-19	3.96747016981e-19
10	12	108	108	2.90252708457e-21	2.82702396128e-21
7	33	83	101	1.41732314562e-19	1.42560208477e-19
6	8	81	31	6.63373879593e-20	6.38885388347e-20
11	5	171	145	6.13707827777e-20	6.29826505234e-20
5	12	56	45	8.10520882674e-20	9.44146784209e-20
40	19	64	46	4.66358255125e-20	4.81932538555e-20

5.2 Results and Discussion

As explained in the preceding paragraphs, different ensembles are chosen and simulated for the reactions as mentioned in Table 2.2. As mentioned in the introduction of this chapter, in the case of O_2-O_2 collision, the database is generated on three PESs: singlet, triplet and quintet spin state surfaces. Similarly, in the case of N_2-O and O_2-N collisions, the two lowest PESs ($^3A'$ and $^3A''$ for N_2O , $^2A'$ and $^4A'$ for NO_2 respectively) are used for generating two databases of cross-section. Figures 5.3-5.6 show the variation of reaction cross-section with relative translational energy for different reactions pertaining to air

chemistry for different values of ro-vibrational levels.

The reactive cross-section generally increases with increase in relative translational energy. However, there are caveats associated with this statement. Firstly, for dissociation processes, the collision induced dissociation (CID) cross-section peaks at a certain value of relative translational energy and starts to decrease with further increase. This is because the high relative velocity during such a collision reduces the interaction time needed for the process of bond breaking and formation and consequently reduces the probability of the collision leading to a reaction. Secondly, in the case of Zeldovich reactions, the process of exchange and dissociation compete with each other. This can be observed from Figures 5.5 and 5.6. The collision induced exchange (CIE) cross-section has a lower threshold value. This is because the exchange reactions have a lower activation energy. Hence, the exchange cross-section peaks at a lower value of relative translational energy than the corresponding dissociation cross-section. As the energy in the collision increases, the chances of the molecule dissociating into atoms increases and this leads to competition between the processes of exchange and dissociation. This in turn results in a decrease in the exchange cross-section at higher relative translational energy.

The reactive cross-section increases with increase in the internal energy in a collision. The plot of cross-section vs relative translational energy shifts to a higher value with increase in rotational and vibrational energy. In addition to this, the threshold value or the lowest value of the relative translational energy with non-zero reactive cross-section decreases with the increase in the rotational and vibrational levels. This is due to increase in the contribution of internal energy which effectively reduces the activation energy provided by the translational energy mode.

Figure 5.5 a)-d) shows that the collision induced exchange (CIE) cross-section for $\text{N} + \text{O}_2 \rightarrow \text{NO} + \text{O}$ at different ro-vibrational levels on the two different PESs ($^2A'$ and $^4A'$). It is observed that at lower relative translational energy, the trajectories favour the lower energy $^2A'$ PES compared to the $^4A'$ surface. This leads to a higher value of exchange cross-section at lower energy. As the energy of the system increases, the trajectories favour the $^4A'$ surface. In comparison with this, no such clear statement can be made for the exchange cross-section for reaction $\text{O} + \text{N}_2 \rightarrow \text{NO} + \text{N}$ on the two $^3A'$ and $^3A''$ surfaces (Figure 5.6 a-d).

The accuracy of the ab-initio based chemical model depends on the accuracy of the fitting function chosen to interpolate the dissociation (CID) and exchange (CIE) cross-section as a function of relative translational energy. After manipulating different forms using trial and error, the following function was found to be the most suitable for fitting

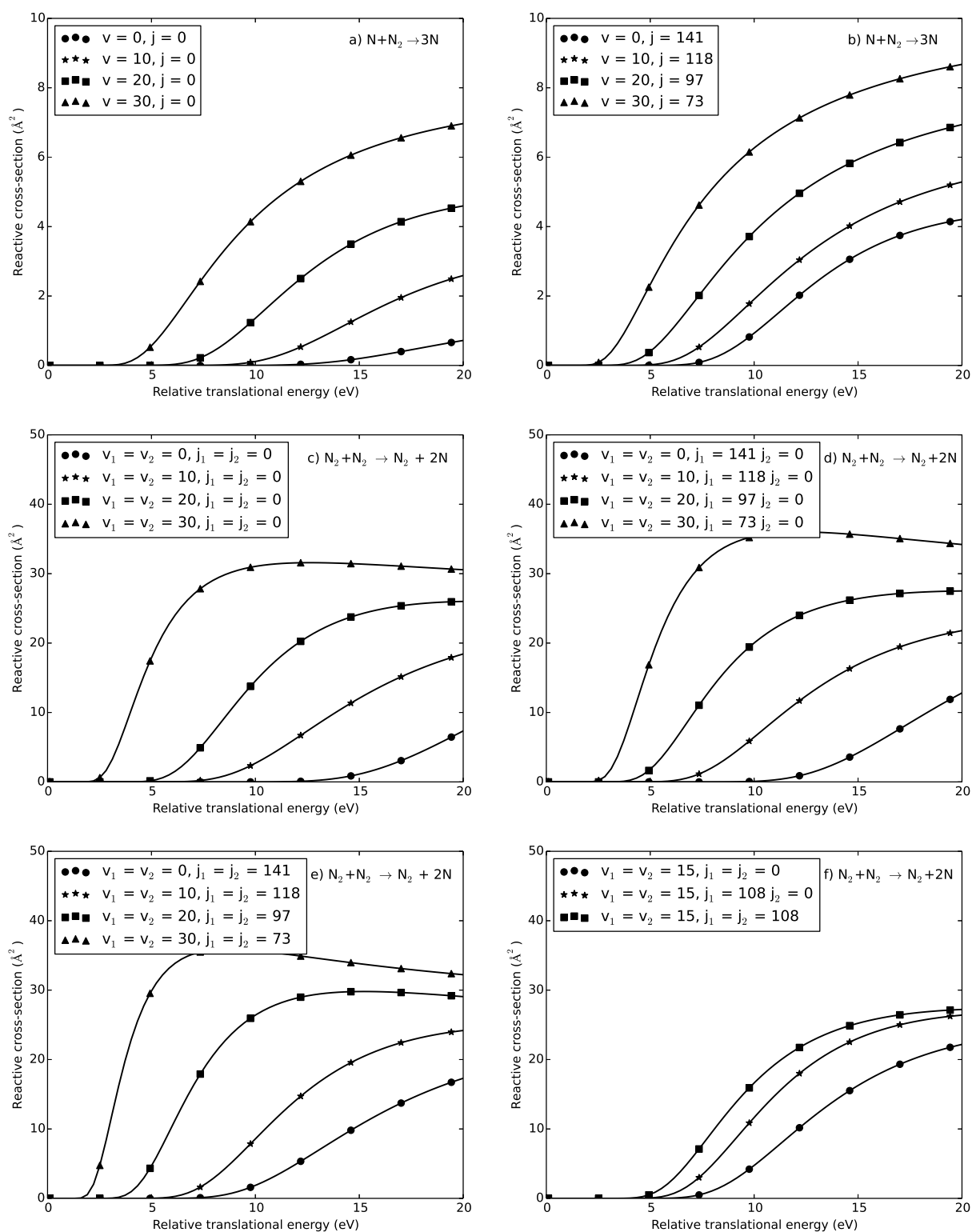


Figure 5.3: Dissociation cross-section vs. Relative translational energy at different ro-vibrational levels for a)-b) $\text{N}_2 + \text{N} \rightarrow 3\text{N}$ and c)-f) $\text{N}_2 + \text{N}_2 \rightarrow \text{N}_2 + 2\text{N}$.

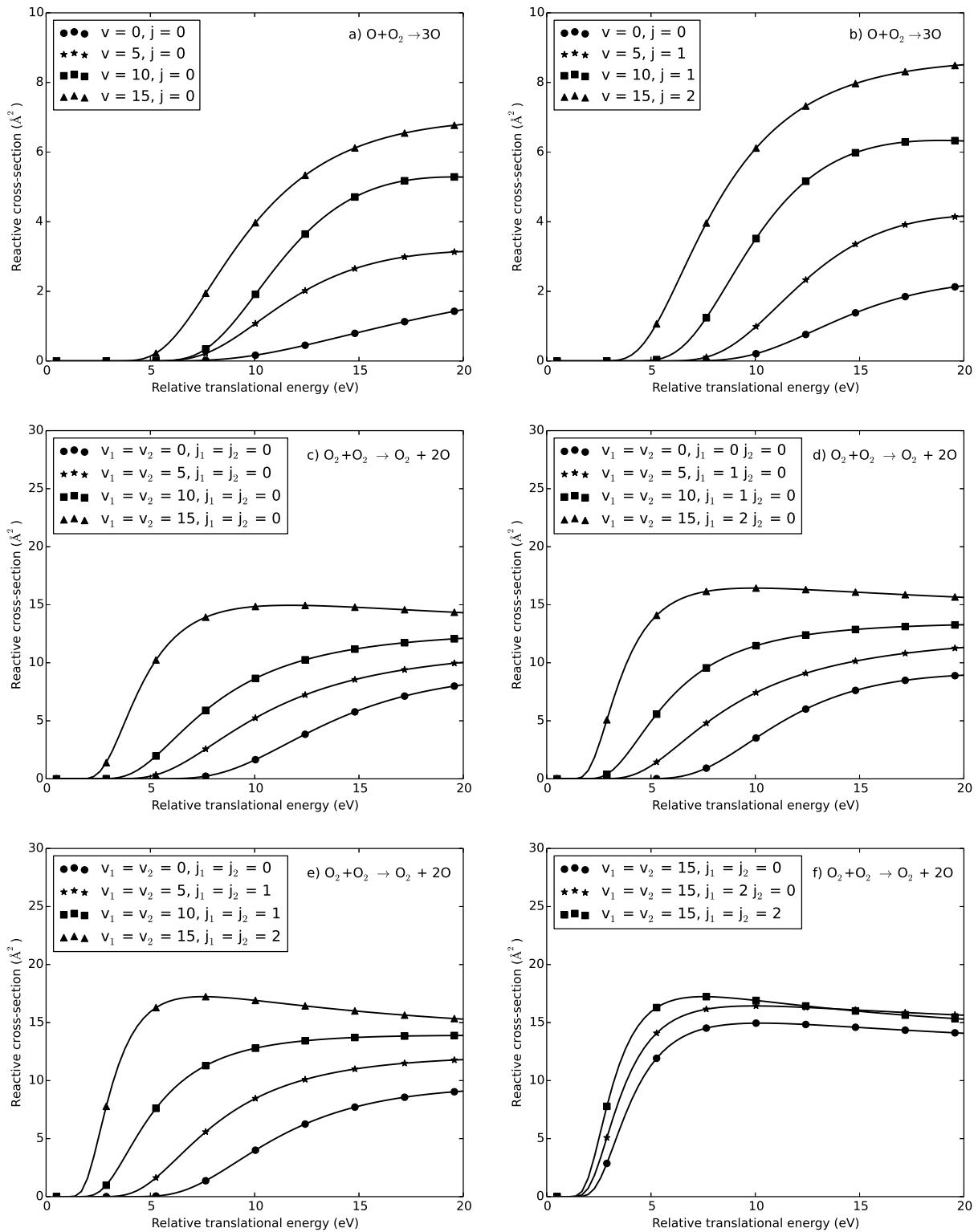


Figure 5.4: Dissociation cross-section vs. Relative translational energy at different ro-vibrational levels for a)-b) $\text{O}_2 + \text{O} \rightarrow 3\text{O}$ and c)-f) $\text{O}_2 + \text{O}_2 \rightarrow \text{O}_2 + 2\text{O}$.

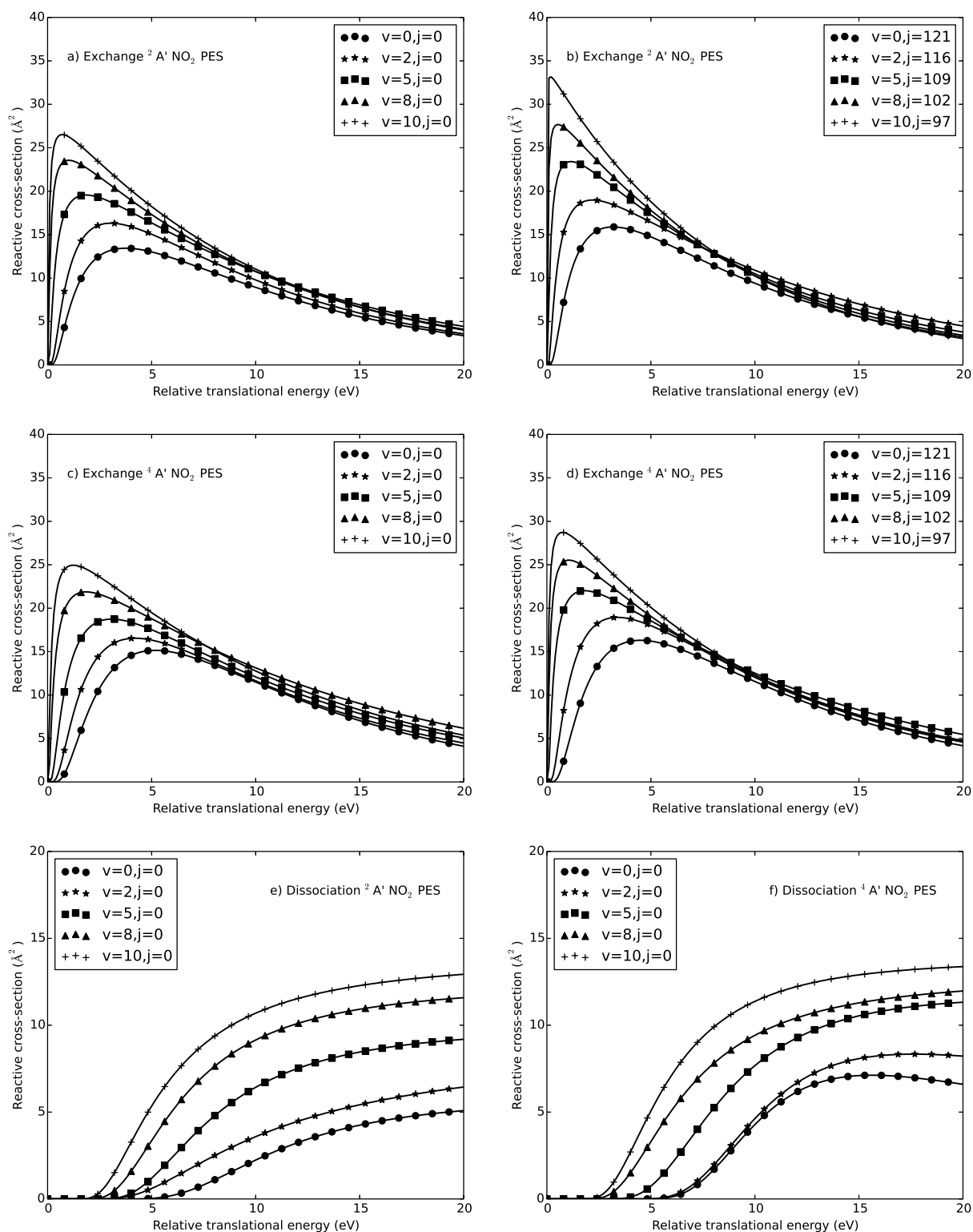


Figure 5.5: Exchange cross-section vs. Relative translational energy at different rovibrational levels for a)-d) $\text{O}_2 + \text{N} \rightarrow \text{NO} + \text{O}$ on two surfaces. Dissociation cross-section for reactions e)-f) $\text{O}_2 + \text{N} \rightarrow 2\text{O} + \text{N}$ on the two surfaces.

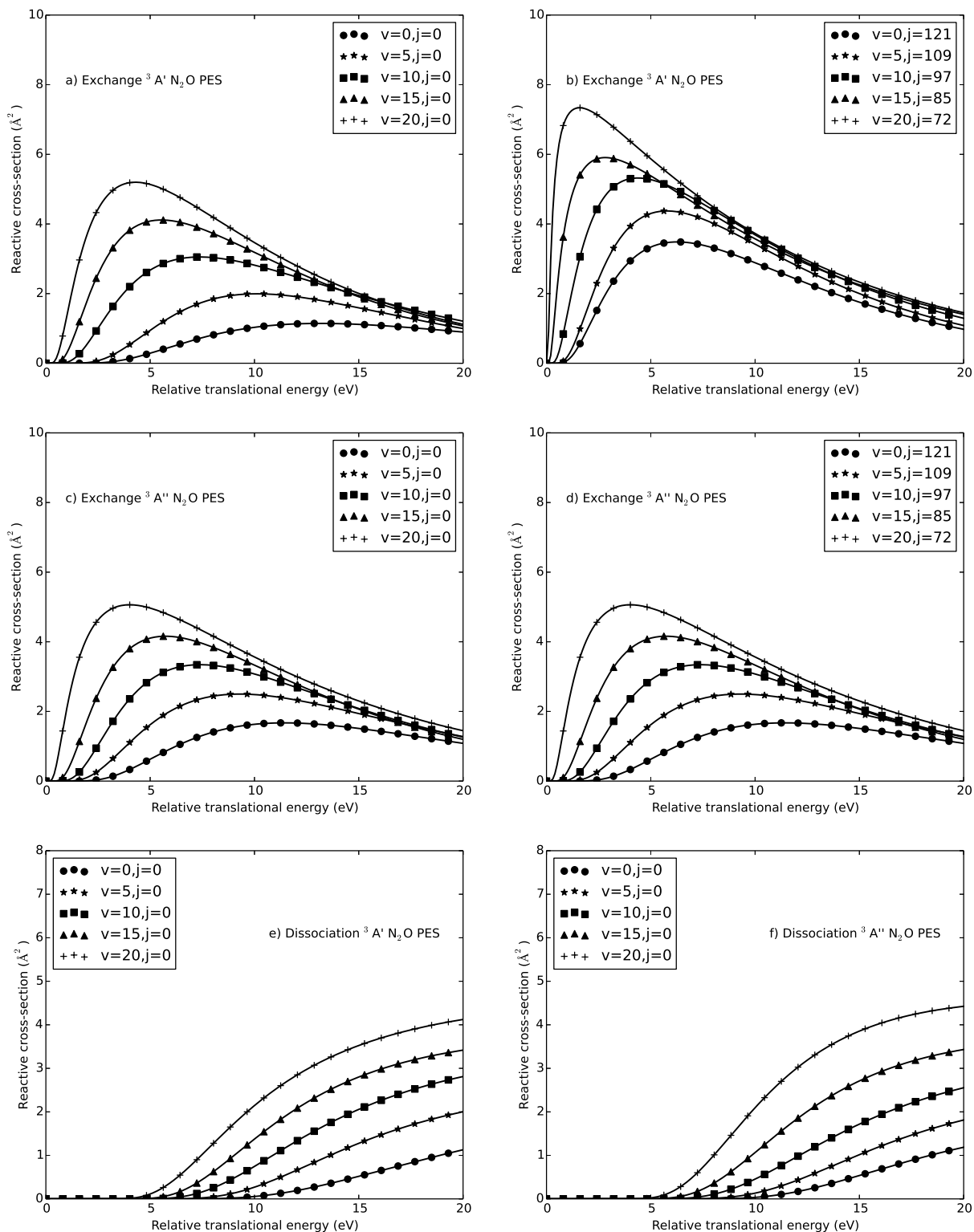


Figure 5.6: Exchange cross-section vs. Relative translational energy at different ro-vibrational levels for a)-d) $N_2 + O \rightarrow NO + N$ on two surfaces. Dissociation cross-section for reactions e)-f) $N_2 + O \rightarrow 2N + O$ on the two surfaces.

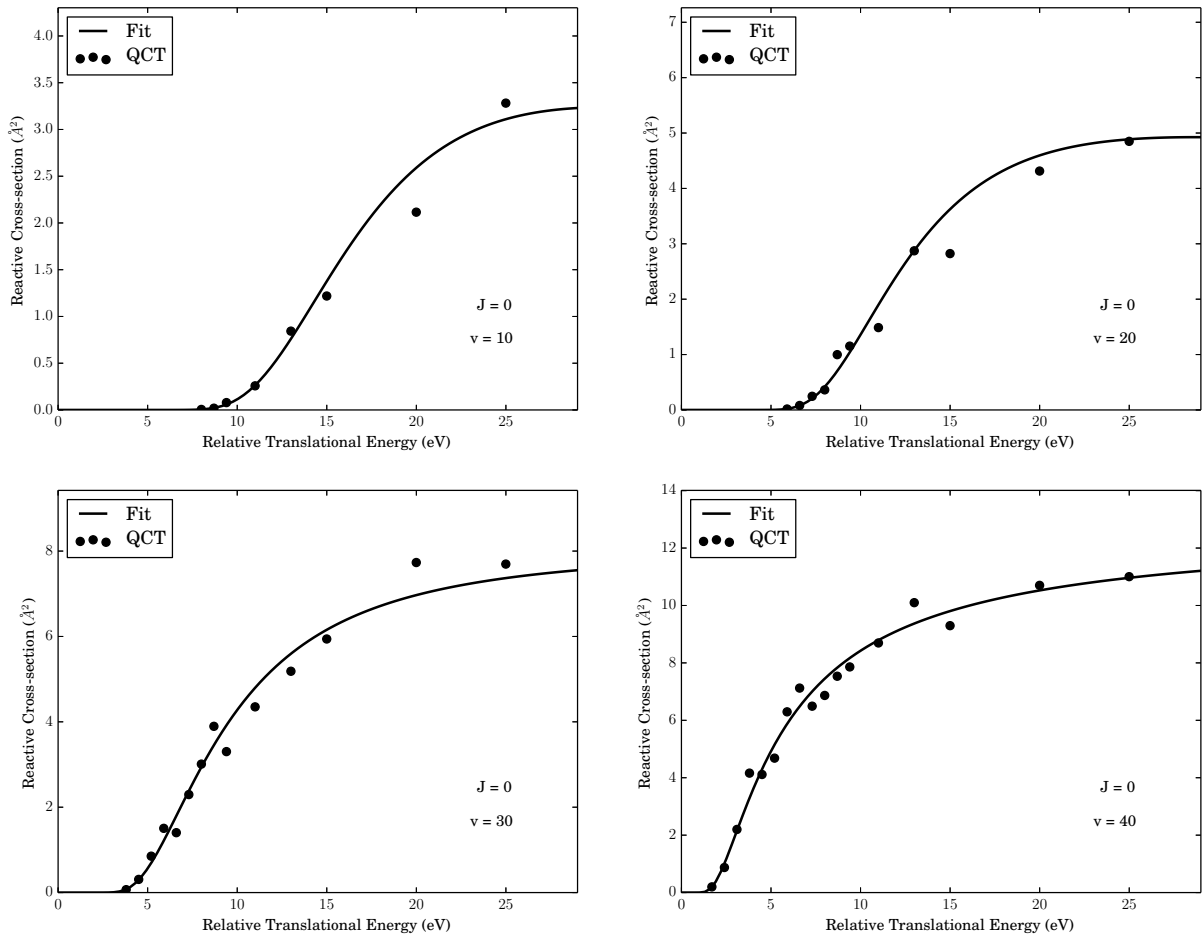


Figure 5.7: Comparison of CID cross-section for the reaction $N_2 + N \rightarrow 3N$ calculated using QCT trials and fitting function for different vibrational levels at $j=0$

the dissociation and exchange cross-section data respectively:

$$\sigma_{r,CID} = 10^{a/x^2+b/x+c} \quad (5.14)$$

$$\sigma_{r,CIE} = 10^{ax^2+b/x+c} \quad (5.15)$$

where x is relative translational energy (in eV) and a, b, c are constants. The function *curvefit* from *scipy.optimize* module in scientific python (SciPy) language is used to find the values of the constants. Comparison of the CID cross-sections obtained from the ab-initio method and their corresponding fitting functions for different vibrational numbers for the N_3 system is shown in Figure 5.7. It is evident that the fit is in a close match with the calculated values.

5.3 Reaction Rate Coefficients

Reactive cross-section results obtained through the PES-QCT method will be used to develop a true non-equilibrium chemistry model. However, the data should at the least match the Arrhenius equation at equilibrium conditions. Integrating the cross-section over the equilibrium distribution function of E_T (or V_R), v and j will give the required dissociation rate coefficients. State specific reaction rates ($k(v_1, v_2, j_1, j_2)$) as a function of temperature obtained by integrating the CID cross-section data with the velocity Boltzmann distribution function can be written as follows

$$k(v_1, v_2, j_1, j_2) = N_A \left(\frac{2^{1/2}}{\pi} \right) \left(\frac{\mu}{k_b T} \right)^{3/2} \times \int_0^\infty \sigma(v_1, v_2, j_1, j_2, V) \exp\left(-\frac{\mu V^2}{2k_b T}\right) V^3 dV \quad (5.16)$$

where N_A is the Avogadro number, k_b is the Boltzmann constant, μ is the reduced mass and T is the temperature.

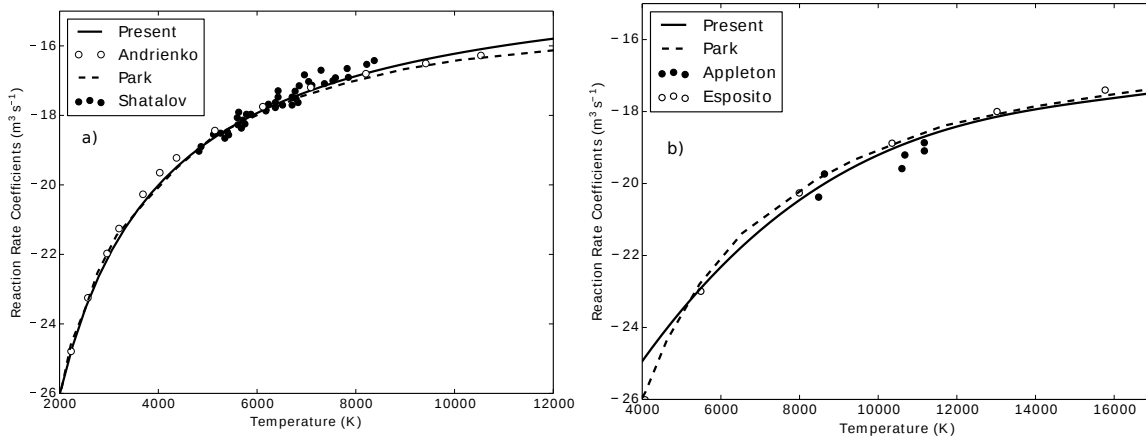


Figure 5.8: Dissociation rate coefficients calculated using data from the calculated cross-section database for the dissociation a) $\text{O}_2 + \text{O} \rightarrow 3\text{O}$ and b) $\text{N}_2 + \text{N} \rightarrow 3\text{N}$ compared with theoretical studies, shock tube experimental results and other computational works.

The state specific reaction rates are integrated over the Boltzmann distributions for both the rotational and vibrational states to get the reaction rate coefficients. In the case of an atom-molecule reaction, the state specific reaction rates are integrated once over rotational and vibrational energy. According to the type of reaction, appropriate degeneracy factors have to be multiplied. For example, a constant factor of $16/3$ [36] that accounts for degeneracy due to multiple electronic states is considered for calculating the dissociation rate coefficients for oxygen colliding with an oxygen atom ($\text{O}_2 + \text{O}$).

The dissociation rate coefficients for reactions $O_2 + O \rightarrow 3O$ and $N_2 + N \rightarrow 3N$ are compared with both experimental[107, 1] and computational results [34]. Figure 5.8 shows that the overall match between the present data and the experimental rates are good. Figure 5.9 a) shows that the reaction rate coefficient for the reaction $O_2 + O_2 \rightarrow O_2 + 2O$ calculated using the present code matches well with the existing experimental results[107, 108] and previous computational results[109]. Figure 5.9 b) shows that the reaction rate for the reaction $N_2 + N_2 \rightarrow N_2 + 2N$ calculated using the present code match well with the experimental results[110, 111, 112] and computational results[113, 33] that use the QCT method results on the same N_4 PES.

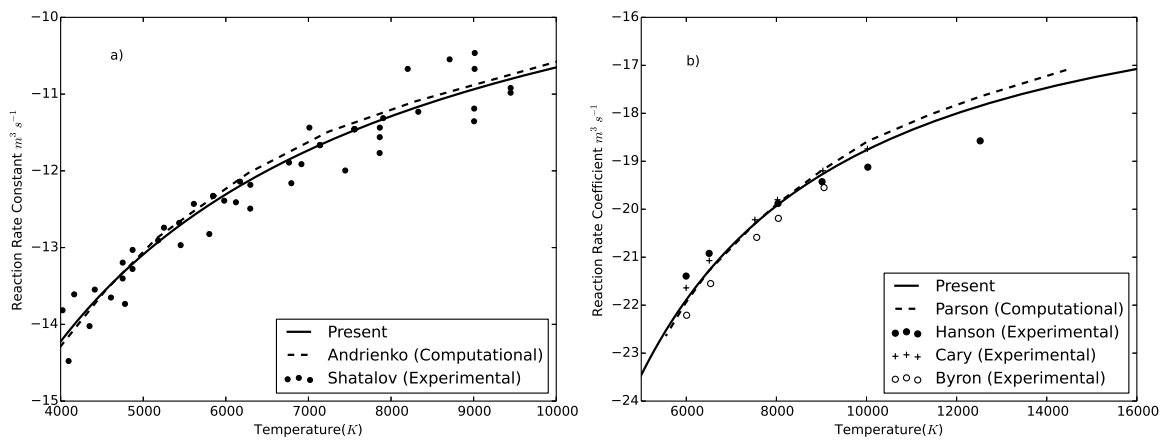


Figure 5.9: Dissociation rate coefficients calculated using data from the calculated cross-section database for the dissociation a) $O_2 + O_2 \rightarrow O_2 + 2O$ and b) $N_2 + N_2 \rightarrow N_2 + 2N$ compared with theoretical studies, shock tube experimental results and other computational works.

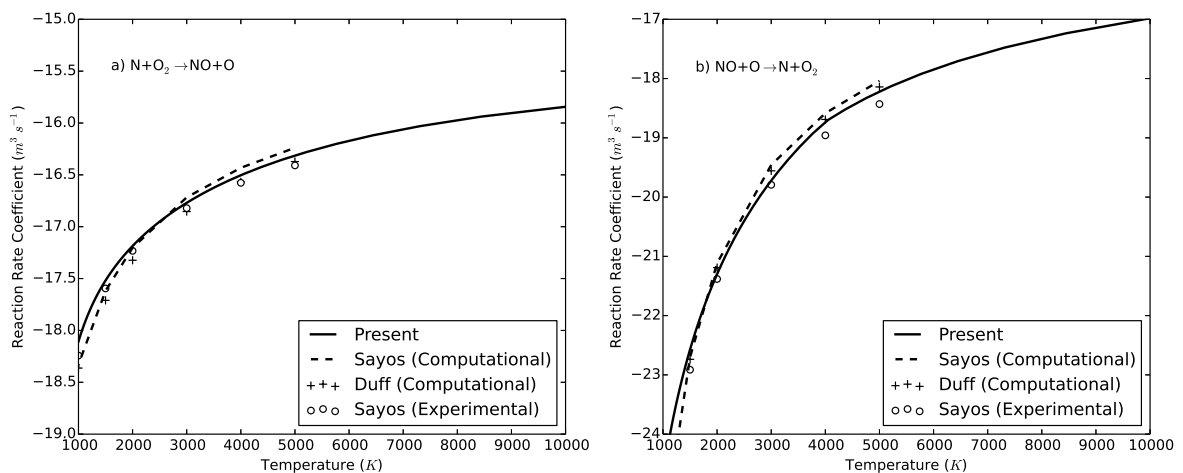


Figure 5.10: Exchange reaction rate coefficients calculated using data from the present work for the exchange a) $N + O_2 \rightarrow NO + O$ and b) $NO + O \rightarrow N + O_2$ compared with experimental results by Sayos et al.[114] and computational results [115, 116, 67]

The cross-sections for Zeldovich exchange reactions are generated for two PESs. In the case of systems pertaining to NO_2 , the final reaction rate coefficient for the exchange reactions is obtained using a weighted formula as reported by Bose et al.[116]

$$k(T) = \frac{1}{6}(k_{2A'}(T) + 2k_{4A'}(T)) \quad (5.17)$$

Figure 5.10 shows the reaction rate coefficients as a function of temperature for forward and backward exchange reactions. It can be concluded from the plots that the reaction rate coefficient as calculated using the present cross-section data match well with the previous experimental data[114] and previous computational results[115, 116, 67].

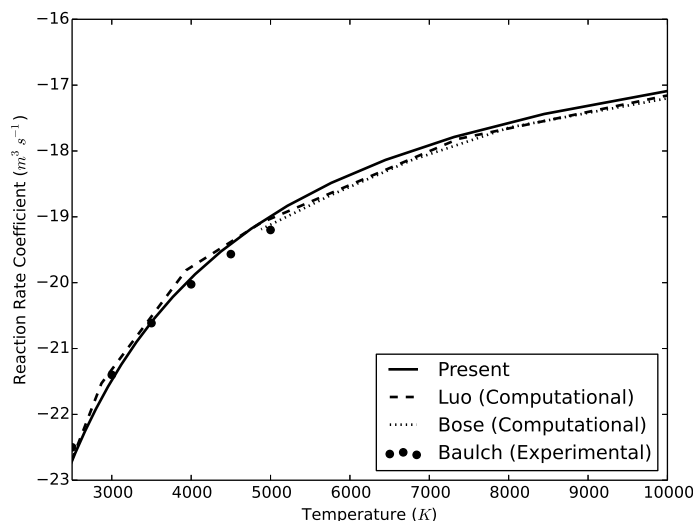


Figure 5.11: Exchange reaction rate coefficients calculated using data from the present work for the exchange $\text{O} + \text{N}_2 \rightarrow \text{NO} + \text{N}$ compared with experimental results by Baulch et al.[117] and computational results [118, 119]

Similarly $\text{N}_2 + \text{O} \rightleftharpoons \text{NO} + \text{N}$ proceeds on two PESs. The final reaction rate coefficients for the exchange reactions pertaining to N_2O system are calculated using the following weighted formula[121]:

$$k(T) = \frac{1}{3}(k_{3A'}(T) + k_{3A''}(T)) \quad (5.18)$$

where $k_{3A'}(T)$ and $k_{3A''}(T)$ are reaction rate coefficients calculated using CIE cross-section database on the two surfaces. Figure 5.11 shows that the reaction rate coefficients calculated in the present study matches well with previous results [117, 118, 119] for the forward reaction.

Additionally, the dissociation rate coefficient of N_2 colliding with atomic oxygen calculated using the CID cross-section on the lowest two N_2O surfaces match well with the reaction rate coefficients for the reaction $\text{N}_2 + \text{N} \rightarrow 3\text{N}$, and the shock tube results for

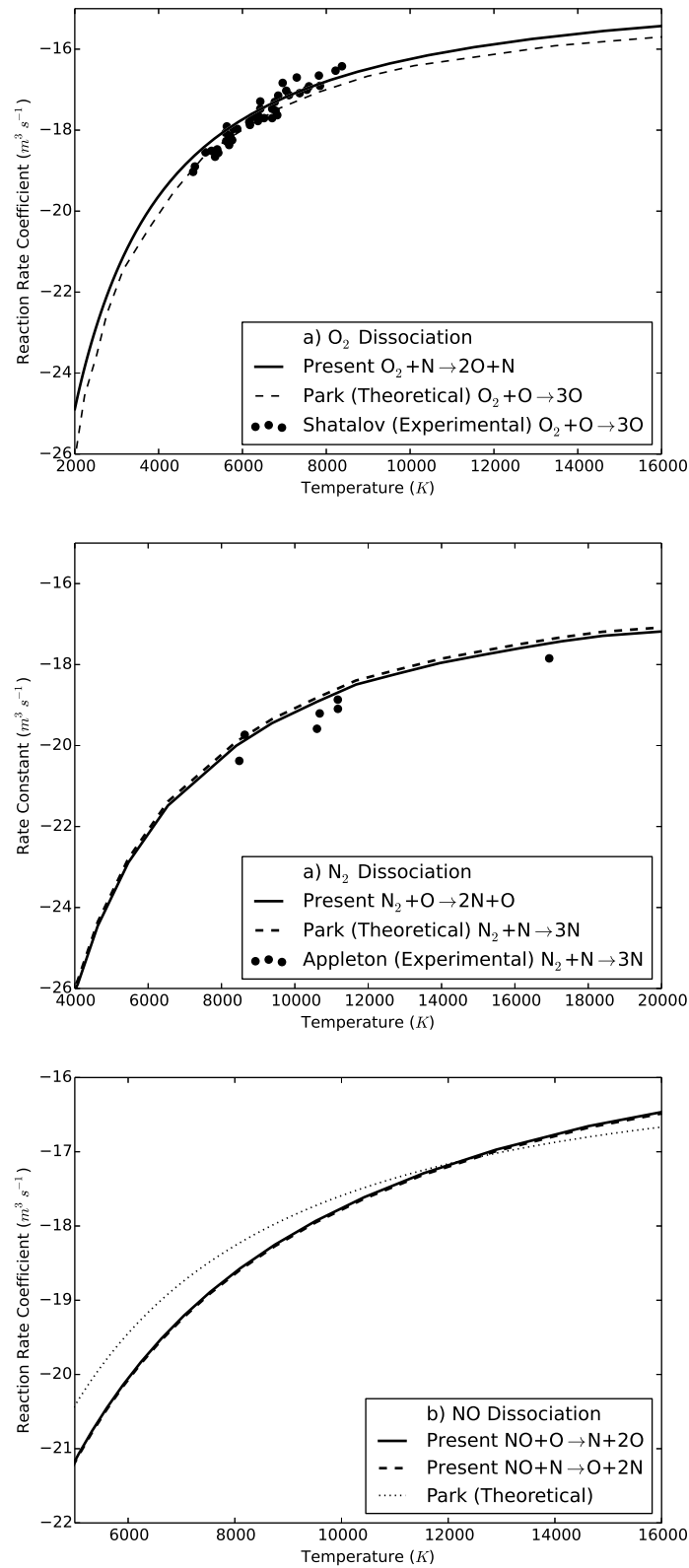


Figure 5.12: Dissociation rate coefficient calculated using the QCT data for a) N_2 dissociation, b) O_2 dissociation and c) NO dissociation compared with previous experimental[120, 107], computational[54, 34] and theoretical work[1].

nitrogen dissociation. Similar, dissociation of oxygen molecule while colliding with atomic nitrogen progressing on the two lowest NO_2 surfaces also match well with dissociation rate coefficient for the reaction $\text{O}_2 + \text{O} \rightarrow 3\text{O}$. The dissociation rate coefficients are shown in Figure 5.12. Figure 5.12 c shows that the QCT study of the NO dissociation upon colliding with other atomic species (N or O) leads to accurate rate coefficients.

5.4 Summary

The cross-section database generated using the QCT method employing the most accurate PESs till date are reliable. This will provide a stable and sound framework for developing an ab-initio chemical reaction model capable of simulating flows with a high degree of non-equilibrium.

Chapter 6

DSMC Simulations of Re-entry flows

The primary objective of this work is to study hypersonic flow around a re-entry vehicle at rarefied ambient atmosphere and to capture the non-equilibrium effects accurately. Towards this end, a new chemical reaction model is developed that calculates reactive cross-section based on a database generated using the QCT method. In comparison with the existing phenomenological models, it is expected that the new ab-initio based chemical reaction model provides a better understanding of the rarefaction and non-equilibrium effects in the flow and predicts the surface heat flux and heat load on the re-entry vehicle more precisely. A comparative study is undertaken to investigate the effects of the different chemical reaction models and varying ambient conditions of the air mixture on the re-entry flows at several altitudes using the DSMC method. The chemical reaction models included in this study are the new ab-initio based chemical reaction model and the Total Collision Energy (TCE) model. The TCE model is more widely accepted as the standard model for handling chemical reaction than the Quantum Kinetic (QK) or the Vibrationally Favoured Dissociation (VFD) model. Also, previously reported comparative studies conclude that the difference between the TCE model and the other models is negligible, and hence only the TCE model is examined as a bench mark for testing the new ab-initio based chemical reaction model.

This chapter begins with a discussion on zero-dimensional DSMC simulations, which provides a further validation of the new ab-initio based chemical reaction model in its application at equilibrium conditions. This is followed by a discussion on the hypersonic flows over re-entry vehicles. Firstly, the re-entry flows with only pure nitrogen or pure oxygen as the working gas are investigated. These simulations, although hypothetical, help in understanding the effects of individual gas chemistries towards the overall flow physics in simulations with practical input conditions.

Finally, a detailed analysis of results of DSMC simulations with air as the working gas

is provided for hypersonic flow over a realistic re-entry geometry at different altitudes. The degree of rarefaction increases with the increase in altitude and subsequent decrease in the ambient pressure. Simulations are run at conditions corresponding to three different altitudes (68km, 80km and 100km). The ambient conditions at 65 km are closer to continuum and hence the DSMC simulations demand high computational resources. In contrast, the ambient conditions at 80 km are rarefied and the flow belongs to transition regime. At 100 km, the flow is nearly collision-less in nature. It can be observed that with increase in altitude, along with number density, the number of collisions decreases drastically. Fewer collisions in the flow result in higher degree of non-equilibrium in the flow. The present comparative study investigates re-entry flows at varying degrees of non-equilibrium.

6.1 Simulation at Equilibrium Conditions

A zero-dimensional DSMC study is initially carried out under conditions that ensure sufficient collisions for equilibrium to occur. The number density, n_0 is taken equal to $2.687 \times 10^{25} m^{-3}$, which corresponds to the ambient density at the ground level. The gas is considered to be made of only nitrogen molecules at high temperature. Atomic nitrogen is assumed to be absent in the beginning and as the simulation progresses, the nitrogen molecules collide with each other and result in atomic nitrogen. A simple phenomenological model is used to simulate atomic recombination reaction that produces molecular nitrogen back[2] and the ab-initio based chemical model is used for the dissociation. Anharmonic oscillator model is used for modeling vibrational levels and temperature dependent rotational[19] and vibrational[122] LB model is implemented for inelastic collisions. The degree of dissociation and the temperature of the system are noted once steady state is achieved. At equilibrium, the temperature corresponding to different modes of energy and the total temperature are equal. This exercise is carried out for different initial temperatures. The variation of the degree of dissociation with equilibrium temperature is compared in Figure 6.1 with the standard theoretical expression:

$$\alpha^2/(1 - \alpha) = (0.5047 \times 10^{28}/n_i)T^{\frac{1}{2}}\{1 - e^{-3395/T}\} \{4 + 10e^{-27658/T} + 6e^{-41495/T}\}^2 e^{-113200/T} \quad (6.1)$$

It can be seen that in addition to the equilibrium reactions rates (shown in Chapter 5), the present chemical model also shows a match with equilibrium degree of dissociation.

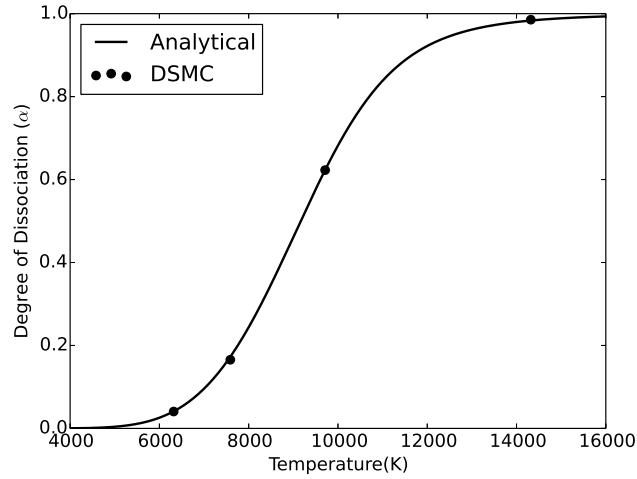


Figure 6.1: Comparison of theoretical equilibrium degree of dissociation and DSMC simulations with ab-initio based chemical model.

6.2 Nitrogen Reactions under Non-equilibrium

As mentioned earlier, the next set of simulations involve nitrogen as the working gas. The reactions that require modelling are:



The simulation conditions chosen, albeit hypothetical, are close to the conditions encountered by a re-entry vehicle at an altitude of ~ 75 km. Simulations are carried out using the parallel implementation of the in-house DSMC code on a distributed computer.

A twelve inch diameter cylinder encounters nitrogen gas flow with stream velocity equal to 10000 m/s. The ambient number density and temperature for the simulations are fixed at $1 \times 10^{21} \text{ m}^{-3}$ and 200 K. Surface temperature of the cylinder is assumed to be at 1000 K.

A regular Cartesian grid with 527×527 cells is constructed in a domain of $1\text{m} \times 1\text{m}$. Temperature dependent Larsen-Borgnakke model is implemented to account for inelastic collisions and exchange of rotational and vibrational energy. In addition to this, anharmonic vibrational levels for molecular nitrogen are considered. The particles colliding with the cylinder are assumed to undergo diffuse reflection. The post-collision velocities and internal energies are re-initialized from the Maxwellian distribution corresponding to the surface temperature. Two sets of simulations are carried out, one using the TCE model and the second using the ab-initio chemical reaction model developed in the present work.

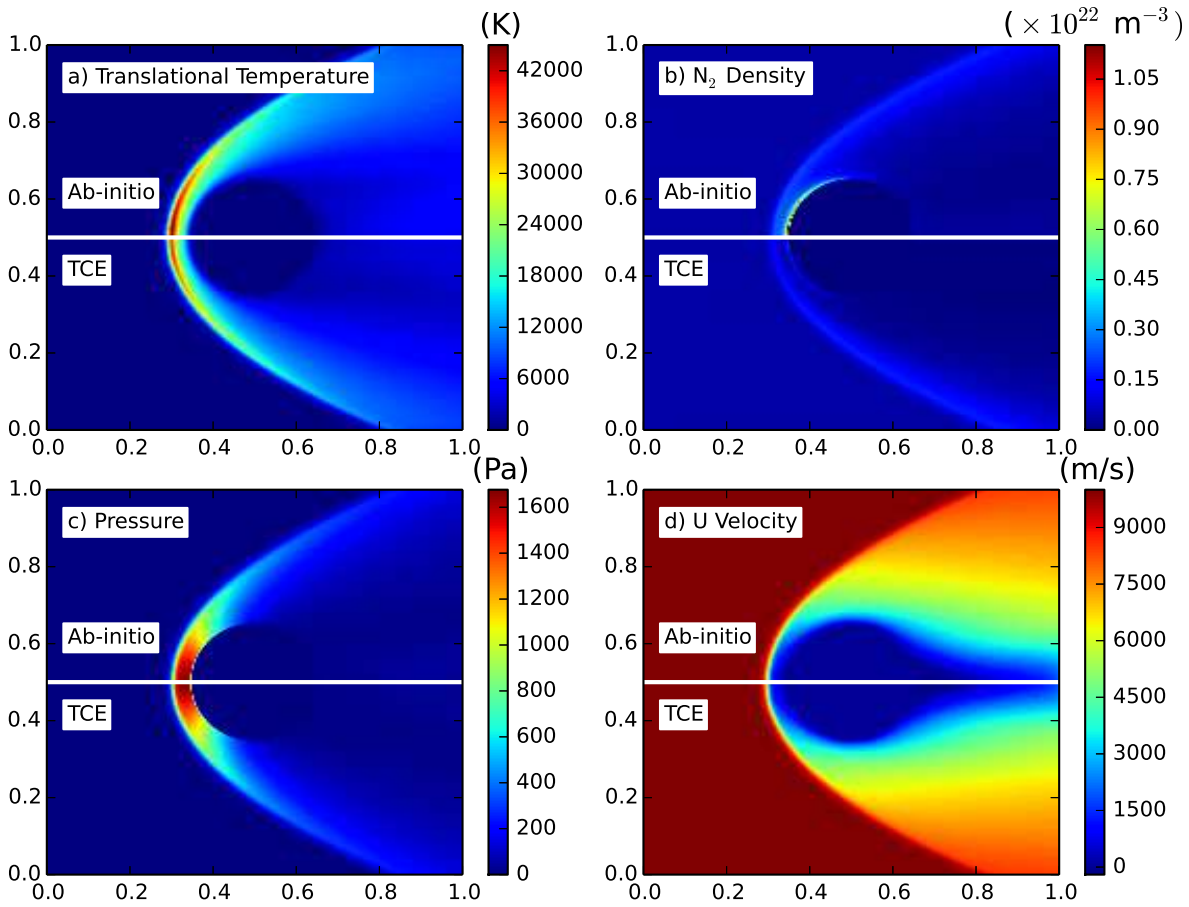


Figure 6.2: Comparison of a) Translational temperature, b) N_2 number density, c) Pressure and d) U Velocity in simulation using the two different chemical models

The contour plots of translational temperature, molecular nitrogen density, pressure and stream velocity in the x direction are shown in Figure 6.2 a), 6.2 b), 6.2 c) and 6.2 d) respectively. In each sub-figure, the upper part of the figure shows the results from the ab-initio chemical reaction model, while the lower part of the figure shows results from the TCE model. The differences in the temperature and N_2 number density predicted by the two models is apparent from Figure 6.2 a) and b) respectively. In contrast, there is negligible difference in the values of pressure and U component of velocity. The characteristic bow shock formation can be visualized from the contour plots. The difference in various modes of temperature is shown in Figure 6.3. It is apparent that the temperatures in each mode are different indicating a high degree of non-equilibrium. This observation is true irrespective of the chemical reaction model used.

The difference in the predicted centreline mole fractions of molecular and atomic nitrogen is shown in Figure 6.4. It is evident that compared to simulations with the TCE chemical model, the degree of dissociation is lesser in the case of simulations with ab-initio

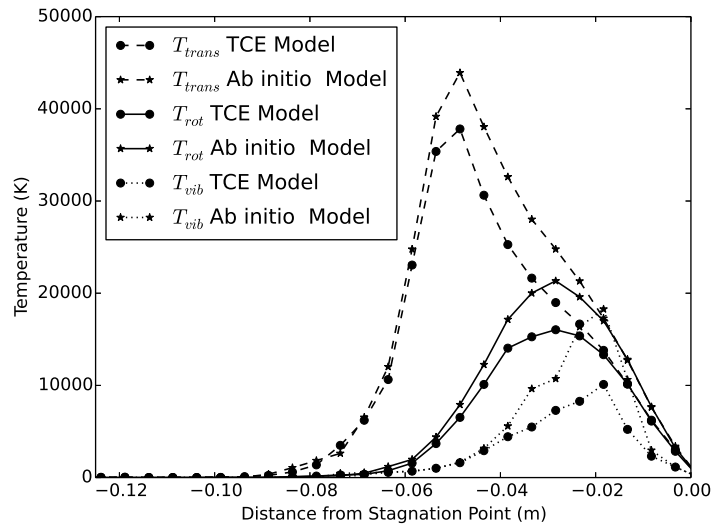


Figure 6.3: Comparison of different modes of temperatures at the centreline for TCE and Ab-initio based chemical model.

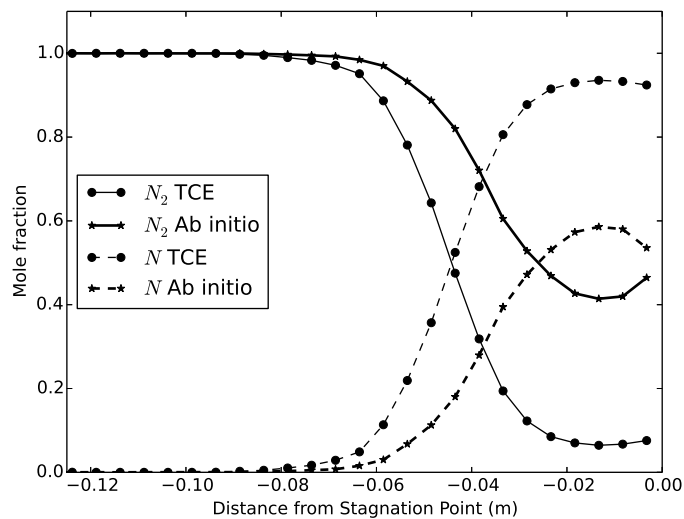


Figure 6.4: Comparison of mole fraction of the two species at the centreline for TCE and Ab-initio based chemical model.

based chemical model. This result can be attributed to the high degree of non-equilibrium in the flow. The ambient temperature of the initial flow is 200 K and all nitrogen molecules are in their lowest vibrational state. In the shock and the post-shock region, the collisions are fewer than those happening in an equilibrium flow. Fewer collision events lead to a non-equilibrium situation and fewer nitrogen molecules are at higher vibrational levels. The difference in the results is due to significant differences observed in the cross-section values in the two models as discussed below.

Figure 6.5 shows a comparison of the absolute values of the CID cross-sections calcu-

lated using the ab-initio studies and the assumed form of the cross-section as predicted by the TCE model for N_3 system. In the figure, the molecules are in their zeroth rotational quantum number. It can be observed that the shapes of the CID cross-section plots are different for the TCE and the ab-initio model. Further, the difference is more pronounced for collisions of N_2 molecules occupying lower vibrational levels. At the zeroth vibrational level, the TCE model predicts a much higher cross-section at lower relative translational energy. The maximum relative translational energy for collision in the shock region observed from the simulations is less than 12 eV. It is noticeable from Figure 6.5 that the reactive cross-section predicted by the ab-initio chemical model is lower than the corresponding reactive cross-section predicted by the TCE model. This is the prime reason for the difference in degree of dissociation in the shock region. A serious limitation of the TCE chemical model is that it does not distinguish between the different modes of energy whereas the reactive cross-section calculated using ab-initio methods includes the vibrational level as an input variable. The influence of the vibrational levels on the cross-section is prominent and hence DSMC results with TCE chemical model can be erroneous under non-equilibrium conditions though clearly under equilibrium conditions the two models predict exactly the same results.

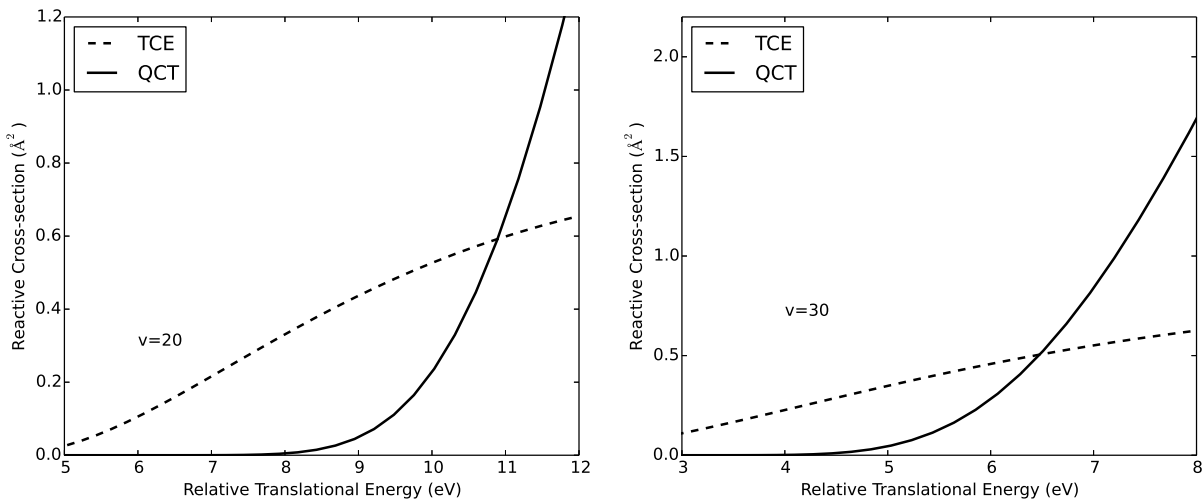


Figure 6.5: Cross-sections as calculated using the assumed form for TCE and those obtained from the QCT studies for two vibrational numbers ($v=20,30$) for $N_2 + N$ reaction.

The maximum relative translational energy for collision in the shock region observed from the simulations is less than 12 eV. It is noticeable from Figure 6.5 that the reactive cross-section predicted by the ab-initio chemical model is lower than the corresponding reactive cross-section predicted by the TCE model. This is the prime reason for the difference in degree of dissociation in the shock region. A serious limitation of the TCE chemical model is that it does not distinguish between the different modes of energy

whereas the reactive cross-section calculated using ab-initio methods includes the vibrational level as an input variable. The influence of the vibrational levels on the cross-section is prominent and hence DSMC results with TCE chemical model can be erroneous under non-equilibrium conditions.

Higher degree of dissociation in the case of simulation with TCE chemical model directly affects the value of various modes of temperature (Figure 6.3). For simulation with TCE, a higher portion of the flow enthalpy is utilized in breaking bonds in dissociation and hence the flow temperatures are lowered. This also affects the heat flux experienced by the cylinder surface. A comparison of coefficient of heat flux on the cylinder with angle subtended at the centre of the cylinder is shown in Figure 6.6. The heat flux is normalized in the following manner:

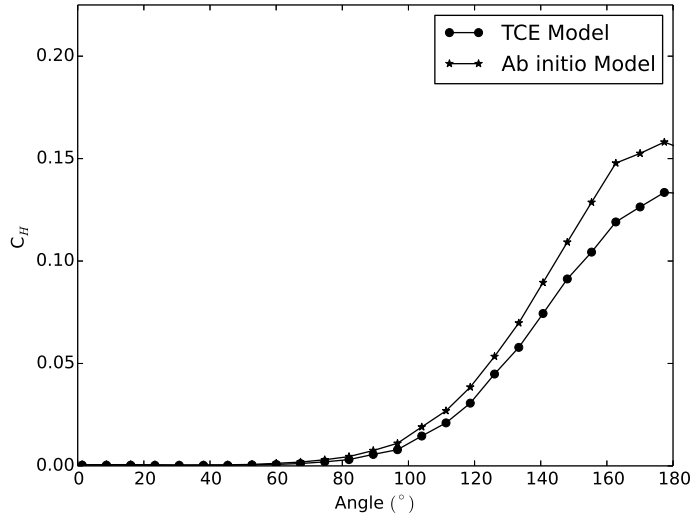


Figure 6.6: Comparison of non-dimensional heat flux on the cylinder surface for TCE and Ab-initio based chemical model.

$$C_H = \frac{q_h}{\frac{1}{2}\rho u_\infty^3} \quad (6.4)$$

where q_h is heat flux, ρ is inlet density and u_∞ is inlet velocity in the x direction. The 180° on the x-axis corresponds to the stagnation point on the cylinder and this point encounters the maximum particle collisions and heat flux. The heat flux experienced by the cylinder at the stagnation is about 8% higher for the ab-initio based chemical model in comparison with the TCE chemical model. This is a direct consequence of lower dissociation in the case of DSMC simulations with the ab-initio based chemical model.

A different result that is again a direct outcome of the two reaction models can be further demonstrated using shock tube simulations. Shock tube studies are essential ex-

periments used for investigating a wide range of applications. A shock tube under rarefied conditions containing Nitrogen gas is simulated wherein cross-sections are implemented using the ab-initio method as well as the classical TCE model. The length of the shock tube is 1 cm and the diaphragm is placed at the centre. The number density and temperature on the driver side are $8.15 \times 10^{25} \text{ m}^{-3}$ and 9000 K while that on the driven side are $2.44 \times 10^{25} \text{ m}^{-3}$ and 300 K respectively. At the start of the simulation, the horizontal velocity in both sections is zero. In the driver section, the mole fractions of molecular and atomic nitrogen are calculated using the equilibrium degree of dissociation at 9000 K, while the driven section is entirely composed of molecular nitrogen due to the low temperature. The shock tube is discretized into 1856 cells each having a cell size of 0.0005389 cm. A time step of 1×10^{-10} s is chosen for the simulation. Unlike the steady state problems, a combination of time and ensemble sampling is used to average the microscopic properties in order to calculate macroscopic properties using the standard kinetic theory relations.

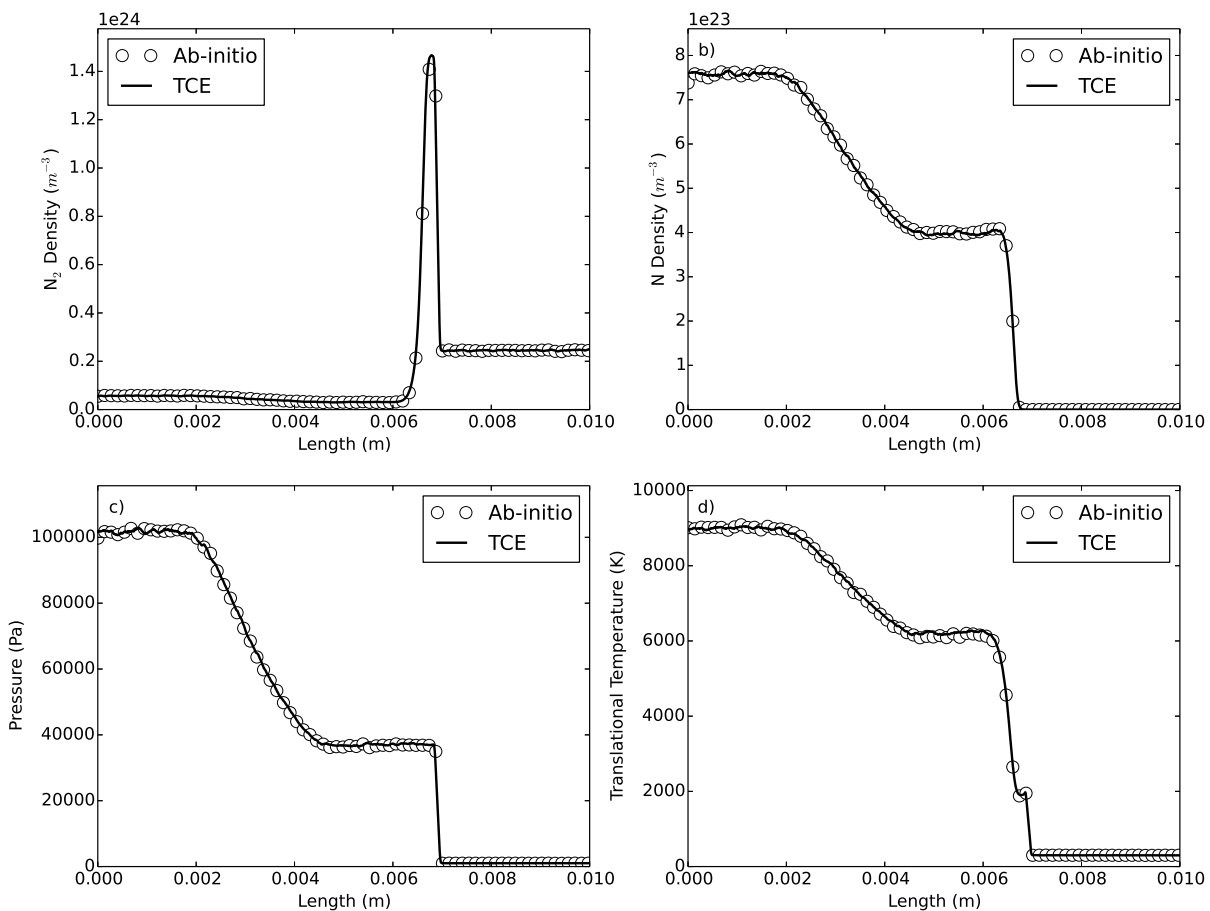


Figure 6.7: Comparison of a) number density of N_2 , b) number density of N, c) translational temperature and d) pressure for simulations employing TCE and Ab-initio based chemical models.

The line plots of molecular and atomic nitrogen number density, translational tem-

perature and pressure for simulations with TCE and ab-initio based chemical model at 1×10^{-6} s after the start of the simulations are shown in Figure 6.7. The characteristic plots of pressure and temperature similar to standard Sod shock tube case can be observed. The driver and driven sections are predominantly composed of atomic and molecular nitrogen respectively. Hence the region between the contact discontinuity and the shock wave front is the region of interest where high velocity collisions occur. The effect of the chemical reaction models can be observed in this region. The enlarged view of the line plot of molecular nitrogen number density is shown in Figure 6.8.

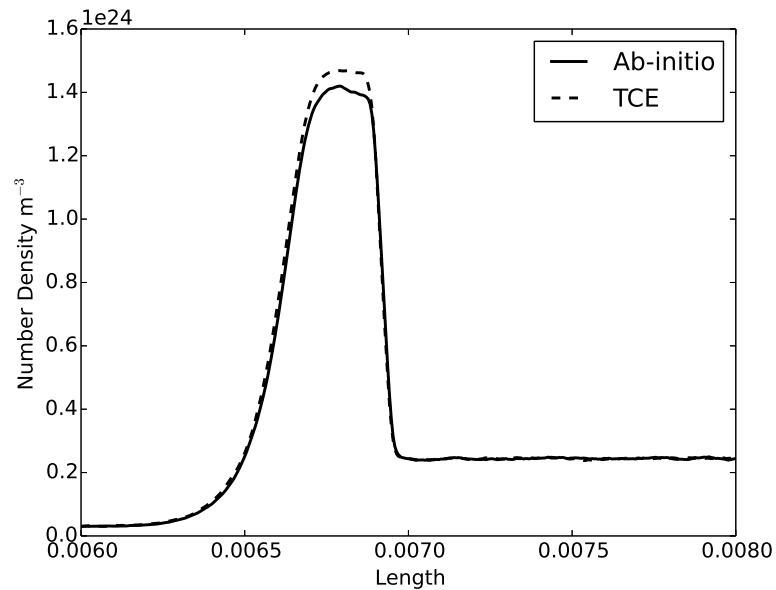


Figure 6.8: Comparison of number density of N_2 for simulations employing TCE and Ab-initio based chemical models between the contact discontinuity and shock wave.

In contrast to the mole fraction results obtained in the re-entry flow simulation, it is clear that the ab-initio model predicts a higher dissociation rate for Nitrogen when compared to the TCE model in this case. This is again because of the difference in the shape and the form of the cross-section assumed in the TCE model and as calculated using the ab-initio method for different ro-vibrational levels as seen in Figure 6.5. Initially, the gas in the driver section is maintained at a high temperature and it is in equilibrium. At such high temperatures, the gas consists of both dissociated and undissociated nitrogen gas. In the case of re-entry flows, all nitrogen molecules in the pre-shock region were in the ground state as the ambient temperature is below the vibrational excitation temperature. In comparison, the vibrational level distribution of the undissociated molecular nitrogen in the driver section of the shock tube follows the Maxwell-Boltzmann probability distribution function at the driver section temperature: 9000 K and a large number of nitrogen molecules reside in excited vibrational levels. As the shock wave progresses, these excited

nitrogen molecules in the driver section collide with the gas particles in the driven section. These collisions may further lead to dissociation. As stated earlier, the TCE model does not include the varying influence of the individual form of energies. Instead, the cross-section is simply a function of the sum of all energies. It is obvious from Figure 6.5 that there is a higher degree of disagreement between the cross-sections predicted by the two models at higher vibrational levels. The cross-sections predicted by the ab-initio based chemical reaction model for such collisions at the shock front are greater than those predicted by the TCE model. This leads to a higher dissociation rate in simulations with the ab-initio chemical reaction model. This is apparent from Figure 6.8. This exercise on shock tube study elucidates the limitation of the TCE model and the need for ab-initio based chemical reaction model.

6.3 Oxygen Reactions under Non-equilibrium

Similar to the previous set of simulations for Nitrogen flow over an infinite cylinder, a set of DSMC simulations is carried out for flow of only molecular Oxygen over an infinite cylinder with the same domain size and ambient conditions as for Nitrogen flow[123]. In this case, the oxygen dissociation forms the model chemistry:



In contrast to the study with Nitrogen gas, the flow of Oxygen gas is simulated at two different re-entry speeds ($U_\infty = 5000 \text{ m/s}$, 10000 m/s). This is done to analyze the effect of the inlet velocity and further highlight the difference in the chemistries of the two inlet gas systems.

A comparison of pressure (Figure 6.9 a,b), total temperature (Figure 6.9 c,d) and x component of velocity (Figure 6.9 e,f) in the flow field for the two chemistry models at the two re-entry speeds is shown in Figure 6.9. The characteristic bow shock is noticeable from the contour plots. A major deduction revealed from this primary analysis is that the flow field values of all macroscopic properties as predicted by the DSMC simulation at higher re-entry speed ($U_\infty = 10000 \text{ m/s}$) with the TCE chemical model match exactly with the corresponding values as calculated by the simulations employing the ab-initio chemical model. In contrast, the simulations run at lower re-entry speed ($U_\infty = 5000 \text{ m/s}$) predict results with a significant difference. This can be again attributed to the difference in the shapes of CID cross-sections in the two models as shown in Figure 6.10.

Since at the zeroth vibrational level, the TCE model has a higher cross-section at

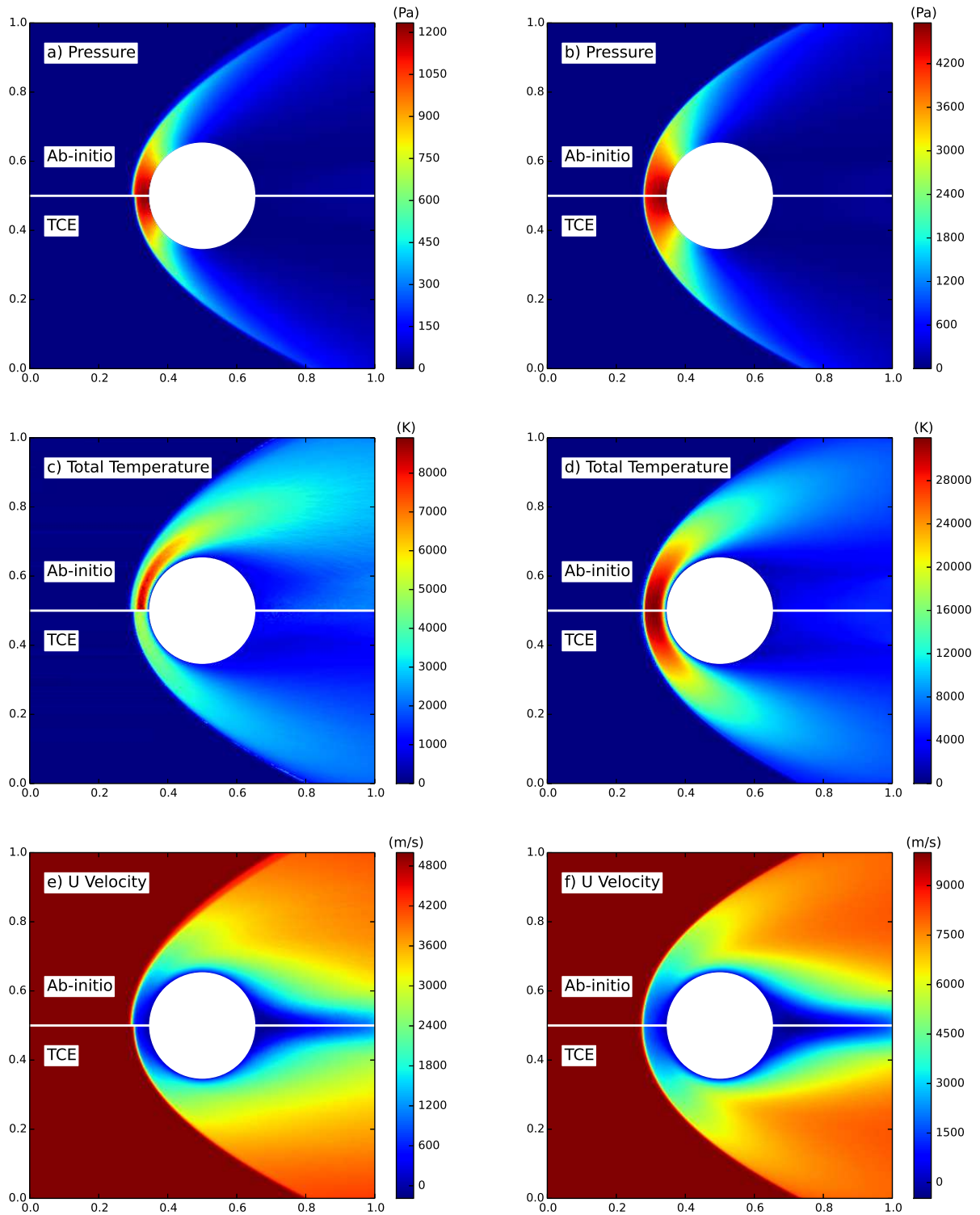


Figure 6.9: Comparison of contour plots of Pressure, Total Temperature and U velocity, (x component of velocity) for DSMC simulations employing TCE and Ab-initio chemical models for low ($U_\infty = 5000$ m/s) (Sub figure a, c and e) and high ($U_\infty = 10000$ m/s) (Sub figure b, d and f) inlet velocity.

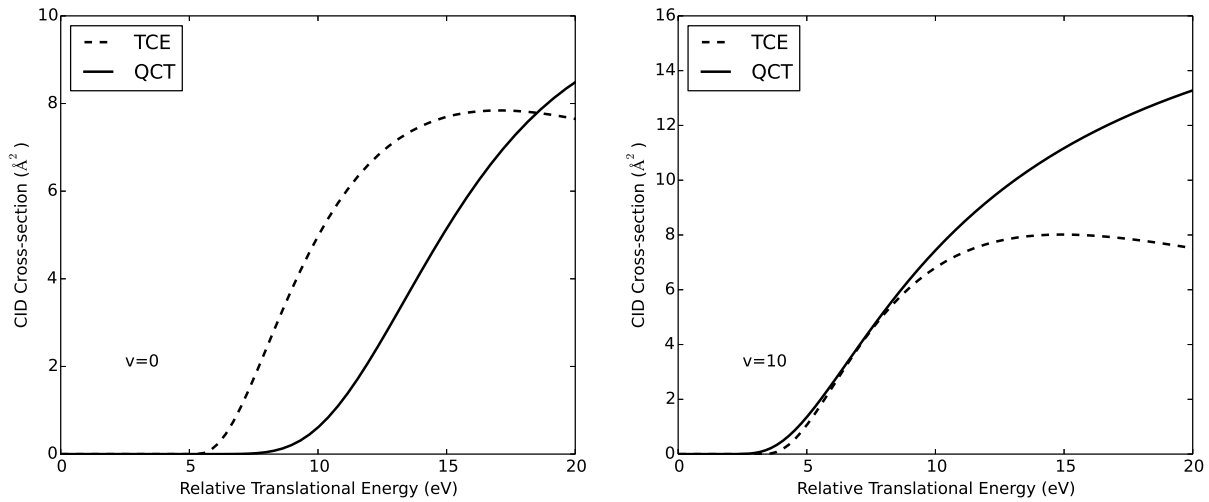


Figure 6.10: Comparison of CID cross-sections predicted by the TCE model and the ab-initio method for reaction $O_2 + O_2 \rightarrow O_2 + 2O$ at different vibrational numbers ($v_1 = v_2 = 0, 10$) and zeroth rotational number.

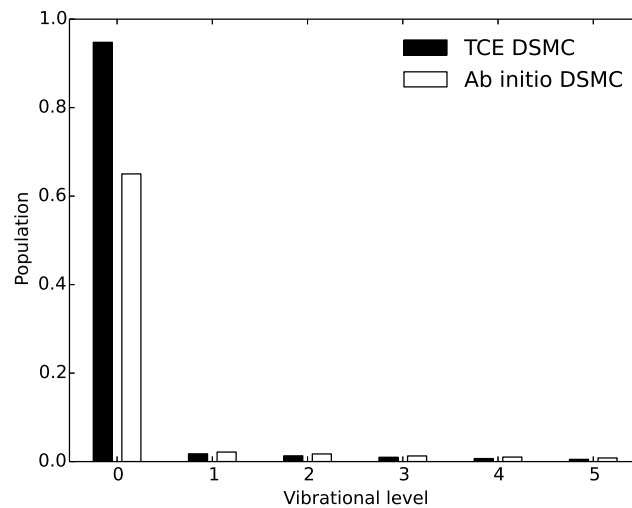


Figure 6.11: Comparison of population distribution (bar plot) of oxygen molecules in vibrational levels at the shock front acquired from DSMC simulations at $U_\infty = 5000$ m/s employing TCE and Ab-initio chemical models.

lower energies (as compared to the ab-initio model), it predicts a higher dissociation of oxygen at the zeroth vibrational level. A histogram showing the occupancy of vibrational levels, $v = 0$ to 5, is shown in Figure 6.11 for the re-entry speed U_∞ equal to 5000 m/s. It is clear that the simulation using the TCE model predicts an occupancy of 94% at the zeroth vibrational level, whereas the simulation with the ab-initio model predicts only 65% occupancy at this level. Thus, overall the TCE model predicts a far higher dissociation of Oxygen. This is clearly visible in Figure 6.12 a, which is a centreline plot of mole fraction of the two species: molecular and atomic Oxygen, at a re-entry speed of 5000 m/s. In this

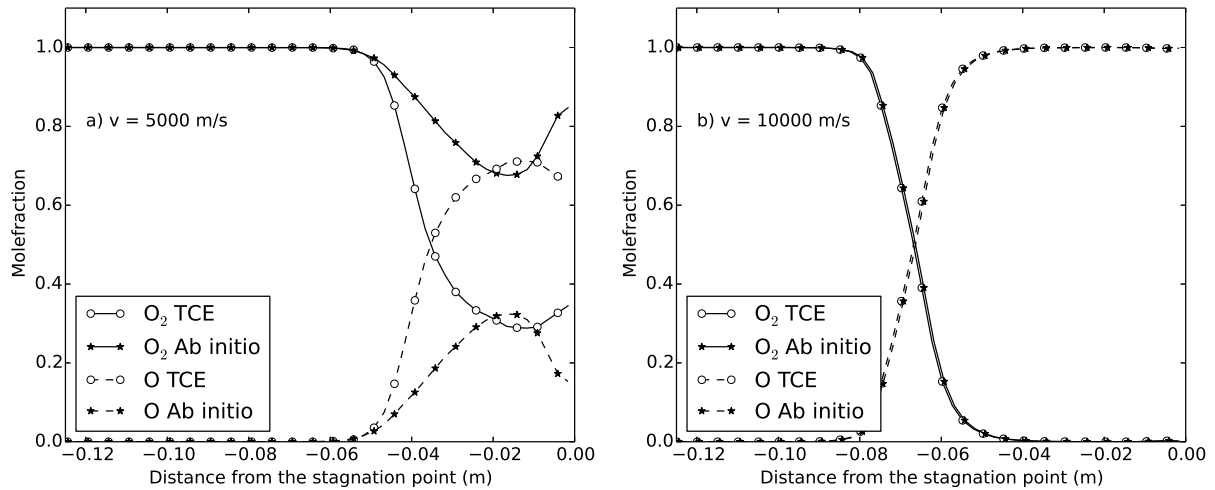


Figure 6.12: Comparison of centre-line plots of mole fraction of molecular and atomic Oxygen for DSMC simulations employing TCE and Ab-initio chemical models for a) low ($U_\infty = 5000$ m/s) and b) high ($U_\infty = 10000$ m/s) inlet velocity.

case, it can be clearly seen that the TCE model predicts a much higher mole fraction of atomic oxygen due to higher level of dissociation. In contrast, at higher enthalpy ($U_\infty = 10000$ m/s), the post shock region consists entirely of atomic Oxygen with the maximum degree of dissociation irrespective of the chemical model employed (Figure 6.12 b). This is due to the fact that the energy in the post shock region is much higher than the bond energy and thus only traces of molecular Oxygen are left.

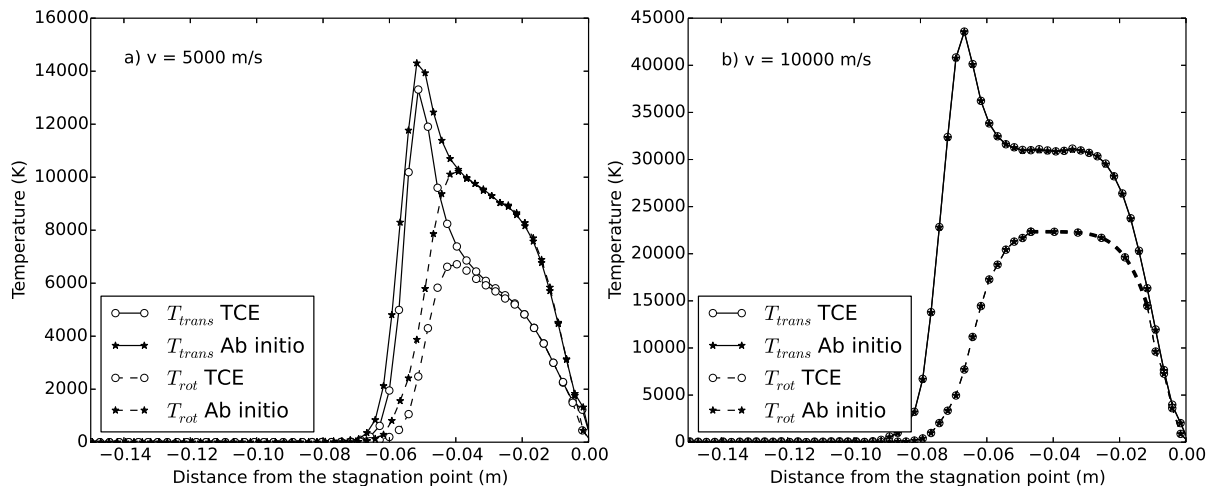


Figure 6.13: Comparison of centre-line plots of different modes of temperature (Translational, Rotational and Vibrational modes) for DSMC simulations employing TCE and Ab-initio chemical models for a) low ($U_\infty = 5000$ m/s) and b) high ($U_\infty = 10000$ m/s) inlet velocity.

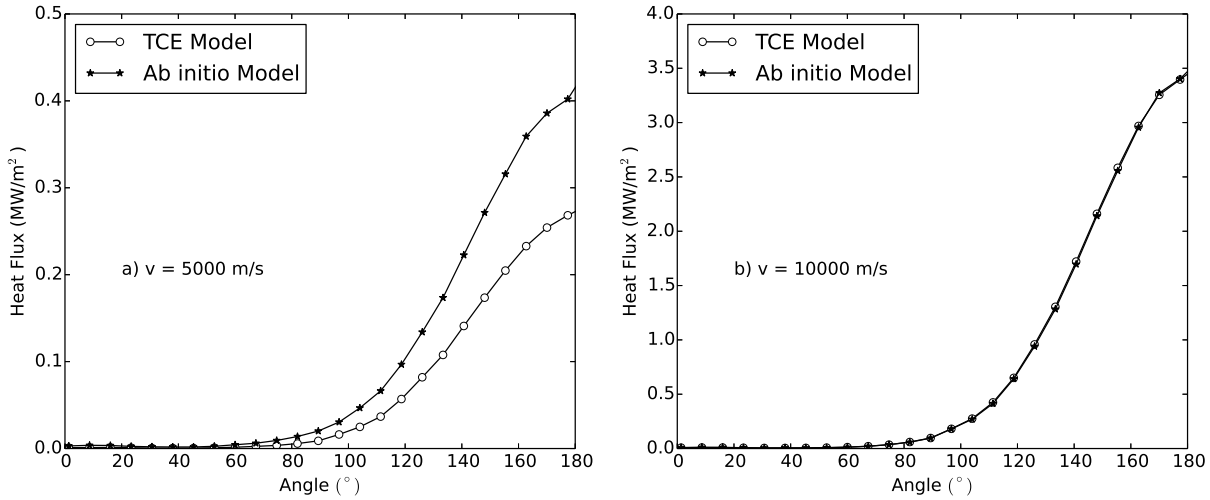


Figure 6.14: Comparison of surface heat flux along the surface of the cylinder for DSMC simulations employing TCE and Ab-initio chemical models for a) low ($U_\infty = 5000$ m/s) and b) high ($U_\infty = 10000$ m/s) inlet velocity.

In the case of DSMC simulation at lower re-entry speeds, the higher degree of dissociation with the TCE model leads to lower enthalpy in the field and in turn lower values of different modes of temperature compared to the ab-initio model. This is observed from Figure 6.13 a). In the case of DSMC simulation at higher re-entry speed, the degree of dissociation and the mole fractions of the two species predicted by either chemical models are equal. Hence, the centreline temperatures (Figure 6.13 b) overlap perfectly.

Figure 6.14 a) and b) shows the variation of heat flux as a function of angle subtended at the centre. In the figures, an angle of 180° represents stagnation point on the surface. A direct consequence of the higher degree of dissociation is the lower heat flux exchange with the cylinder surface as observed in the case of DSMC simulation with TCE model and lower re-entry speeds.

It can be concluded that for very high enthalpy simulations in pure Oxygen environment, employing either the TCE model or the ab-initio chemical model will predict the same flow field and centreline properties. This inference is different from the study of hypersonic flow of pure Nitrogen reported in the previous section[105], where it was observed that at $U_\infty = 10000$ m/s, there were significant differences in the flow field mole fractions of molecular and atomic nitrogen (Figure 6.4), different modes of temperature (Figure 6.3) and surface heat flux as predicted by the two models. This is due to the shape of the CID cross-sections for Nitrogen. In conclusion, the effect of different set of reactions have contrasting effects on the flow and surface properties on the re-entry vehicles as expected.

6.4 Stardust Re-entry Simulations

6.4.1 Stardust Geometry

In the previous sections, the effect of individual dissociation systems during hypersonic flow situations has been investigated. The next logical step is to include all five major species of air chemistry and the additional chemical reactions in order to simulate re-entry flows in realistic conditions. Towards this end, hypersonic air flow around the Stardust Re-entry Capsule (SRC) are simulated at different ambient conditions. The aim of the Stardust mission was to collect dust samples from the coma of the Comet Wild 2. Unlike the traditional re-entry capsules that have a blunt forebody, the Stardust re-entry vehicle had a more streamlined shape (Figure 6.15). The re-entry speed of the Stardust Re-entry was also significantly higher than its predecessors. Its re-entry speed at an altitude of 100 km was in excess of 12 km/s, whereas previous missions such as the FIRE-II mission had re-entry speeds around 6 km/s. At altitudes above 70 km, the effect of ionization reactions and radiative heat transfer on the flow physics for Stardust re-entry is significant. Ideally, these effects should be included when simulating such flows. However, in the present work, the focus is to study the effect of the new ab-initio based chemical reaction model. Hence, the simulations are restricted to the chemical reactions, while ionization reactions and radiative heat transfer modelling are not included. The dimensions of the Stardust geometry are shown in Figure 6.15.

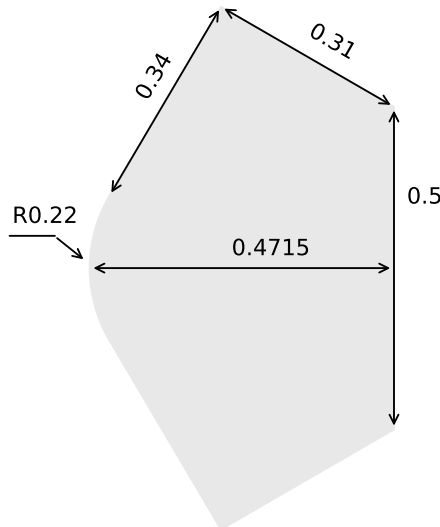


Figure 6.15: Stardust Re-entry capsule.

6.4.2 Ambient and Computational Variables

Simulations are carried out at ambient conditions corresponding to three different altitudes: 100 km, 80 km and 68 km. At 100 km, the ambient pressure is highly rarefied and accordingly the Knudsen number is large ($\gg 1$). The flow at such conditions is closer to the free molecular flow regime. The gas encounters few particle-particle collisions. In other words, the flow is nearly collision-less. In contrast to this, the ambient conditions at 80 km are less rarefied and the flow belongs to the transition flow regime. The DSMC method is the most suitable for simulating flow at these conditions. With further decrease in the altitude, the ambient conditions of the flow are closer to the continuum flows. In comparison to the other two altitudes, the flow at 68 km is the densest, has a higher collision frequency and hence the DSMC simulations are more computationally expensive. The ambient conditions at the three altitudes are tabulated in Table 6.1.

Table 6.1: Ambient conditions at different altitudes

	68 km	80 km	100 km
Number Density (m^{-3})	1.60×10^{21}	4.18×10^{20}	1.19×10^{19}
Temperature (K)	224	185	181
N ₂ mole fraction	0.7628	0.79	0.78
O ₂ mole fraction	0.2372	0.21	0.18
O mole fraction	0.0	0.0	0.04
U_∞ (m/s)	11.9	12.8	12.8
Kn_∞	0.010	0.82	5.24

The Stardust geometry is placed at the centre of a 1.4 m \times 1.6 m domain that is discretized using a regular Cartesian grid. The number of cells in the domain are 140 \times 160, 532 \times 608 and 1130 \times 1290 for DSMC simulations at 100 km, 80 km and 68 km respectively. Based on heuristic considerations, the simulation at 100 km could have been carried out using only 15 \times 17 cells, but it is considered to be too coarse. The time-step for all DSMC simulations is taken to be 2.5×10^{-8} s. The time-step chosen is much lower than the mean collision time at 100 km altitude to ensure that the particles do not cross multiple cells in one time step. No Time Counter (NTC) and Variable Hard Sphere (VHS) models are employed to handle collisions. Temperature dependent Larsen-Borgnakke (LB) model is implemented for both rotational and vibrational energy exchange. Anharmonic vibrational levels are assumed for the molecules. Two simulations are implemented at each altitude employing the two chemical reaction models: Total Collision Energy (TCE) and ab-initio based chemical reaction model. Diffuse surface boundary condition is assumed and the surface temperature is assumed to be constant at 1000 K. The simulations reach steady state by 0.1 ms. A sample of 25000 time steps from the steady state is used to

calculate the macroscopic quantities using the standard kinetic theory formulations.

6.4.3 Results and Analysis

The simulations are run on a parallelized Fortran DSMC framework on an Intel Xeon processor distributed system. The computational domain for the simulations at 68 km and 80 km is divided horizontally into 24 segments. These segments are handled by individual threads or processors. Each processor implements the DSMC algorithms for particles and cells confined to their respective partition of the domain. As the particles move, few particles may cross the segment boundary and travel to the region of the domain that is handled by a different processor. After every DSMC time step, the information of the particles that have crossed the segment boundary is communicated with their new processors. The information is appended to the existing list of particles in the new processor. The DSMC simulations at 100 km altitude are carried out serially since the grid used is much coarser than the other two, and hence these simulations are not computationally expensive. The total computational run times per DSMC step for the different simulations after attaining the steady state is tabulated in Table 6.2. For DSMC simulations at 68 km and 80 km, the average computational time shown in the table is multiplied with the number of threads used (24 in present case) in parallel implementations. An analysis of the simulation at 80 km altitude showed that the communication module took only 1.6 % of the time and thus the present algorithm is computation bound. In comparison to this, the movement, collision and sampling took 47%, 31% and 17% computational time respectively.

Table 6.2: Computational run time per time-step(s)

Altitude (km)	Computational time per DSMC step (s)	
	TCE Model	Ab-initio
100	1.29024	1.3547
80	19.265	22.871
68	87.716	97.910

It is evident from the computational time study that the DSMC simulations employing the TCE chemical reaction model are faster compared to the DSMC simulations employing the ab-initio based chemical reaction model. This is because a higher number of operations are used in the calculation of reactive cross-section in the ab-initio based chemical reaction model compared to the TCE model. Unlike the TCE model, which uses a single analytical expression with just two parameters, the ab-initio model employs a large number of fitting parameters and additional time is used for accessing the correct

set of parameters. Further, more computationally expensive operations such as the exponential function are employed in the cross-section fits.

Similar to the results of Nitrogen and Oxygen flow over the cylinder, the characteristic bow shock is formed in front of the re-entry geometry in all simulations. In addition to the bow shock, several interesting shock structures are generally formed in the hypersonic re-entry flows such as the stagnation on the nose of the re-entry vehicle, thin viscous boundary layer, shock-boundary layer interactions, expansion waves, recirculation zone and stagnation region in the afterbody, viscous core and shear recompression in the flow downstream. The degree of rarefaction also affects the strength and position of these features. The streamline plots around the re-entry vehicle calculated in the present set of simulations shown in Figure 6.16 depict some of these interesting shock structures. Figure 6.16 a) b) and c) show the streamline patterns in the flow around the re-entry vehicle at 68 km, 80 km and 100 km respectively in the DSMC simulations employing the TCE model. The chemical reaction model has no significant effect on the streamlines.

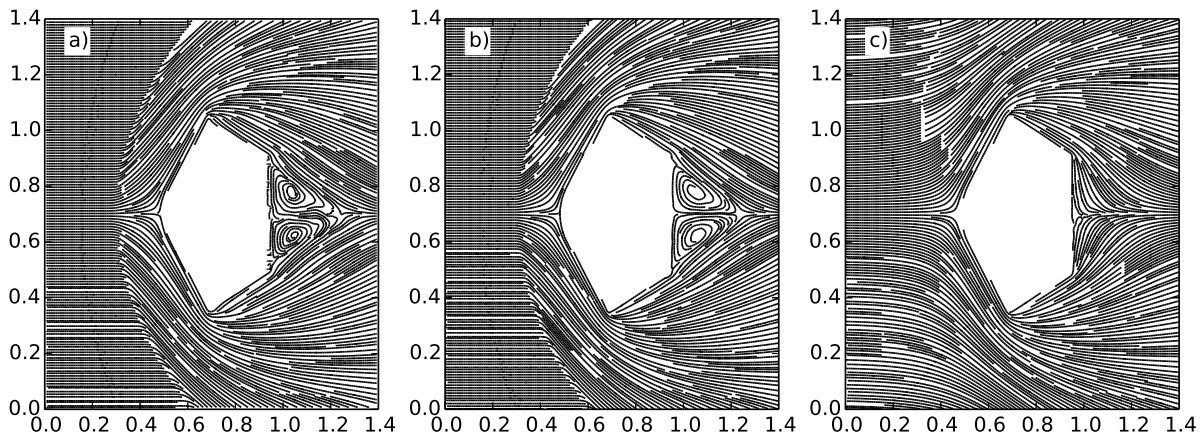


Figure 6.16: Comparison of streamline plots for DSMC simulations a) at 68 km, b) at 80 km and c) 100 km.

Several important inferences can be made from the comparison of the streamline plots. The strength of the bow shock in the flow field is considerably stronger at 68 km compared to that at 100 km altitude. This is evident from the sharp change in the streamlines in the case of simulations at 68 km. The streamlines in the forebody of the re-entry vehicle at 100 km change gradually. This difference in the sharpness of the shock is also observed from the flow property contour plots shown in Figure 6.17, 6.18 and 6.19 (Subfigure a), b) and c) are plots at 68 km, 80 km and 100 km respectively). In each sub-figure, the upper part of the figure shows the results from the ab-initio chemical reaction model, while the lower part of the figure shows results from the TCE model.

It is noteworthy that the most striking difference in the streamline plots at the three altitudes is the recirculation zone and the stagnation region in the downstream of the vehicle. The prominent recirculation zone in the flow at 68 km is short in length which is followed by a small stagnation region located at around 0.3 m from the rear end of the re-entry vehicle. The length of the recirculation zone reduces as the rarefaction increases. The distance of the stagnation zone is about 0.25 m from the rear end of the re-entry body at 80 km, while there is no clear recirculation zone in the flow at 100 km. The streamlines at 100 km look similar to potential flow streamlines. This is due to high degree of rarefaction in the flow at 100 km. Similar observations have been made in DSMC studies of rarefied flows in L shaped channel and lid driven cavity problems.

Air flow analysis is an extension of the investigations carried out for pure Nitrogen and Oxygen flows over an infinite cylinder detailed in the previous sections. It is obvious that the observations made for the Nitrogen and Oxygen flows are also valid in the present case of re-entry air flows. Figures 6.20 a), b) and c) show the contour plots of translational temperature in the domain predicted by the DSMC simulations with the two model at 68 km, 80 km and 100 km respectively. It is to be noted that the translational temperatures predicted by the DSMC simulations with the TCE model are lower compared to those calculated by the DSMC simulation with the ab-initio chemical reaction model. This is because of the difference in the degree of dissociation and exchange reactions. These differences are noticeable in Figure 6.21 that shows the variation of the total density as well as the density of each individual species along the centreline from the inlet of the domain to the stagnation point on the re-entry surface. Figures 6.21 a), c) and e) are centreline density plots for DSMC simulations with the TCE model at 68 km, 80 km and 100 km respectively whereas Figures 6.21 b), d) and f) show density plots for DSMC simulations with the ab-initio chemical reaction model.

The difference in the flow field temperatures and densities can be explained in the following manner. The composition of air is predominantly molecular Nitrogen which has a mole fraction in excess of 0.72 at all three altitudes. As a result, the nitrogen dissociation becomes the most influential reaction in air chemistry. It was found in the previous discussion on pure nitrogen flow over an infinite cylinder that at re-entry speeds of 10000 m/s, there is a significant difference in the degree of dissociation as predicted by the two models, which in turn results in a difference in the mole fraction of molecular and atomic nitrogen. For the ab-initio model, there is lesser dissociation resulting in higher temperature. The principle reason for the difference in the predictions is the difference in the shape of the dissociation cross-sections of Nitrogen molecules with respect to the relative translational energy as calculated by the two chemical reaction models. The TCE

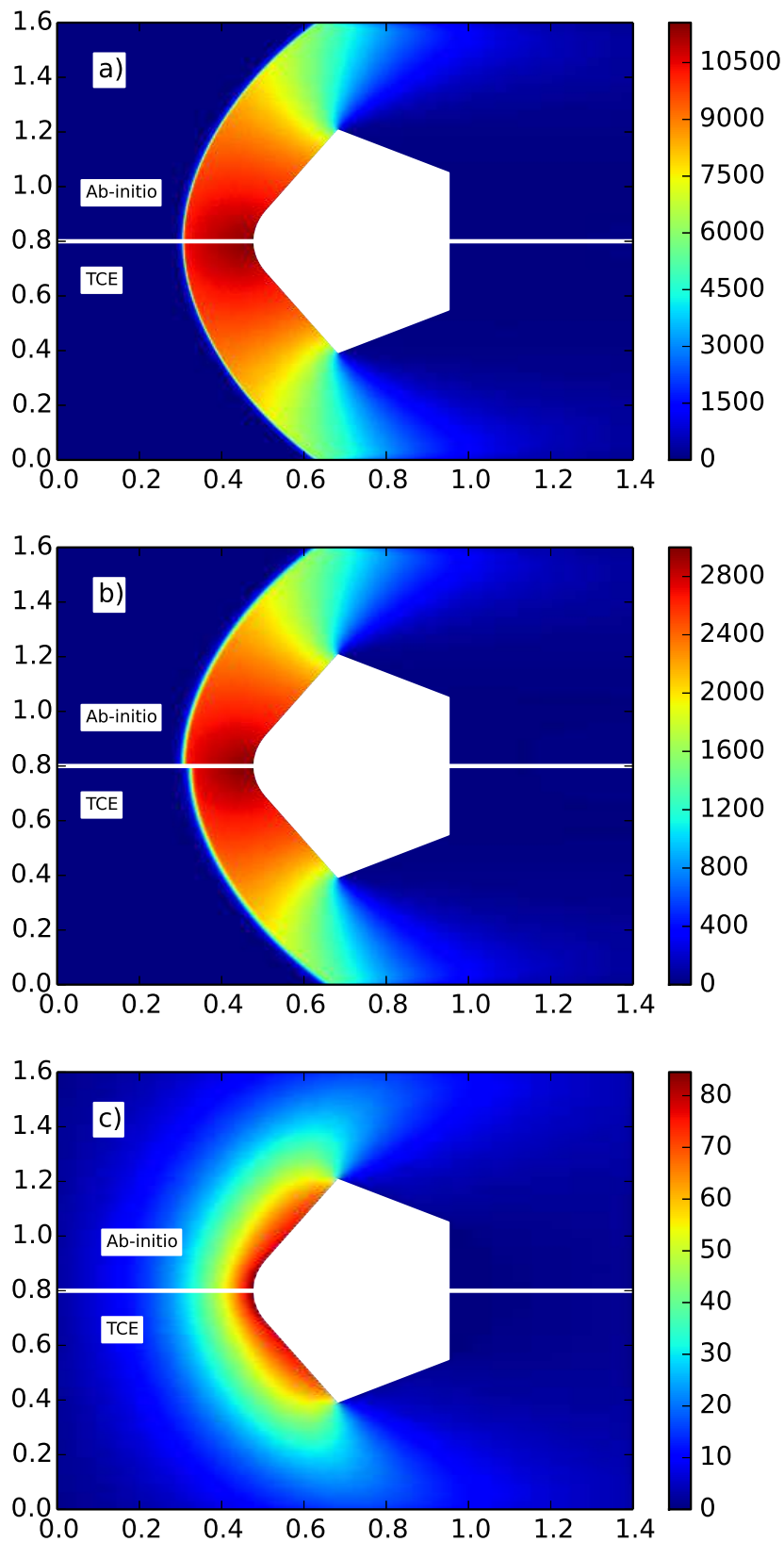


Figure 6.17: Comparison of contour plots of Pressure at a) 68 km, b) 80km and c) 100 km using DSMC simulations employing TCE and Ab-initio chemical model

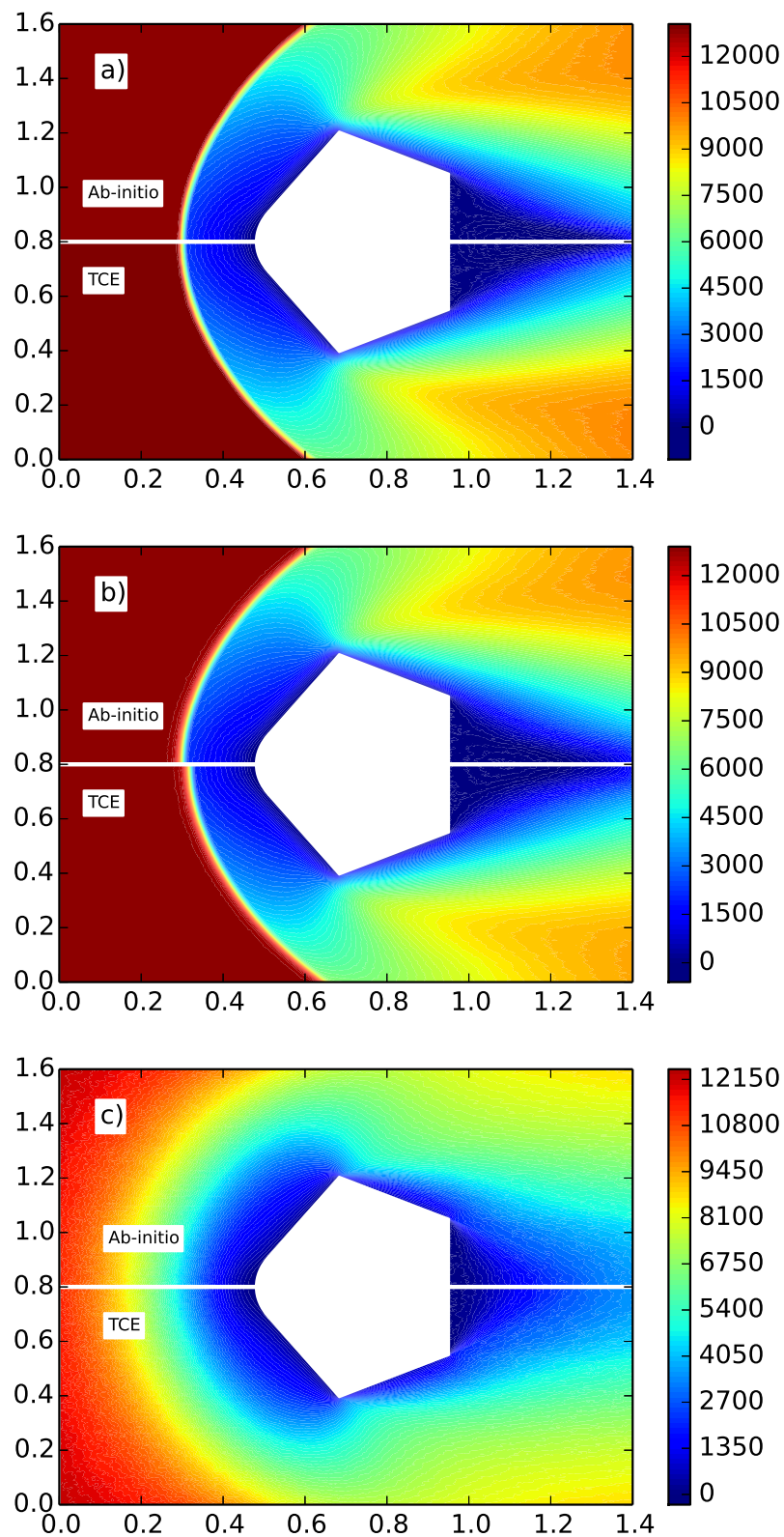


Figure 6.18: Comparison of contour plots of U component of Velocity at a) 68 km, b) 80km and c) 100 km using DSMC simulations employing TCE and Ab-initio chemical model

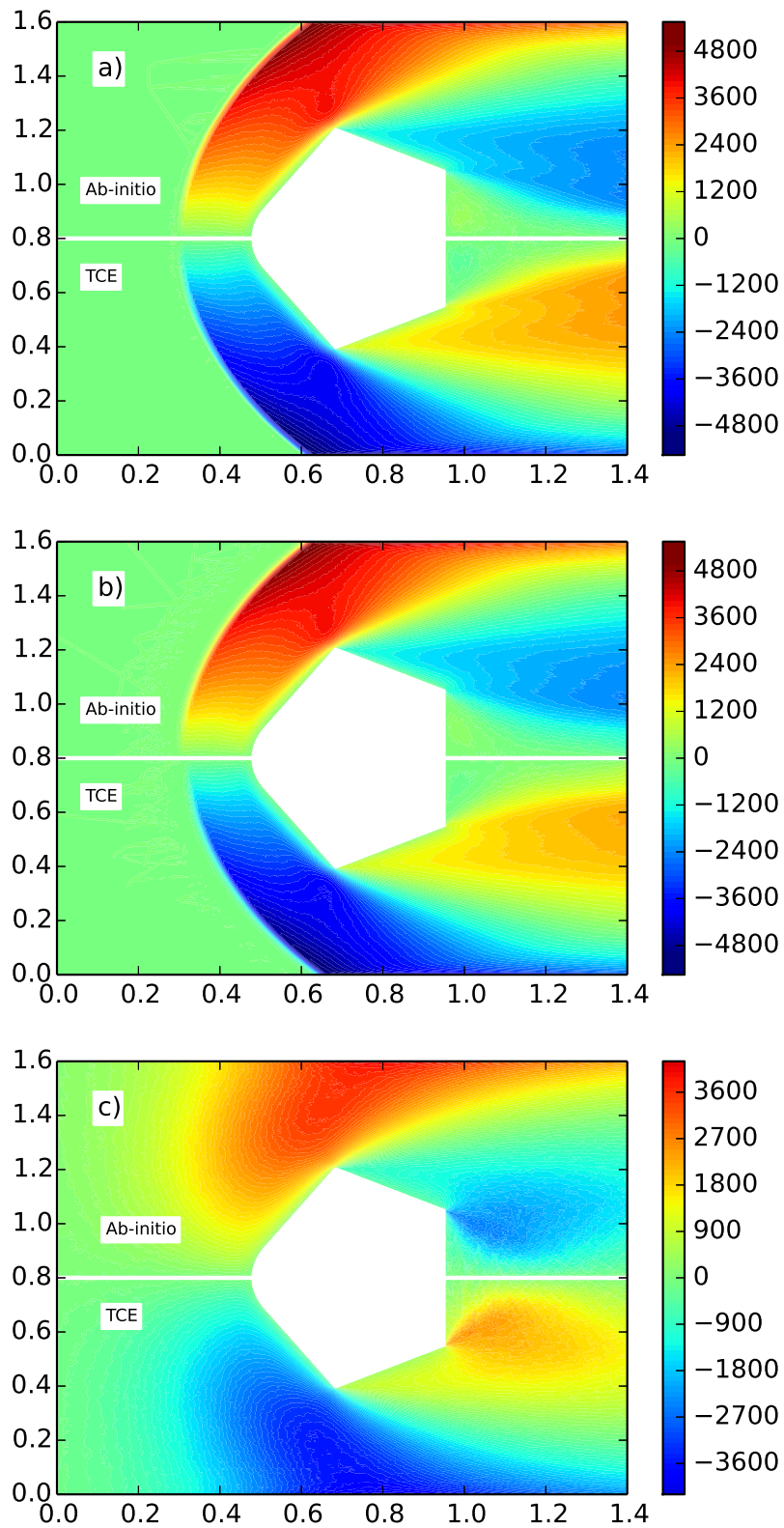


Figure 6.19: Comparison of contour plots of V component of Velocity at a) 68 km, b) 80km and c) 100 km using DSMC simulations employing TCE and Ab-initio chemical model

model predicts a higher value of dissociation cross-sections at a lower ro-vibrational level compared to the dissociation cross-section calculated using the ab-initio chemical reaction model. The same argument is applicable here also. One of the deductions from the study on the Oxygen dissociation chemistry was that at very high re-entry speeds, the molecular oxygen undergoes complete dissociation in the vicinity of the stagnation point. This was predicted by both the chemical reaction models. In the present air flow simulations as well, it is found that oxygen undergoes complete dissociation and the densities of molecular and atomic oxygen predicted by the two chemical reaction models at all three altitudes superimpose.

Although the DSMC simulations with the TCE chemical reaction model predict lower flow field temperatures compared to those predicted by simulations with the ab-initio chemical reaction model, there are other subtle observations to be made. The difference in the temperature values in the flow obtained by the two chemical reaction models is most striking for the simulations at 80 km. The maximum translational temperature in the flow field is around 54200 K and 56700 K for the TCE and ab-initio chemical reaction models respectively. The maximum temperature is located in the shock front for both the cases. In contrast, the difference in the temperatures predicted by the two models at the other two altitudes is less noticeable. The ambient conditions at 80 km corresponds to transition flow regime. The ambient conditions at the other two altitudes correspond to contrasting flow regimes: near continuum flow at 68 km and near free molecular flow at 100 km. The reasons for closer agreement of temperatures predicted by the chemical reaction models are also contrasting. In the case of flows at 100 km, the collision frequency is low and the flow is almost collision-less in nature. At standard temperature and pressure, the collision frequency is $7.3 \times 10^9 \text{ s}^{-1}$. In comparison, the collision frequency at the ambient conditions at 100 km is only $2.1 \times 10^3 \text{ s}^{-1}$. The low collision frequency at 100 km results in a highly diffused shock front. As the number of collisions occurring are few, the number of collisions resulting in a reaction are fewer. In the DSMC simulation at 100 km with the TCE model, the fraction of reacting collisions is relatively higher compared to the DSMC simulation with the ab-initio chemical reaction model. However, as the absolute number of collisions occurring is small, the effect of the chemical reaction model is inconsequential. As a matter of fact, the flow field predicted by DSMC simulation without including any chemical reaction model is also in close agreement with the flow fields predicted by the DSMC simulation with the two chemical reaction models.

In contrast to flow at 100 km, the flow at 68 km is closer to continuum conditions. The distribution of velocities in the post-shock region in this case is closer to the Maxwell-Boltzmann distribution than the distribution of velocities in the post-shock regions of re-entry flows at 80 km or 100 km altitude. In the previous chapter, it was shown that

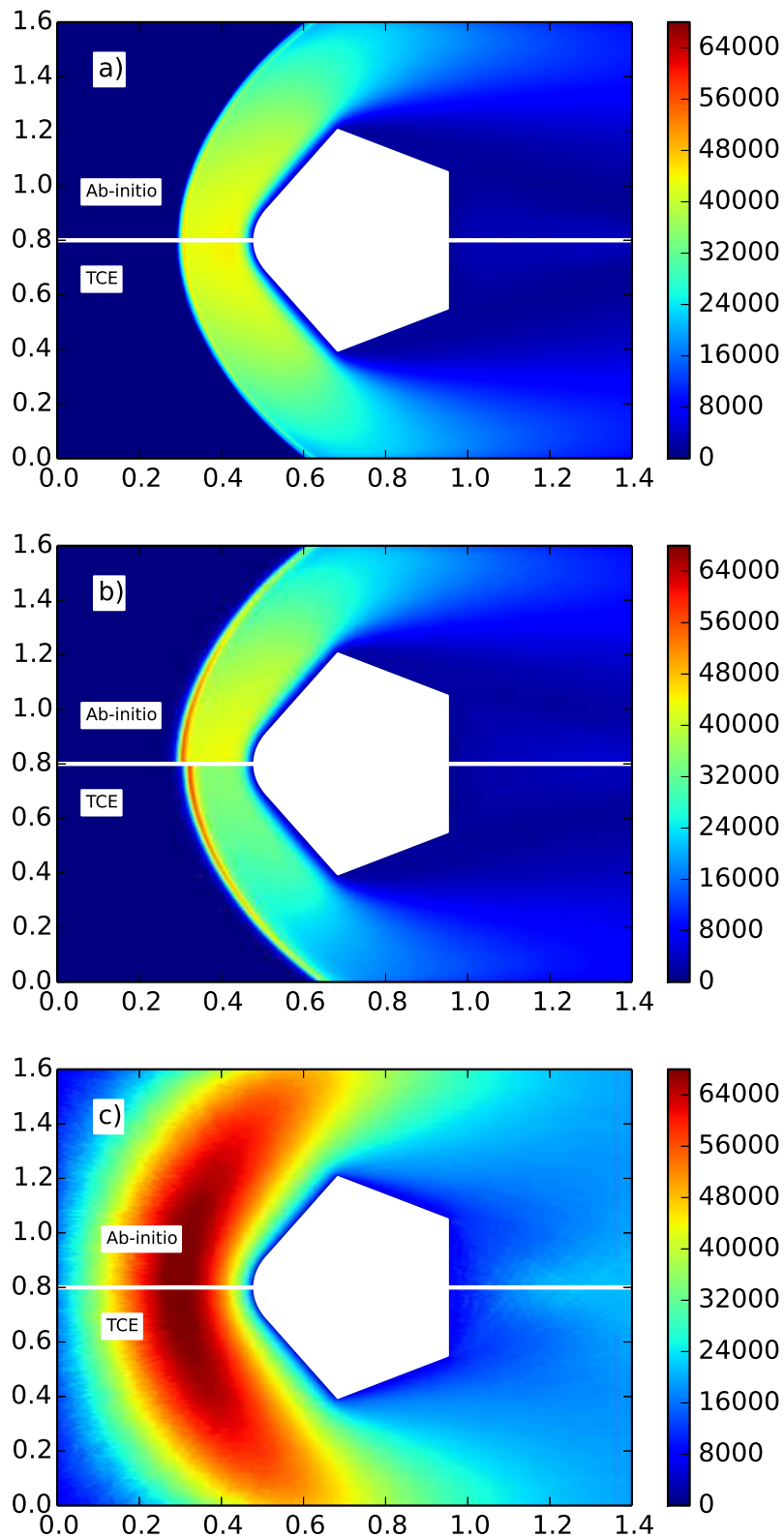


Figure 6.20: Comparison of contour plots of Translational Temperature at a) 68 km, b) 80km and c) 100 km using DSMC simulations employing TCE and Ab-initio chemical model

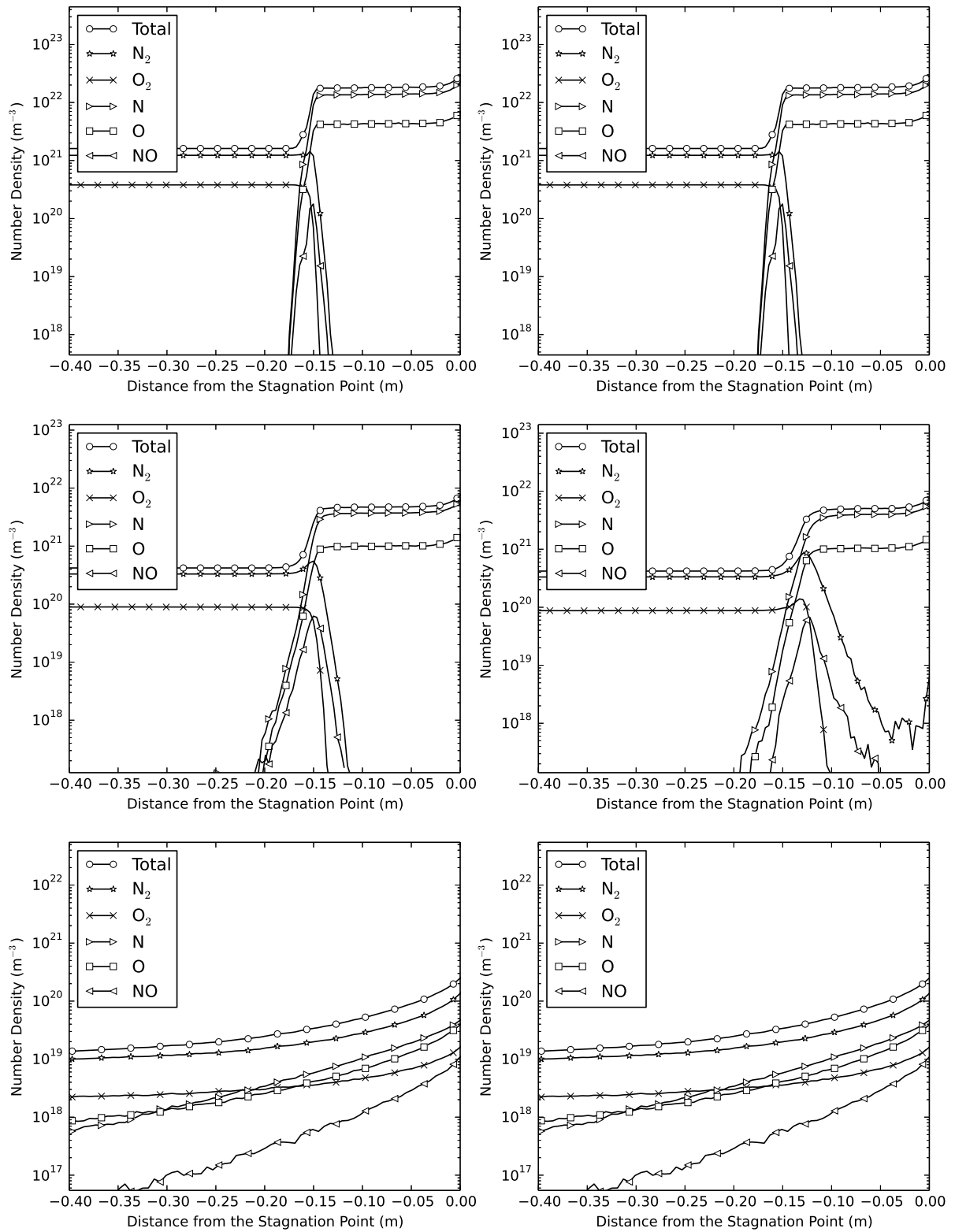


Figure 6.21: Comparison of line plots of Densities for DSMC simulations employing TCE (Sub figures a), c) and e) for altitudes at 68 km, 80km and 100 km respectively) and Ab-initio chemical model (Sub figures b), d) and f) for altitudes at 68 km, 80km and 100 km respectively)

the reaction rate coefficients calculated using the ab-initio cross-sections are in excellent agreement with the available experimental data. This is also true for TCE cross-sections since they are derived as a fit using the equilibrium data. Hence under equilibrium conditions, both models predict the same reaction rates, a fact already demonstrated using the 0-D simulations at the beginning of this chapter. These observations can be extended to justify the flow field results at 68 km where the conditions conform to equilibrium conditions. Hence, the difference in the flow field predicted by the DSMC simulation employing the two chemical reaction models decreases as compared to that at 80 km. It is noteworthy that the differences in the temperature field is lesser at 68 km and 100 km as compared to the differences at 80 km. It can be concluded that modelling reactions using the TCE model is more justified at altitudes 68 km and lower. At 100 km, a nearly similar recommendation can be made for entirely different reasons: that the collisions are far too less to cause reactions. It has to be further cautioned that this statement is only valid for very high re-entry speeds only. At lower re-entry speeds, the difference in the flow fields at any altitude above 60 km calculated using the two chemical reaction models may result in significant disagreement.

Decrease in the degree of reaction leads to increase in the temperatures and the surface heat flux on the vehicle surface. Figure 6.22 shows the variation of surface heat flux along the vehicle surface with zero point on the x-axis representing the stagnation point. As the difference in the reaction rates and temperatures predicted using the DSMC simulations by the two chemical reaction models is significant at 80 km, the difference in surface heat flux is also prominent at this altitude. The TCE chemical reaction model understates the surface heat flux values. As stated earlier, it is obvious that the ab-initio chemical reaction model is more reliable than the phenomenological models. Hence, it is recommended that DSMC simulations with the ab-initio chemical reaction model be used for calculating heat flux on the surface used in designing the TPS.

Nitrogen and Oxygen dissociation have the maximum influence on air chemistry and in turn on the convective portion of the surface heat flux. It is apparent from the density plots that the quantity of NO in the flow is negligible when compared to the contribution of the remaining constituents of air. The ambient atmosphere does not contain any NO. In the shock region, high energy collisions among the molecular Nitrogen and Oxygen leads to dissociation and formation of nascent Nitrogen and Oxygen. These atomic Nitrogen and Oxygen can further collide with other Oxygen and Nitrogen molecules respectively. A fraction of these collisions result in exchange reactions which lead to formation of NO. In the post-shock region, newly formed NO species collide with atomic Nitrogen and Oxygen and further result in backward exchange reaction and depletion of NO. In addition to this, the energy in the post shock region is sufficiently high for the NO molecule to dissociate.

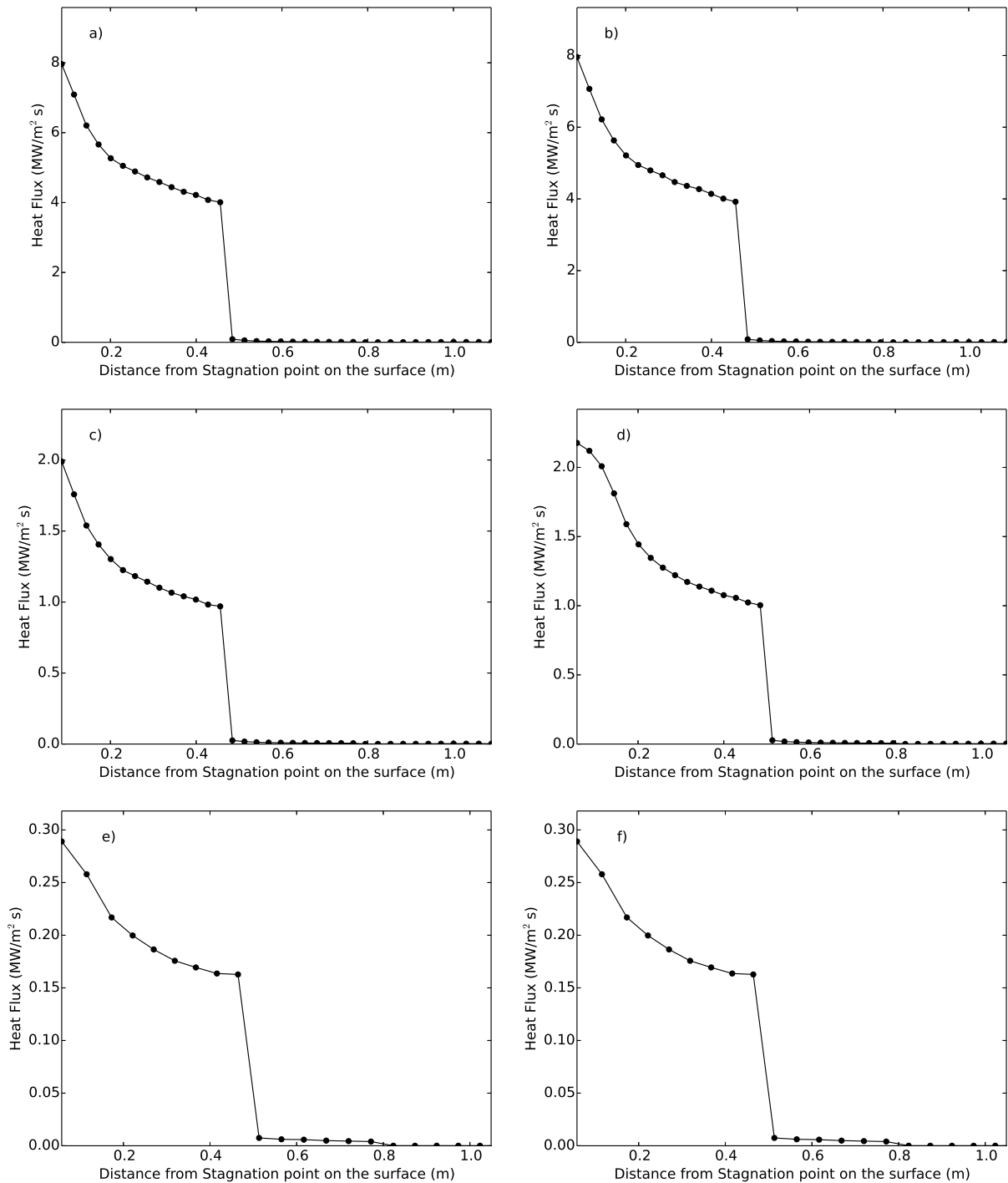


Figure 6.22: Comparison of Surface heat flux along the surface for DSMC simulations employing TCE (Sub figures a), c) and e) for altitudes at 68 km, 80km and 100 km respectively) and Ab-initio chemical model (Sub figures b), d) and f) for altitudes at 68 km, 80km and 100 km respectively)

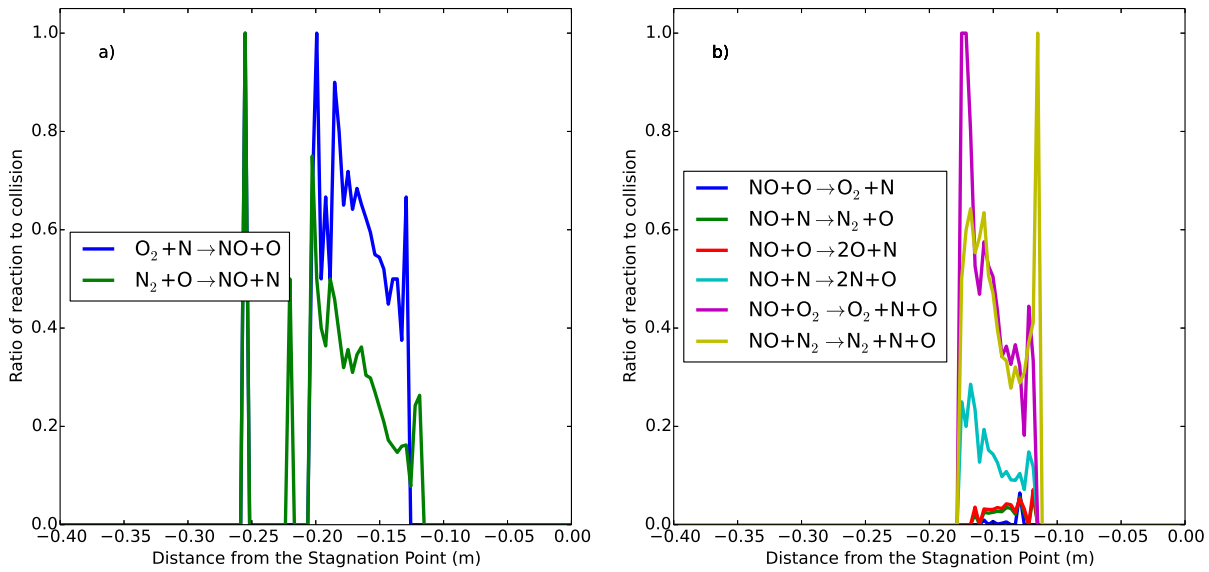


Figure 6.23: Line plots of variation of fraction of collisions leading to reactions along the centreline for a) production of NO b) consumption of NO.

This also leads to the rapid consumption of NO. Hence, the maximum concentration of NO is confined to the thin shock front.

Figure 6.23 a) shows the centreline plot of fraction of reacting collisions to total collisions for different reactions responsible for production of NO. Similarly Figure 6.23 b) shows the plots for consumption of NO. The forward exchange reactions account for production for NO. Oxygen having lower dissociation enthalpy starts to dissociate at the anterior of the shock front. This leads to availability of nascent Oxygen which upon collision with molecular Nitrogen can lead to NO production. In contrast, the Nitrogen dissociation initiates in the downstream towards the posterior of the shock front. It is evident from Figure 6.23 a) that the production of NO through $N+O_2 \rightarrow NO+O$ exchange reaction is more prominent at the start of the shock front whereas the production through $O+N_2 \rightarrow NO+N$ exchange reaction is more prominent at the end. Figure 6.23 b) shows that the depletion of NO is dominated by dissociation upon colliding with molecular Nitrogen and Oxygen in comparison with the reverse Zeldovich reactions and dissociation with atomic Nitrogen and Oxygen. In the case of flow at 100 km, as explained in the earlier section, the number of collisions occurring is fewer leading to lesser consumption rate of NO in the post-shock region. In addition to the convective component of the heat flux, radiative heat transfer becomes vital at higher altitudes. NO has a significant role in radiative heat transfer. Hence it is crucial that the exchange reactions are also properly modelled. The amount of NO formed in the shock front predicted by the ab-initio based chemical model is greater than that predicted by the TCE model, especially at 80 km (Figure 6.21). This difference is again because of the difference in the exchange

cross-sections predicted by the two models. This will lead to a difference in the amount of radiative heat flux on the re-entry surface. Although the amount of NO is negligible in comparison to the other air species, it is recommended that the ab-initio chemical reaction model be preferred over the TCE model.

6.5 Summary

An ab-initio based chemical model for Direct Simulation Monte Carlo algorithm is formulated that uses the ab-initio based CID cross-section data. It is found that the new model provides an excellent estimate of the degree of dissociation as a function of temperature at equilibrium conditions in addition to the correct match of equilibrium reaction rates. In non-equilibrium situations, DSMC simulations with these cross-sections predict a clear difference with the predictions from the simulations that use the TCE model. This highlights the need and the utility of a more theoretically accurate model than the phenomenological models generally used in DSMC to study hypersonic flows.

Chapter 7

Summary and Future Work

7.1 Summary and Key Contributions

A brief summary of the present work is presented here. The most important contribution from this work is the development of an ab-initio cross-section database for air chemistry. All important dissociation reactions in air chemistry have been studied extensively. The procedure for development of a CID cross-section database as a function of relative translational energy and ro-vibrational levels of the interacting particles is described. Global potential energy surfaces are used to calculate the reaction probability and the CID cross-section by employing the Quasi-Classical Trajectory method. A key contribution is the formulation of a fitting procedure that calculates the CID cross-section for the entire range of ro-vibrational combinations using a selected set of CID cross-section data and spectroscopic data. The reaction rate calculated using this cross-section matches well with available experimental data under equilibrium conditions for all reactions.

An ab-initio based chemical model for Direct Simulation Monte Carlo algorithm is formulated that uses the ab-initio based CID cross-section data. It is found that the proposed model gives a good estimate of the degree of dissociation as a function of temperature at equilibrium conditions in addition to the correct match of equilibrium reaction rates. In non-equilibrium situations, DSMC simulations with these cross-sections predict reaction rates and mole fractions that are clearly different from the predictions obtained from the simulations that use the TCE model. This highlights the need for a more theoretically accurate model that can replace the phenomenological models presently used in DSMC to study hypersonic flows.

Thus, the key contributions from the present work are as follows:

- A 3D parallel Direct Simulation Monte Carlo (DSMC) code is developed and the existing elastic and inelastic collision models as well as the phenomenological chemical

reaction models are implemented.

- A new ab-initio chemical reaction model based on a stronger theoretical understanding is reported. This model is free from parameters based on phenomenological assumption making it superior for simulating flows having a high degree of non-equilibrium.
- The ab-initio model employs highly accurate Potential Energy Surfaces (PES). New PESs for N_3 , O_3 , N_4 and O_4 systems are constructed and published from scratch using the MolCAS computational chemistry software. PESs for the remaining systems (N_4 , N_2O_2 , N_2O , NO_2) are available in the literature.
- A parallel Quasi-Classical Trajectory (QCT) code is developed that simulates the interaction between the reactants at the molecular level using PESs. A large number of simulations are sampled using this QCT code and a reactive cross-section database is calculated for the entire ro-vibrational spectrum for important reactions in the five species air chemistry model. The reaction cross-section databases are then utilized in the ab-initio based chemical reaction model in the DSMC algorithm.

7.2 Future Work

On further scrutiny of the present work, it is clear that questions can be raised on the fact that an accurate chemical reaction model is being used for the reactions, while phenomenological models are still being used for simulating elastic and inelastic collisions. The present work opens up the possibility for improving the models for such processes that can be developed on similar principles as the new chemical reaction model.

- The present collision models, such as the Variable Hard Sphere (VHS) and Variable Soft Sphere (VSS) models, assume an analytical expression for the total collision cross-section as a function of relative translational speed. These models generally employ various parameters such as the reference VHS parameter and reference temperature. The value of the VHS parameter at the reference temperature is calculated in a way that the viscosity calculated using the assumed total collision cross-section matches with the experimental value of viscosity at the particular reference temperature. This is appropriate for DSMC simulations in near isothermal cases. It is apparent that the viscosity-temperature relation calculated using such cross-section models do not match with the corresponding experimental relation over a wide range of temperature. In contrast, the total cross-section database calculated using the present methodology (using the QCT method on ab-initio developed PESs) is a suitable alternative that is expected to resolve the question of

viscosity-temperature relation over the entire range of temperature. Additionally, the total collision cross-section databases calculated using the QCT procedure can be used to predict viscosity-temperature relations of new materials where experimental data are not available.

- The Larsen-Borgnakke model is widely used to simulate inelastic energy exchange in DSMC. The parameters used in the LB model utilize the values of macroscopic quantities such as the translational temperature, pressure and number density. In the case of flows with high degree of non-equilibrium, the definition and significance of temperature is questionable and the value of temperature is a mere statistical quantity. Although the LB model handles inelastic collisions reasonable well in most cases, it is not appropriate to use this model in case of flows with high degree of non-equilibrium. State-to-state inelastic cross-sections using the QCT method though computationally expensive are certainly a better alternative to the LB model. The generation of such a database will require ingenuity in addition to large computational resources.
- Presently, models similar to the Total Collision Energy (TCE) model are employed to simulate ionization reactions. The work done for generating the present set of databases can be extended to include such ionization reactions. However, the calculation of the Potential Energy Surfaces in the case of ionization reactions will require appreciable effort.
- Several phenomenological models are used to handle thermal and chemical ablation of the surface material installed on the Thermal Protection System of a re-entry vehicle. Studying these complex phenomena at molecular level was not feasible in the past due to limited computational resources. However, in the present day this is possible. This is yet another example of a problem that can be considered for modelling based on first principles.

Additionally, the future space missions will require similar cross-section databases for designing vehicles re-entering atmospheres of other astronomical objects such as Martian and Venusian atmospheres. The reactive cross-section databases generated have applications in simulation techniques other than DSMC. An exact chemical reaction model employing the cross-section database, on suitable modification, can be introduced in several other methods such as the Navier-Stokes and higher order Boltzmann based Computational Fluid Dynamics algorithms. The above mentioned problems are an extension to

the Ph.D. work and also complex standalone assignments that need to be undertaken as a future work.

Bibliography

- [1] C. Park, *Nonequilibrium Hypersonic Aerothermodynamics*, Wiley, 1990.
- [2] G. A. Bird, *Molecular gas dynamics and the direct simulation of gas flows*, Clarendon, 1994.
- [3] G. Bird, *The DSMC method*, CreateSpace Independent Publishing Platform, 2013.
- [4] G. Bird, The velocity distribution function within a shock wave, *Journal of Fluid Mechanics*, 30(3):479–487, 1967.
- [5] G. Bird, Direct simulation and the Boltzmann equation, *Physics of Fluids (1958-1988)*, 13(11):2676–2681, 1970.
- [6] G. Bird, Monte Carlo simulation of gas flows, *Annual Review of Fluid Mechanics*, 10(1):11–31, 1978.
- [7] G. Bird, *Perception of Numerical Methods in Rarefied Gasdynamics*, pages 211–226, Progress in Astronautics and Aeronautics. American Institute of Aeronautics and Astronautics, Jan 1989, 0.
- [8] G. Bird, Recent advances and current challenges for DSMC, *Computers & Mathematics with Applications*, 35(1):1–14, 1998.
- [9] G. A. Bird, The QK model for gas phase chemical reaction rates, *Physics of Fluids*, 23(10), 2011.
- [10] A. Gavasane, A. Agrawal, A. M. Pradeep, and U. Bhandarkar, Simulation of a temperature drop for the flow of rarefied gases in microchannels, *Numerical Heat Transfer, Part A: Applications*, 71(10):1066–1079, 2017.
- [11] K. Koura, Transient Couette flow of rarefied binary gas mixtures, *The Physics of Fluids*, 13(6):1457–1466, 1970.
- [12] M. Ivanov and S. Rogasinsky, Analysis of numerical techniques of the direct simulation Monte Carlo method in the rarefied gas dynamics, *Russian Journal of numerical analysis and mathematical modelling*, 3(6):453–466, 1988.

- [13] M. Ivanov, S. Gimelshein, and G. Markelov, Statistical simulation of the transition between regular and Mach reflection in steady flows, *Computers & Mathematics with Applications*, 35(1):113–125, 1998.
- [14] H. Matsumoto and K. Koura, Comparison of velocity distribution functions in an argon shock wave between experiments and Monte Carlo calculations for Lennard-Jones potential, *Physics of Fluids A: Fluid Dynamics*, 3(12):3038–3045, 1991.
- [15] K. Koura and H. Matsumoto, Variable soft sphere molecular model for inverse-power-law or Lennard-Jones potential, *Physics of Fluids A: Fluid Dynamics*, 3(10):2459–2465, 1991.
- [16] H. A. Hassan and D. B. Hash, A generalized hard-sphere model for Monte Carlo simulation, *Physics of Fluids A: Fluid Dynamics*, 5(3):738–744, 1993.
- [17] J. Fan, A generalized soft-sphere model for Monte Carlo simulation, *Physics of Fluids*, 14(12):4399–4405, 2002.
- [18] C. Borgnakke and P. S. Larsen, Statistical collision model for Monte Carlo simulation of polyatomic gas mixture, *Journal of computational Physics*, 18(4):405–420, 1975.
- [19] B. L. Haas, D. B. Hash, G. A. Bird, F. E. Lumpkin, and H. A. Hassan, Rates of thermal relaxation in direct simulation Monte Carlo methods, *Physics of Fluids*, 6(6):2191–2201, 1994.
- [20] J. Parker, Rotational and vibrational relaxation in diatomic gases, *The Physics of Fluids*, 2(4):449–462, 1959.
- [21] J. A. Lordi and R. E. Mates, Rotational relaxation in nonpolar diatomic gases, *The Physics of Fluids*, 13(2):291–308, 1970.
- [22] B. L. Haas and I. D. Boyd, Models for direct Monte Carlo simulation of coupled vibration-dissociation, *Physics of Fluids A: Fluid Dynamics*, 5(2):478–489, 1993.
- [23] M. Karplus, R. N. Porter, and R. D. Sharma, Exchange Reactions with Activation Energy. I. Simple Barrier Potential for (H, H₂), *The Journal of Chemical Physics*, 43(9):3259–3287, 1965.
- [24] D. G. Truhlar and J. T. Muckerman, *Reactive Scattering Cross Sections III: Quasiclassical and Semiclassical Methods*, pages 505–566, Springer US, Boston, MA, 1979.
- [25] P. Pulay, A perspective on the CASPT2 method, *International Journal of Quantum Chemistry*, 111(13):3273–3279, 2011.

- [26] T. Ozawa, D. A. Fedosov, and D. A. Levin, Modeling of OH Product Distributions Using QCT-MD and BL Models in a Bow Shock, In M. Capitelli, editor, *Rarefied Gas Dynamics: 24th International Symposium on Rarefied Gas Dynamics*, volume 762 of *American Institute of Physics Conference Series*, pages 902–907, May 2005.
- [27] T. Ozawa, D. A. Levin, and I. J. Wysong, Chemical reaction modeling for hypervelocity collisions between O and HCl, *Physics of Fluids*, 19(5), 2007.
- [28] B. Ramachandran and K. A. Peterson, Potential energy surfaces for the $\hat{3}A''$ and $\hat{3}A'$ electronic states of the $O(^3P) + HCl$ system, *Journal of Chemical Physics*, 119(18):9590–9600, 2003.
- [29] I. Wysong, S. Gimelshein, N. Gimelshein, W. McKeon, and F. Esposito, Reaction cross sections for two direct simulation Monte Carlo models: Accuracy and sensitivity analysis, *Physics of Fluids*, 24(4):042002, 2012.
- [30] P. Valentini, P. Norman, C. Zhang, and T. E. Schwartzentruber, Rovibrational coupling in molecular nitrogen at high temperature: An atomic-level study, *Physics of Fluids*, 26(5):056103, 2014.
- [31] P. Valentini, T. E. Schwartzentruber, J. D. Bender, I. Nompelis, and G. V. Candler, Direct simulation of rovibrational excitation and dissociation in molecular nitrogen using an ab initio potential energy surface, *AIAA Paper*, 474:2015, 2015.
- [32] P. Valentini, T. E. Schwartzentruber, J. D. Bender, and G. V. Candler, Direct molecular simulation of hightemperature nitrogen dissociation due to both NN 2 and N₂-N₂ collisions, *AIAA Aviation*, pages 22–26, 2015.
- [33] J. D. Bender, P. Valentini, I. Nompelis, Y. Paukku, Z. Varga, D. G. Truhlar, T. Schwartzentruber, and G. V. Candler, An improved potential energy surface and multi-temperature quasiclassical trajectory calculations of N₂ + N₂ dissociation reactions, *The Journal of Chemical Physics*, 143(5):054304, 2015.
- [34] D. A. Andrienko and I. D. Boyd, Rovibrational energy transfer and dissociation in O₂-O collisions, *The Journal of Chemical Physics*, 144(10), 2016.
- [35] M. Tashiro and R. Schinke, The effect of spin-orbit coupling in complex forming O(P-3)+ O-2 collisions, *Journal of Chemical Physics*, 119(19):10186–10193, 2003.
- [36] E. E. Nikitin, *Theory of Elementary Atomic and Molecular Processes in Gases*, Clarendon, 1994.

- [37] A. Varandas and A. Pais, A realistic double many-body expansion (DMBE) potential energy surface for ground-state O_3 from a multiproperty fit to ab initio calculations, and to experimental spectroscopic, inelastic scattering, and kinetic isotope thermal rate data, *Molecular Physics*, 65(4):843–860, 1988.
- [38] F. Esposito and M. Capitelli, Quasiclassical trajectory calculations of vibrationally specific dissociation cross-sections and rate constants for the reaction $O + O_2(v) \rightarrow 3O$, *Chemical physics letters*, 364(1):180–187, 2002.
- [39] F. Esposito and M. Capitelli, The relaxation of vibrationally excited O_2 molecules by atomic oxygen, *Chemical physics letters*, 443(4):222–226, 2007.
- [40] F. Esposito, I. Armenise, G. Capitta, and M. Capitelli, $O-O_2$ state-to-state vibrational relaxation and dissociation rates based on quasiclassical calculations, *Chemical Physics*, 351(1), 2008.
- [41] M. Kulakhmetov, M. Gallis, and A. Alexeenko, Ab initio-informed maximum entropy modeling of rovibrational relaxation and state-specific dissociation with application to the $O_2 + O$ system, *The Journal of Chemical Physics*, 144(17), 2016.
- [42] K. Yamashita, K. Morokuma, F. L. Quéré, and C. Leforestier, New ab initio potential surfaces and three-dimensional quantum dynamics for transition state spectroscopy in ozone photodissociation, *Chemical Physics Letters*, 191(6), 1992.
- [43] A. Banichevich, S. D. Peyerimhoff, and F. Grein, Potential energy surfaces of ozone in its ground state and in the lowest-lying eight excited states, *Chemical Physics*, 178(1):155 – 188, 1993.
- [44] T. Müller, S. S. Xantheas, H. Dachsels, R. J. Harrison, J. Nieplocha, R. Shepard, G. S. Kedziora, and H. Lischka, A systematic ab initio investigation of the open and ring structures of ozone, *Chemical Physics Letters*, 293(1-2):72 – 80, 1998.
- [45] D. Xie, H. Guo, and K. A. Peterson, Accurate ab initio near-equilibrium potential energy and dipole moment functions of the ground electronic state of ozone, *The Journal of Chemical Physics*, 112(19):8378–8386, 2000.
- [46] D. W. Arnold, C. Xu, E. H. Kim, and D. M. Neumark, Study of low lying electronic states of ozone by anion photoelectron spectroscopy of O_3 , *The Journal of Chemical Physics*, 101(2):912–922, 1994.
- [47] R. Siebert, P. Fleurat-Lessard, R. Schinke, M. Bittererová, and S. C. Farantos, The vibrational energies of ozone up to the dissociation threshold: Dynamics calculations on an accurate potential energy surface, *The Journal of Chemical Physics*, 116(22):9749–9767, 2002.

- [48] D. Babikov, B. K. Kendrick, R. B. Walker, R. T. Pack, P. Fleurat-Lesard, and R. Schinke, Metastable states of ozone calculated on an accurate potential energy surface, *The Journal of Chemical Physics*, 118(14):6298–6308, 2003.
- [49] V. G. Tyuterev, R. V. Kochanov, S. A. Tashkun, F. Holka, and P. G. Szalay, New analytical model for the ozone electronic ground state potential surface and accurate ab initio vibrational predictions at high energy range, *The Journal of Chemical Physics*, 139(13):134307, 2013.
- [50] M. Ayouz and D. Babikov, Global permutationally invariant potential energy surface for ozone forming reaction, *The Journal of Chemical Physics*, 138(16):164311, 2013.
- [51] R. Dawes, P. Lolur, J. Ma, and H. Guo, Communication: Highly accurate ozone formation potential and implications for kinetics, *The Journal of Chemical Physics*, 135(8):081102, 2011.
- [52] R. Dawes, P. Lolur, A. Li, B. Jiang, and H. Guo, Communication: An accurate global potential energy surface for the ground electronic state of ozone, *The Journal of Chemical Physics*, 139(20):201103, 2013.
- [53] P. J. Hay and T. H. D. Jr, Geometries and energies of the excited states of O_3 from ab initio potential energy surfaces, *The Journal of Chemical Physics*, 67(5):2290–2303, 1977.
- [54] F. Esposito and M. Capitelli, Quasiclassical molecular dynamic calculations of vibrationally and rotationally state selected dissociation cross-sections: $N + N_2(v, j) \rightarrow 3N$, *Chemical physics letters*, 302(1):49–54, 1999.
- [55] F. Esposito, M. Capitelli, and C. Gorse, Quasi-classical dynamics and vibrational kinetics of $N + N_2(v)$ system, *Chemical Physics*, 257(2):193–202, 2000.
- [56] F. Esposito, I. Armenise, and M. Capitelli, $N-N_2$ state to state vibrational-relaxation and dissociation rates based on quasiclassical calculations, *Chemical Physics*, 331(1):1–8, 2006.
- [57] E. Garcia, A. Saracibar, S. Gomez-Carrasco, and A. Lagana, Modeling the global potential energy surface of the $N + N_2$ reaction from ab initio data, *Physical Chemistry Chemical Physics*, 10(18):2552–2558, 2008.
- [58] A. Lagana, E. Garcia, and L. Ciccarelli, Deactivation of vibrationally excited nitrogen molecules by collision with nitrogen atoms, *Journal of Physical Chemistry*, 91(2):312–314, 1987.

- [59] C. Petrongolo, MRD-CI quartet potential surfaces for the collinear reactions $N(^4S_u)+N_2(X^1\Sigma_{g^+}, A^3\Sigma_{u^+}, \text{ and } B^3\Pi_g)$, *Journal of Molecular Structure: THEOCHEM*, 202:135 – 142, 1989.
- [60] D. Wang, J. R. Stallcop, W. M. Huo, C. E. Dateo, D. W. Schwenke, and H. Partridge, Quantal study of the exchange reaction for $N+N_2$ using an ab initio potential energy surface, *The Journal of Chemical Physics*, 118(5):2186–2189, 2003.
- [61] C. F. Jackels and E. R. Davidson, An ab initio potential energy surface study of several electronic states of NO_2 , *The Journal of Chemical Physics*, 65(8):2941–2957, 1976.
- [62] G. Hirsch and R. J. Buenker, Ab initio MRD-CI study of NO_2 . 1. Multi-dimensional potential surfaces for the two lowest $2A'$ states, *Canadian journal of chemistry*, 63(7):1542–1549, 1985.
- [63] G. Hirsch, R. J. Buenker, and C. Petrongolo, Ab initio study of NO_2 : Part II: Non-adiabatic coupling between the two lowest $2A'$ states and the construction of a diabatic representation, *Molecular Physics*, 70(5):835–848, 1990.
- [64] D. Reignier, T. Stoecklin, P. Halvick, A. Voronin, and J. C. Rayez, Analytical global potential energy surfaces of the two lowest $2A'$ states of NO_2 , *Phys. Chem. Chem. Phys.*, 3:2726–2734, 2001.
- [65] S. P. Walch and R. L. Jaffe, Calculated potential surfaces for the reactions: $O+N_2\rightarrow NO+N$ and $N+O_2\rightarrow NO+O$, *The Journal of Chemical Physics*, 86(12):6946–6956, 1987.
- [66] M. Gilibert, A. Aguilar, M. González, and R. Sayós, Quasiclassical trajectory study of the $N(^4S_u) + O_2(X^3\Sigma_g)\rightarrow NO(X^2\Pi) + O(^3P_g)$ atmospheric reaction on the $2A'$ ground potential energy surface employing an analytical Sorbie-Murrell potential, *Chemical Physics*, 172(1):99 – 115, 1993.
- [67] R. Sayós, C. Oliva, and M. González, New analytical ($2A', 4A'$) surfaces and theoretical rate constants for the $N(^4S)+O_2$ reaction, *The Journal of Chemical Physics*, 117(2):670–679, 2002.
- [68] A. J. C. Varandas, A realistic multi-sheeted potential energy surface for $NO_2(2A')$ from the double many-body expansion method and a novel multiple energy-switching scheme, *The Journal of Chemical Physics*, 119(5):2596–2613, 2003.
- [69] V. Kurkal, P. Fleurat-Lessard, and R. Schinke, NO_2 : Global potential energy surfaces of the ground(1^2A_1) and the first excited (1^2B_2) electronic states, *The Journal of Chemical Physics*, 119(3):1489–1501, 2003.

- [70] M. Braunstein and J. W. Duff, Theoretical study of the $\text{N}(2\text{D})+\text{O}_2(\text{X } ^3\Sigma_{g-})\rightarrow\text{O}+\text{NO}$ reaction, *The Journal of Chemical Physics*, 113(17):7406–7413, 2000.
- [71] M. González, I. Miquel, and R. Sayós, Ab initio, variational transition state theory and quasiclassical trajectory study on the lowest $2\text{A}'$ potential energy surface involved in the $\text{N}(^2\text{D})+\text{O}_2(\text{X } ^3\Sigma_g)\rightarrow\text{O}(^3\text{P})+\text{NO}(\text{X } ^2\Pi)$ atmospheric reaction, *The Journal of Chemical Physics*, 115(6):2530–2539, 2001.
- [72] M. Gilibert, A. Aguilar, M. Gonzalez, F. Mota, and R. Sayos, Dynamics of the $\text{N}(^4\text{S}_u) + \text{NO}(\text{X}^2\Pi) \rightarrow \text{N}_2(\text{X}^1\Sigma_g+) + \text{O}(^3\text{P}_g)$ atmospheric reaction on the $3\text{A}'$ ground potential energy surface. I. Analytical potential energy surface and preliminary quasiclassical trajectory calculations, *The Journal of Chemical Physics*, 97(8):5542–5553, 1992.
- [73] P. Gamallo, M. González, and R. Sayós, Ab initio derived analytical fits of the two lowest triplet potential energy surfaces and theoretical rate constants for the $\text{N}(^4\text{S})+\text{NO}(\text{X}^2\Pi)$ system, *The Journal of Chemical Physics*, 119(5):2545–2556, 2003.
- [74] W. Lin, Z. Varga, G. Song, Y. Paukku, and D. G. Truhlar, Global triplet potential energy surfaces for the $\text{N}_2(\text{X}^1\Sigma) + \text{O}(^3\text{P}) \rightarrow \text{NO}(\text{X}^2\Pi) + \text{N}(^4\text{S})$ reaction, *The Journal of Chemical Physics*, 144(2):024309, 2016.
- [75] POTLIB, <http://comp.chem.umn.edu/potlib>.
- [76] D. Lauvergnat and D. C. Clary, Reactive scattering of highly vibrationally excited oxygen molecules: Ozone formation?, *The Journal of Chemical Physics*, 108(9):3566–3573, 1998.
- [77] R. Hernández-Lamoneda and A. Ramirez-Solis, Reactivity and electronic states of O_4 along minimum energy paths, *The Journal of Chemical Physics*, 113(10):4139–4145, 2000.
- [78] A. Varandas and J. Llanio-Trujillo, On triplet tetraoxygen: ab initio study along minimum energy path and global modelling, *Chemical physics letters*, 356(5):585–594, 2002.
- [79] Y. Paukku, K. R. Yang, Z. Varga, G. Song, J. D. Bender, and D. G. Truhlar, Potential energy surfaces of quintet and singlet O_4 , *The Journal of Chemical Physics*, 147(3):034301, 2017.

- [80] R. Hernández-Lamoneda, M. Bartolomei, M. I. Hernández, J. Campos-Martínez, and F. Dayou, Intermolecular Potential of the O_2 - O_2 Dimer. An ab Initio Study and Comparison with Experiment, *The Journal of Physical Chemistry A*, 109(50):11587–11595, 2005, PMID: 16354051.
- [81] M. Bartolomei, E. Carmona-Novillo, M. I. Hernández, J. Campos-Martínez, and R. Hernández-Lamoneda, Accurate ab initio intermolecular potential energy surface for the quintet state of the $O_2(^3\Sigma_{g-})$ - $O_2(^3\Sigma_{g-})$ dimer, *The Journal of Chemical Physics*, 128(21):214304, 2008.
- [82] M. Bartolomei, E. Carmona-Novillo, M. I. Hernández, J. Campos-Martínez, and R. Hernández-Lamoneda, Global ab initio potential energy surfaces for the $O_2(^3\Sigma_{g-})+O_2(^3\Sigma_{g-})$ interaction, *The Journal of Chemical Physics*, 133(12):124311, 2010.
- [83] Y. Paukku, K. R. Yang, Z. Varga, and D. G. Truhlar, Global ab initio ground-state potential energy surface of N_4 , *The Journal of Chemical Physics*, 139(4), 2013.
- [84] Z. Varga, R. Meana-Pañeda, G. Song, Y. Paukku, and D. G. Truhlar, Potential energy surface of triplet N_2O_2 , *The Journal of Chemical Physics*, 144(2), 2016.
- [85] T. K. Mankodi, U. V. Bhandarkar, and B. P. Puranik, Dissociation cross sections for $N_2 + N \rightarrow 3N$ and $O_2 + O \rightarrow 3O$ using the QCT method, *The Journal of Chemical Physics*, 146(20):204307, 2017.
- [86] Z. Varga, Y. Paukku, and D. G. Truhlar, Potential energy surfaces for $O+O_2$ collisions, *The Journal of Chemical Physics*, 147(15):154312, 2017.
- [87] T. K. Mankodi, U. V. Bhandarkar, and B. P. Puranik, Global potential energy surface of ground state singlet spin O_4 , *The Journal of Chemical Physics*, 148(7):074305, 2018.
- [88] Y. Paukku, Z. Varga, and D. G. Truhlar, Potential energy surface of triplet O_4 , *The Journal of Chemical Physics*, 148(12):124314, 2018.
- [89] D. J. Griffiths, *Introduction to quantum mechanics*, Pearson Education India, 2005.
- [90] J. D. Bender, I. Nompelis, P. Valentini, S. Doraiswamy, T. Schwartzentruber, G. V. Candler, Y. Paukku, K. R. Yang, Z. Varga, and D. G. Truhlar, Quasiclassical Trajectory Analysis of the $N_2 + N_2$ Reaction Using a New Ab Initio Potential Energy Surface, *11th AIAA/ASME Joint Thermophysics and Heat Transfer Conference*, 2014.

- [91] L. Bytautas, N. Matsunaga, and K. Ruedenberg, Accurate ab initio potential energy curve of O₂. II. Core-valence correlations, relativistic contributions, and vibration-rotation spectrum, *The Journal of Chemical Physics*, 132(7), 2010.
- [92] W. C. Swope, H. C. Andersen, P. H. Berens, and K. R. Wilson, A computer simulation method for the calculation of equilibrium constants for the formation of physical clusters of molecules: Application to small water clusters, *The Journal of Chemical Physics*, 76(1):637–649, 1982.
- [93] G. Karlström, R. Lindh, P. Åke Malmqvist, B. O. Roos, U. Ryde, V. Veryazov, P.-O. Widmark, M. Cossi, B. Schimmelpfennig, P. Neogrady, and L. Seijo, MOLCAS: a program package for computational chemistry, *Computational Materials Science*, 28(2):222 – 239, 2003, Proceedings of the Symposium on Software Development for Process and Materials Design.
- [94] V. Veryazov, P.-O. Widmark, L. Serrano-Andrés, R. Lindh, and B. O. Roos, 2MOLCAS as a development platform for quantum chemistry software, *International Journal of Quantum Chemistry*, 100(4):626–635, 2004.
- [95] F. Aquilante, L. De Vico, N. Ferré, G. Ghigo, P.-A. Malmqvist, P. Neogrady, T. B. Pedersen, M. Pitoňák, M. Reiher, B. O. Roos, L. Serrano-Andrés, M. Urban, V. Veryazov, and R. Lindh, MOLCAS 7: The Next Generation, *Journal of Computational Chemistry*, 31(1):224–247, 2010.
- [96] K. Andersson, P.-k. Malmqvist, and B. O. Roos, Second order perturbation theory with a complete active space self consistent field reference function, *The Journal of Chemical Physics*, 96(2):1218–1226, 1992.
- [97] B. R. L. Galvao, P. J. S. B. Caridade, and A. J. C. Varandas, N(⁴S/²D)+N₂: Accurate ab initio-based DMBE potential energy surfaces and surface-hopping dynamics, *The Journal of Chemical Physics*, 137(22), 2012.
- [98] M. P. Deskevich, D. J. Nesbitt, and H.-J. Werner, Dynamically weighted multi-configuration self-consistent field: Multistate calculations for F+ H₂O → HF+ OH reaction paths, *The Journal of chemical physics*, 120(16):7281–7289, 2004.
- [99] B. J. Braams and J. M. Bowman, Permutationally invariant potential energy surfaces in high dimensionality, *International Reviews in Physical Chemistry*, 28(4):577–606, 2009.
- [100] R. Hernández-Lamonedá and A. Ramírez-Solís, Spin-orbit coupling in highly vibrationally excited O₂ (v) and O₂ (v= 0)-O₂ (v), *Chemical Physics Letters*, 321(3):191–196, 2000.

- [101] R. Hernández-Lamoneda and A. Ramírez-Solís, Systematic ab initio calculations on the energetics and stability of covalent O_4 , *The Journal of chemical physics*, 120(21):10084–10088, 2004.
- [102] M. Caffarel, R. Hernández-Lamoneda, A. Scemama, and A. Ramírez-Solís, Multireference quantum Monte Carlo study of the O_4 molecule, *Physical review letters*, 99(15):153001, 2007.
- [103] A. Ramírez-Solís, F. Jolibois, and L. Maron, Ab initio molecular dynamics studies on the ground singlet potential energy surface of the tetraoxygen molecule, O_4 , *Chemical Physics Letters*, 485(1):16–20, 2010.
- [104] E. T. Seidl and H. F. S. III, Is there a transition state for the unimolecular dissociation of cyclotetraoxygen (O_4)?, *The Journal of Chemical Physics*, 96(2):1176–1182, 1992.
- [105] T. K. Mankodi, U. V. Bhandarkar, and B. P. Puranik, An ab initio chemical reaction model for the direct simulation Monte Carlo study of non-equilibrium nitrogen flows, *The Journal of Chemical Physics*, 147(8):084305, 2017.
- [106] R. R. Laher and F. R. Gilmore, Improved fits for the vibrational and rotational constants of many states of nitrogen and oxygen, *Journal of physical and chemical reference data*, 20(4):685–712, 1991.
- [107] O. P. Shatalov, Molecular dissociation of oxygen in the absence of vibrational equilibrium, *Combustion, Explosion and Shock Waves*, 9(5):610–613, 1973.
- [108] L. B. Ibragimova, G. D. Smekhov, and O. P. Shatalov, Dissociation rate constants of diatomic molecules under thermal equilibrium conditions, *Fluid Dynamics*, 34(1):153–157, Jan 1999.
- [109] D. A. Andrienko and I. D. Boyd, State-specific dissociation in O_2 - O_2 collisions by quasiclassical trajectory method, *Chemical Physics*, 491:74–81, 2017.
- [110] R. K. Hanson and D. Baganoff, Shock-Tube Study of Nitrogen Dissociation Rates Using Pressure Measurements, *AIAA Journal*, 10:211–215, February 1972.
- [111] S. R. Byron, Measurement of the Rate of Dissociation of Oxygen, *The Journal of Chemical Physics*, 30(6):1380–1392, 1959.
- [112] B. Cary, Shock Tube Study of the Thermal Dissociation of Nitrogen, *Physics of Fluids*, 8(1):26–35, 1965.

- [113] N. Parsons, D. A. Levin, A. C. T. van Duin, and T. Zhu, Modeling of molecular nitrogen collisions and dissociation processes for direct simulation Monte Carlo, *The Journal of Chemical Physics*, 141(23), 2014.
- [114] R. Sayós, J. Hijazo, M. Gilibert, and M. González, Variational transition state calculation of the rate constants for the $\text{N}(^4\text{S}_u) + \text{O}_2(\text{X } ^3\Sigma_{g-}) \rightarrow \text{NO}(\text{X}^2\Pi) + \text{O}(^3\text{P}_g)$ reaction and its reverse between 300 and 5000 K, *Chemical physics letters*, 284(1):101–108, 1998.
- [115] J. Duff and R. Sharma, Quasiclassical trajectory study of the $\text{N}(^4\text{S}) + \text{NO}(\text{X}^2\Pi) \rightarrow \text{N}_2(\text{X}^1\Sigma_{g+}) + \text{O}(^3\text{P})$ reaction rate coefficient, *Geophysical research letters*, 23(20):2777–2780, 1996.
- [116] D. Bose and G. V. Candler, Thermal rate constants of the $\text{O}_2 + \text{N} \rightarrow \text{NO} + \text{O}$ reaction based on the 2A' and 4A' potential-energy surfaces, *The Journal of Chemical Physics*, 107(16):6136–6145, 1997.
- [117] D. Baulch, *Evaluated kinetic data for high temperature reactions*, Homogeneous Gas Phase Reactions of the $\text{H}_2\text{-N}_2\text{-O}_2$ System. Butterworths, 1973.
- [118] W. Lin, R. Meana-Pañeda, Z. Varga, and D. G. Truhlar, A quasiclassical trajectory study of the $\text{N}_2(\text{X}^1\Sigma) + \text{O}(^3\text{P}) \rightarrow \text{NO}(\text{X}^2\Pi) + \text{N}(^4\text{S})$ reaction, *The Journal of chemical physics*, 144(23):234314, 2016.
- [119] H. Luo, M. Kulakhmetov, and A. Alexeenko, Ab initio state-specific $\text{N}_2 + \text{O}$ dissociation and exchange modeling for molecular simulations, *The Journal of Chemical Physics*, 146(7):074303, 2017.
- [120] J. P. Appleton, M. Steinberg, and D. Liquornik, Shock-Tube Study of Nitrogen Dissociation using Vacuum-Ultraviolet Light Absorption, *The Journal of Chemical Physics*, 48:599–608, 1968.
- [121] D. Bose and G. V. Candler, Thermal rate constants of the $\text{N}_2 + \text{O} \rightarrow \text{NO} + \text{N}$ reaction using ab initio 3A'' and 3A' potential energy surfaces, *The Journal of Chemical Physics*, 104(8):2825–2833, 1996.
- [122] R. C. Millikan and D. R. White, Systematics of Vibrational Relaxation, *The Journal of Chemical Physics*, 39(12):3209–3213, 1963.
- [123] T. K. Mankodi, U. V. Bhandarkar, and B. P. Puranik, Dissociation Cross-sections for High Energy $\text{O}_2\text{-O}_2$ Collisions, *The Journal of Chemical Physics*, 148(14):144305, 2018.

List of Publications

- [1] Mankodi T.K., Bhandarkar U.V. , Puranik B.P., *Cross-sections for $O_2 + N$ system using the QCT method*, Chemical Physics Letters, Volume 706, pp 1, (2018)
 - [2] Mankodi T.K., Bhandarkar U.V. , Puranik B.P., *Collision Induced Dissociation Cross-section for High Energy N_2-O_2 Collisions*, Chemical Physics Letters, Volume 704, pp 21, (2018)
 - [3] Mankodi T.K., Bhandarkar U.V. , Puranik B.P., *Dissociation Cross-section for High Energy O_2-O_2 collisions*, The Journal of Chemical Physics, Volume 148, Issue 14, pp 144305, (2018)
 - [4] Mankodi T.K., Bhandarkar U.V. , Puranik B.P., *Global potential energy surface of ground state singlet spin O_4* , The Journal of Chemical Physics, Volume 148, Issue 8, pp 074305, (2018)
 - [5] Mankodi T.K., Bhandarkar U.V. , Puranik B.P., *An ab initio chemical reaction model for the direct simulation Monte Carlo study of non-equilibrium nitrogen flows*, The Journal of Chemical Physics, Volume 147, Issue 8, pp 084305, (2017)
 - [6] Mankodi T.K., Bhandarkar U.V. , Puranik B.P., *Dissociation cross sections for $N_2 + N \rightarrow 3N$ and $O_2 + O \rightarrow 3O$ using the QCT method*, The Journal of Chemical Physics, Volume 146, Issue 20, pp 204307, (2017)
-

Conferences

- [1] Mankodi T.K., Bhandarkar U.V. , Puranik B.P., *Computational and Accuracy Analysis of a Reduced and Full Scale Ab-initio Based Chemical Model in DSMC*, 5th National Symposium on Shock Waves, Terminal Ballistics Research Laboratory, Chandigarh, India 2018.
- [2] Mankodi T.K., Bhandarkar U.V. , Puranik B.P., *Comparison of DSMC Chemistry Models for Rarefied Shock Tube Simulations with Nitrogen*, 31th International Symposium on Shock Wave, Nagoya, Japan 2017.
- [3] Mankodi T.K., Bhandarkar U.V. , Puranik B.P., *Comparison of Chemical Reaction Models with various Experimental Reentry Capsules using DSMC*, 30th International Symposium on Shock Wave, Tel Aviv, Israel 2015.
- [4] Mankodi T.K., Bhandarkar U.V. , Puranik B.P., *DSMC simulation of a Micro-turbine Blade Cascade Assembly*, 24th International Conference on Discrete Simulation of Fluid Dynamics, Edinburgh, 2015.
- [5] Mankodi T.K., Bhandarkar U.V. , Puranik B.P., *Density Distribution based Interpolated Grid for DSMC*, 29th International Symposium on Rarefied Gas Dynamics, Xi'an, China 2014.

Poster Presentation

- [1] Mankodi T.K., Bhandarkar U.V. , Puranik B.P., *Chemical Reaction Model for Direct Simulation Monte Carlo*, 4rd National Symposium on Shock Waves, Karunya Institute of Technology and Sciences,Coimbatore, India 2016.
- [2] Mankodi T.K., Bhandarkar U.V. , Puranik B.P., *Effect of LB Model Parameters on the Convective Heat Flux in DSMC*, 1st International ISHMT-ASTFE Heat and Mass Transfer Conference, Thiruvananthpuram, India 2015.
- [3] Mankodi T.K., Bhandarkar U.V. , Puranik B.P., *DSMC Simulations to Study Heat Flux Over SA Model Re-entry Vehicle*, 3rd National Symposium on Shock Waves, IIT Bombay, Mumbai,India 2014.

Acknowledgement

I express my sincerest gratitude to my guide, Prof. Upendra V. Bhandarkar. His wisdom has made me a fine researcher and more importantly a better human being. I look up to him as my role model. I thank Prof. Bhalchandra P. Puranik for his constant support and counsel during my tenure as a PhD student at IITB. I am truly lucky to have mentors like them.

I would like to thank my Research Progress Committee members: Prof. Shivasubramanian Gopalakrishnan, Prof. Prabhu Ramachandran and Prof. Kowsik Bodi for their valuable advice. Their questions and suggestions during the Annual Progress Seminars have helped me in understanding the subject in a better way. I take this opportunity to thank my professors at IITB whose teaching has motivated me to take up academics as a career choice. I would also like to acknowledge Prof. Jyotimay Banerjee and Prof. Hemant Naik from Department of Mechanical Engineering, Sardar Vallabhbhai National Institute of Technology (SVNIT), Surat for inspiring me to pursue research after my graduation. I also thank the anonymous reviewers of my journal papers for their honest opinions and criticisms. I owe my school teachers at Anandalaya, Anand for imbibing values that will lifelong benefit me. I am especially grateful to my mathematics teacher, Sreehari Kulur Sir, who encouraged creativity and instilled passion for learning.

I had a great time with my lab mates: Ashish Sharma, Aniket Sachdeva, Vipin Bokade and Jim George. I thank them for keeping the overall atmosphere of the lab positive. I specially thank my PhD mates, Abhimanyu Gavasane, Dr. Niraj Shah and Avick Sinha, for being there whenever I needed them.

Finally, I am who I am because of my parents. Their love and affection cannot be expressed in any form that I know of. Mummy and pappa are, and will always be, the reason and purpose of my life. I am indebted to my family who supported me in my time of need.

Tapan K. Mankodi